5-1-2018

Defect Growth Characterization in Modern Rail Steel

Sena Kizildemir
Lehigh University, sek615@lehigh.edu

Defect Growth Characterization in Modern Rail Steel

by

SENA KIZILDEMIR

A Thesis

Presented to the Graduate and Research Committee

of Lehigh University

in Candidacy for the Degree of

Master of Science

in

Structural Engineering

Lehigh University

May, 2018

This thesis is accepted and approved in partial fulfillment of the requirements for the Master of Science.

_____

Date

_____

Herman F. Nied

Thesis Advisor

_____

Paolo Bocchini

Co-Advisor

_____

Panayiotis Diplas

Chairperson of Department

ACKNOWLEDGEMENTS

I would like to thank my thesis advisors, Dr. Herman Nied and Dr. John Dupont for their guidance, advice, motivation and patience. I believe, beyond doubt, that this thesis wouldn't have been completed without their support and direction. Their efforts were invaluable towards my academic progress and becoming a skillful engineer.

I would like to thank to all my professors at Lehigh, especially to my academic advisor Dr. Paolo Bocchini for his support and assistance with many technical and nontechnical challenges throughout my studies.

Sincere gratitude is due towards the staff of Whitaker, Packard and Atlss Center as well.

I would like to specially thank to the Federal Railroad Administration and specifically Dr. Robert Wilson for funding this project as well as for his management and technical contributions. I would also like to acknowledge invaluable technical contributions by Dr. David Jeong, as well as those of Michael Carolan and Dr. Benjamin Perlman, of Volpe National Transportation Systems Center (Volpe), and lastly Dr. Fred fletcher of Arcelor Mittal, who donated the rails and offered great insights into all aspects of the project.

Another special thanks to my undergraduate professor and a Lehigh alumni, Dr. Basar Civelek for guiding and inspiring me to come to Lehigh University.

I would like to thank all my friends, especially my office mates Jeongjoo Kim and Omar Alawad, for their company and support which made me feel at home, here in Bethlehem.

Last but not the least, I would like to thank my family for their love, non-stop encouragement and believing in me despite the miles between us. I am especially grateful to my mother, Birsen Kizildemir, for her endless compassion and encouragement in every decision I made in my life. She has been always there for me.

TABLE OF CONTENTS

ILLUSTRATIONS

TABLES

1 ABSTRACT

This thesis investigates the fatigue characterization of modern head-hardened rails, with a specific focus on detail (i.e. transverse) fracture. This study provides necessary information to determine a safe and economically viable rail inspection interval.

Safe inspection interval has previously been established for legacy, i.e. non-head-hardened rails. The head hardening process, which evolved over the past several decades, has been designed to improve rail wear resistance by increasing hardness. Unfortunately, increasing hardness, which is related to strength, typically results in reduction of toughness and fatigue life. This means that while improved wear resistance can extend the wear life of the rail, its fatigue life can simultaneously be reduced. Consequently, the safe inspection interval for legacy rails is not necessarily valid for modern rails. Thorough material characterization of modern rails in reference to legacy rails is necessary to establish the applicability of the legacy rail inspection interval to head hardened rails.

Three modern rails (i.e. ArcelorMittal's AHH, HH, and SS – standard, control-cooled rail) and two unused legacy rails produced in 1977 and 1984, were investigated here. The SS rail, the legacy rails and existing data were used as a reference. As expected, the two modern head hardened rails (i.e. AHH and HH) are significantly harder and stronger than the control rail (i.e. SS) and the two legacy rails. Uniform pearlitic microstructure was observed in all rails, with hardness and strength variation caused primarily by pearlite spacing, which is controlled by the cooling rate and the alloy content. Despite the strength variation, toughness test results are fairly uniform across all rails, with some spatial variation inside the rail heads. Similarly, no significant differences in fatigue crack growth rates between modern and legacy rails have been observed (especially between AHH and legacy rails). These results indicate that the head hardening process designed to improve wear resistance, does not have a significant negative impact on fatigue life of rails. It is important to note that improving wear resistance of modern rails, without sacrificing fatigue properties in reference to legacy rails is a significant enhancement in rail manufacturing technology. However, it can result in fatigue becoming the limiting factor for the overall life of the rail, which places higher emphasis on rail inspection and characterization of fatigue and fracture properties.

Residual stresses due to heat treatment and roller straightening were also investigated in the AHH and HH rails by means of neutron diffraction measurements supplemented by advanced numerical analysis. The results show that the largest stress component (~350MPa) is the longitudinal stress, which is also the most consequential for fatigue growth of transverse defects. Given long beam time required to penetrate the rail material, full 3D distribution of residual stresses is difficult to obtain. Additionally, interpretation of the residual stress state measured with smaller specimens, such as plane stress slices and half-rail samples cut along the longitudinal, vertical symmetry plane, is very challenging due to significant level of interaction between different stress components. This means that extracting a rail specimen by cutting, not only relives the stress component normal to the cut plane, but it also affects the remaining stress components. Considering the importance of the longitudinal residual stresses for transverse crack growth rates, their magnitude and distribution, as well as the effect of rail-wheel contact, require further investigation.

2 INTRODUCTION

2.1 Background

The steel rail has been the most used and irreplaceable component of the world's railroad transportation systems. It basically transmits the forces coming from the wheel to the track bed as its primary function.

The steel rail became practically used and available in 19th century. The Pennsylvania steel company in Steelton, PA was the first in the United States to commercially produce steel in 1867 using the Bessemer process. Before that date, they were procured from England however it was really expensive to do so. In the early days, steel was far high quality material compared to the available cast iron and wrought iron rails which were too brittle and too soft respectively. Especially in 18th century the rails were made of cast iron and unable to redistribute loads through permanent plastic deformations. Some time later it was understood that the most of the rail failures were because of that common material. An important discovery that made steel cost-effective was an invention known as Bessemer converter. Henry Bessemer, and English businessman, discovered a way to produce a "purer" form of molten iron.

The key principle of the Bessemer process was to remove all the impurities from the iron by blowing air through molten iron in an open top vessel. This was also called oxidation and raised the temperature of the iron and kept it molten. A photo of Bessemer converter of that at the Pennsylvania steel company is shown below.

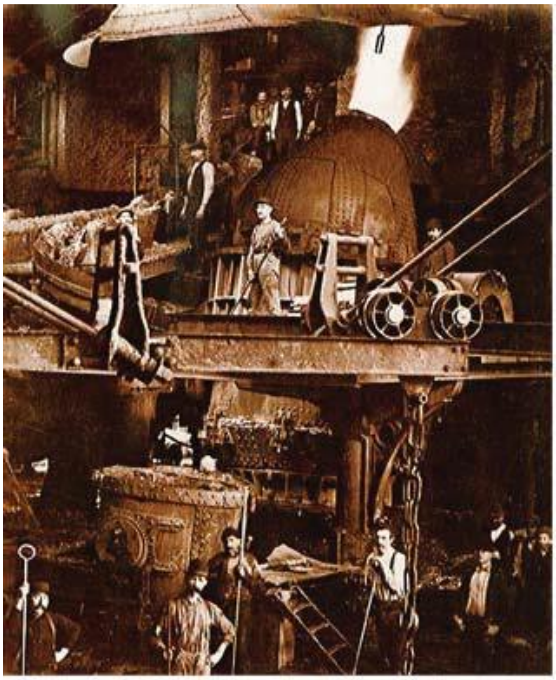

Figure 1 - Bessemer converter, 1880.

After the first full application of this Bessemer method in the U.S to produce rails, in around 1880, the expensive steel rails from England were no longer competitive and from this point on the America's railroad industry dramatically expanded.

Bessemer process was the first but not the only development for the production of steel. After that the open heart furnace and electrical arc furnace processes are developed.

The characteristics of rail steel in the Bessemer era with today's rail steel have some major differences. The most important one is the chemical elements level. Especially the carbon levels were so much lower in the early times than they are today. The table below [5] shows a chemical analysis of both rails.

Date (type of steelmaking)	**C**	**Mn**	**P**	**S**	**Si**
1890(Bessemer Converter)	0.58	1.33	0.074	0.072	0.08
2013 (Electric Furnace)	0.84	1	0.01	0.008	0.4

Table 1 – Typical Chemical analysis in early and modern steel rail

The second noticeable difference is the high levels of phosphorus and sulfur. It was learned that these two elements were not desired in rail because they impart poor ductility. These impurity elements were not effectively removed from the molten pig iron by the Bessemer converter. Later, the open hearth furnace was able to lower both sulfur and phosphorus through a longer refining time and a lime-based slag practice [5] .

Another difference is the lower silicon level. Today, silicon is an essential element for deoxidation of the molten steel. Silicon is also added to increase hardness. The manganese level in the Bessemer steel was higher compared with modern day rail steel. However, most of today's rail steels still have basic carbon/manganese compositions with pearlitic microstructures possibly with some limited grain boundary ferrite [55]. As the Bessemer process was phased out, refining the steel was the advantage of the open hearth furnace [5] .The more information on rail steel history, properties and manufacture up to 1913 can be found in reference [53].

As the usage and production of rail steel increased in the latter part of the 19th century, the railroad specifications became needed and were began to be developed for steel rail. The American Railway Engineering and Maintenance of Way Association (AREMA) recommended specifications for rail in 1907 and Committee 1 of the American Society for Testing and Materials (ASTM) adopted specifications for rail the same year [54, 57]. The very first specification for a steel rail is adopted by ASTM (ASTM A1) that indicates the importance of rail manufacture and use in that era.

The AREMA specification (1907) was mostly composed of a table of chemical composition intervals and limits for Bessemer steel rails. However, obviously, as the railroads expanded dramatically, the specifications were also improved and became very sophisticated comparing to the past 100 years. A comparison of chemical composition ranges in the 1907 and current AREMA specifications are shown in table below.

1907	**C**	**Mn**	**P**	**S**	**Si**
70-79 (lb/yd)	0.5-0.6	0.75-1.00	0.085 max	0.075 max	0.020 max
80-89	0.53-0.63	0.80-1.05	0.085 max	0.075 max	0.020 max
90-100	0.55-0.65	0.80-1.05	0.085 max	0.075 max	0.020 max
2013	0.74-0.86	0.75-1.25	0.020 max	0.020 max	0.10-0.60

Table 2 – Chemical composition ranges for early and modern specifications

On the other hand, the only mechanical property specification was about drop weight tests. It should be worth to mention here that the Brinell and Rockwell hardness test were not established in that time. When we look at the chemical analysis over the years, we see that the main element greatly increased was carbon. As it is known that the increasing carbon content makes the rail steel harder which improves the wear resistance. With the invention of head hardening processes, the rail's hardness and strength were increased a lot comparing to the standard strength ambient air cooled rails while maintaining the adequate rail's ductility. These processes employ accelerated cooling to increase the cooling rate prior to and during the austenite to pearlite transformation [59].The objective is to produce pearlite with the finest possible spacing between ferrite and cementite lamella. The pearlite microstructure in head hardened rail heads is shown below.

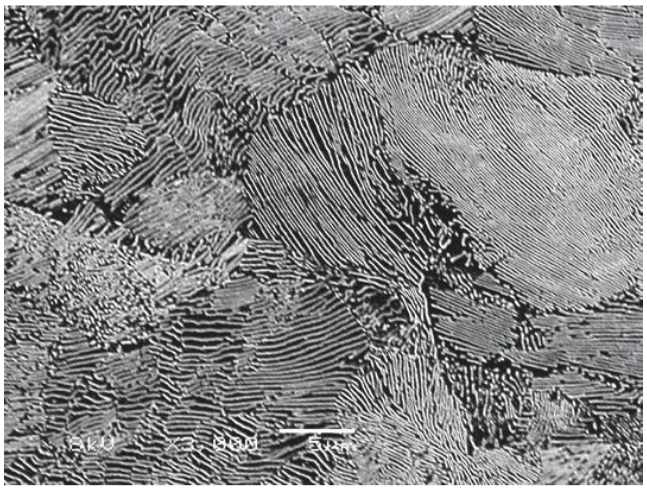

Figure 2 – Pearlite colonies in head hardened rail

It’s also needed to be noted that in the head hardened rail, the inter spacing cannot be resolved using the conventional light microscope and a scanning electron microscope is required to achieve higher magnification [59].

The head hardening processes that briefly mentioned above, involves a 100 meter long system that sprays either water, mist or oil on to rails to cool them as they passes through the cooling zones[58]. The process introduces a microstructural gradient inside the head (Figure 4c), which can lead to variable crack growth rate inside the head. These processes has been developed and used since 1994 to produce intermediate strength head hardened (ISHH), head hardened (HH), and advanced head hardened (AHH) rails.

The head hardening process described previously [58] is done at the facility at Steelton, which is in-line with the rail mill. To describe it better, we can say that the rolled hot rails directly proceed to the facility. The picture of it can be found below.

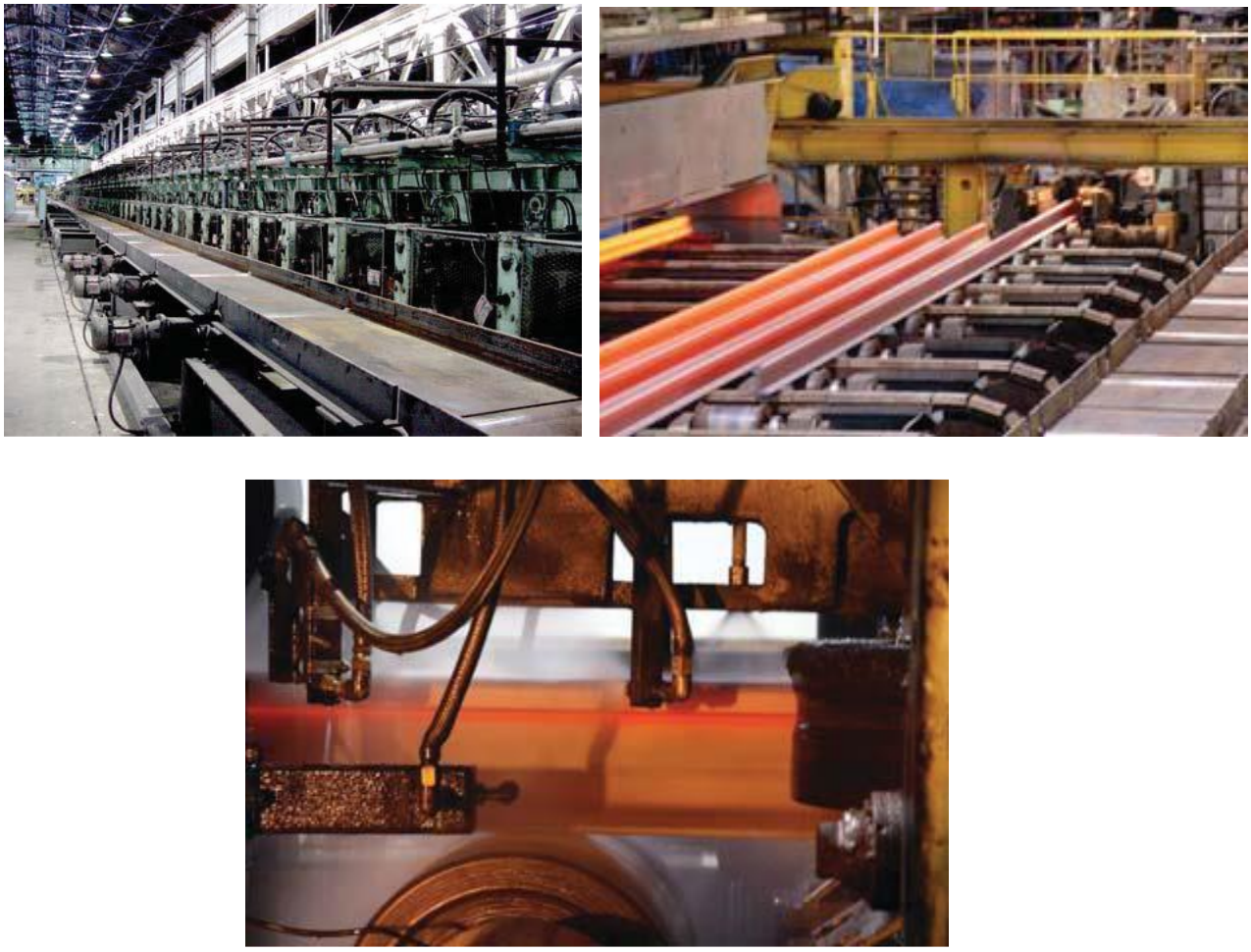

Figure 3 – Head hardening facility at ArcelorMittal, Steelton.

It is known that the rails which have a higher hardness and strength show more resistant to the surface damages. However, all pearlitic rails eventually experience surface damage due to the heavy axle loads. This surface damage forms where the pearlitic microstructure deforms and aligns with the running surface. Over time, those micro levels deforms piles up and creates the surface crackings. This incident, in general, is called contact fatigue. The crack propagation is globally dealt with by the application of fracture mechanics. There are some failure models developed to incorporate fatigue crack propagation. A model that considers the mechanism by which a horizontal shell turns down into a transverse detail fracture has been developed by Farris et al. [56]

The propagation of the internal transverse rail defects, also known as detail fracture, is one of the most important threats to safe operation of rail transport (Figure 4b). The shallow surface cracking generates deeper ones and develops into transverse defects that form and grow in the rail steel as a result of cyclic forces caused by the repeated passage of trains. Detail fracture typically originates from the longitudinal fracture crack known as the shell (Figure 4a). Detail fracture can grow to critical size without any visible material damage on the rail surface [43].

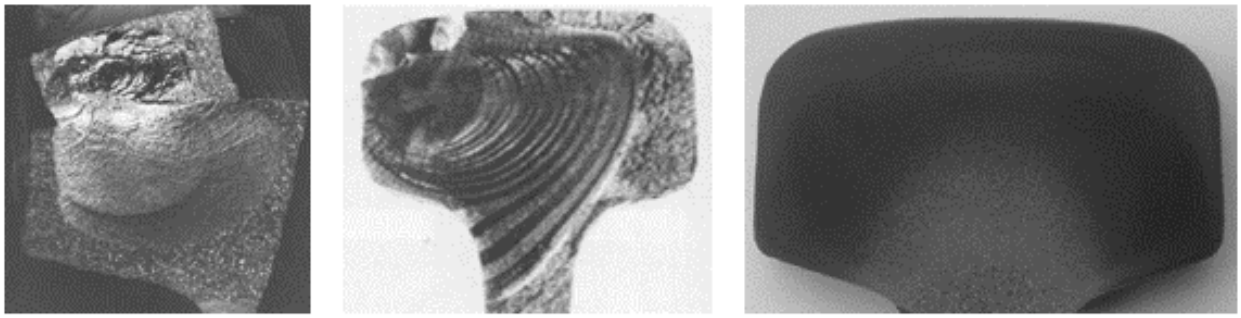

(a) (b) (c)

Figure 4 – (a) Longitudinal shell fracture and transition into the detail fracture; (b) Detail fracture [38]; (c) Microstructural gradient produced by the heat treatment in modern rails [52].

As it was mentioned above previously, the main objective of head hardening is to improve wear resistance of rails achieved by increasing hardness of the head. Other than hardness, there are no requirements for wear resistance. However, in most steels, strength increase is usually associated with ductility reduction, which negatively affects fracture toughness [2]. Today's typical rail steel is strong and resistant to wear but its ductility is limited and at most operating temperatures it will fracture, in the presence of a sharp tipped discontinuity, such as a fatigue crack, in a brittle cleavage mode. This topic has been extensively investigated during the past several decades by the National Transportation Systems Center (Volpe) in conjunction with the rail industry, which resulted in a comprehensive life evaluation methodology for legacy rails (i.e. non head-hardened rails) [17, 20, 23, 29, 34, 36] and establishing the maximum inspection interval of 40 MGT [34]. The railhead hardening process, which has been evolving over the past ~30 years, is a major improvement in the rail manufacturing technology.

Another important effect that needs to be considered is the influence of residual stresses introduced by the heat treatment process. Residual stresses provide a significant contribution to the overall stress state in the railhead. In addition, their distribution follows, to some degree, the microstructural gradient, i.e. residual compression on the top of the railhead changes to tension inside the head, where the material is softer. Interaction if these two effects, i.e. property variation and residual stress distribution in the railhead can have a significant effect on fatigue life of the rail. Thus, the inspection intervals previously determined for legacy rails, might not be applicable to modern head hardened rails.

Establishing the new inspection interval for modern rails would require a multiyear effort, similar to the one conducted previously for legacy, i.e. non-head hardened rails, which spanned several decades. This is beyond the scope of the project discussed in this thesis. The focus of the effort discussed here is on detailed experimental investigation of the effects of head hardening on fatigue and fracture properties in modern rails, in reference to legacy rails.

2.2 Objectives

The main objective of the research effort described in this thesis is to investigate the effects of head hardening on fatigue behavior of modern rails. The data and observations made during the project and presented in this thesis provide necessary information to determine safe and economically viable inspection interval for modern rails.

A secondary objective of the project is development of a systematic and repeatable test plan to characterize the microstructural gradient and residual stresses in rails, as well as a clear and consistent procedure to collect and interpret the data. This plan is necessary considering significant variability in the rail properties resulting from different railhead hardening process used over the past ~30 years (e.g. induction cooling; compressed air, water or mist cooling; oil quenching [5, 52]).

2.3 Overall Approach

Reaching the project objectives requires detailed experimental characterization of modern rail steel. Multiple experimental techniques and methods are employed to investigate specific aspects of fatigue behavior in rails, including:

- *HARDNESS:*
  Rockwell hardness mapping is used to identify strategic locations for collection of material samples for light optical microscopy (LOM) and scanning electron microscopy (SEM). Hardness maps provide a general overview of spatial property distribution in the railhead, which is a function of microstructural gradient.
- *METALOGRAPHY:*
  LOM and SEM microstructural observations using Hitachi 4300 High Resolution Field Emission SEM equipped with a state-of-the-art integrated EDAX-TSL energy dispersive X-ray system. These observations allow a detailed mapping of the microstructure in the railheads.
- *TENSILE TESTING:*
  Tensile testing of the rail steel using samples extracted from different location inside the rail. Tensile tests provide a simple and effective way of investigating the elastic properties

and the yield strength of the investigated rails as well as their ductility under uniaxial loading conditions.

- *TOUGHNESS AND FATIGUE TESTING:*
  Fracture toughness and fatigue crack growth measurements using machined compact tension (CT) and center cracked tension (CCT) specimens cut from various locations and orientations within the rails. These measurements are an essential component of investigating fatigue properties of rail steels. All previously conducted tests (hardness, metallography, tensile tests) provide necessary information for strategic planning of fracture and fatigue tests.
- *RESIDUAL STRESS MEASUREMENTS:*
  Neutron diffraction measurements performed to characterize the residual stress field in the rail. Detailed finite element simulations are used to optimize the specimens and analyze the data. These measurements allow approximation of the residual stress field in the railheads, which is a significant component of the overall stress state in the rails.

These and other measurement methods are used to characterize a representation of three modern rails, i.e. advanced head hardened (AHH), head hardened (HH) and standard control-cooled rail (SS), all of which were donated by ArcelorMittal. The SS rail serves as a baseline providing the reference data for comparison with the head-hardened rail data. In addition, two unused legacy rails are characterized, i.e. CF&I control-cooled rail manufactured in 1977 (CF&I77), and vacuum heat-treated Hayange Steel rail produced in 1984 (HAY84). Both legacy rails were donated by TTCI. While this representation of different rails and their properties can be considered comprehensive, it does not cover all possible rail types. Thus, the data generated here for both modern and legacy rails, is used for direct comparison with the corresponding data generated during the legacy Rail Integrity Research Program [17, 23, 34, 36]. This allows quantification of the microstructural gradient and residual stress effects on fatigue crack growth rate in modern rails in reference to legacy rails, expressed by the parameters of the crack growth relationship. Since a Paris-Walker relationship was used during the legacy Rail Integrity Program and its parameters for legacy rails were determined [21], the same relationship is used here for modern rails.

All critical observations and conclusions reached during execution of the experimental program are collected and documented. This serves the second objective of the project, i.e. development of a testing protocol for characterizing fatigue properties of modern rails.

2.4 Scope

Experimental material characterization effort is the primary component of the scope of work discussed in this thesis. The test plan is designed to meet the project objectives, i.e. investigation of the microstructural gradient and residual stress effects on fatigue and fracture properties of modern, head-hardened rail steel, in reference to legacy rail steel.

Five distinct rail types are used in the experimental program and are given the following designations throughout this report:

1. AHH – advanced head-hardened; new rail manufactured by ArcelorMittal
2. HH – head-hardened; new rail manufactured by ArcelorMittal
3. SS – standard, control-cooled rail; new non-head-hardened rail manufactured by ArcelorMittal

4. CF&I77 – Colorado Fuel & Iron control-cooled rail manufactured in 1977; never used
5. HAY84 – Hayange Steel vacuum heat treated rail manufactured in 1984; never used

The project includes the following tasks:

Task 1 – Microstructural Gradient

The objective of this task is to characterize the microstructural gradient in modern rails in reference to legacy rails through a combination of mechanical tests and metallurgical observations performed using light optical microscopy and scanning electron microscopy.

Task 2 – Residual Stress

The objective of this task is to characterize the residual stress state in the rails through a combination of neutron diffraction measurements and detailed finite element analyses.

Task 3 – Bending stress gradient

The objective of this task is to characterize the effect of different stress state in the rails caused by a combination of bending and residual stresses through toughness and fatigue crack growth rate measurements.

Task 4 – Data analysis and a test plan

This task is intended to collect and summarize the key observations made during the experimental testing program to establish best testing practices and a systematic test program that could be generally followed to characterize rail steel.

A detailed breakdown of project tasks, subtasks, milestones and deliverables is given in Table .

Table 3 – Project task breakdown and an experimental test plan

Tasks, Subtasks / Tests	Type of Test	Test Plan (Modern and Legacy Rails)
1.MICROSTRUCTURAL GRADIENT		
Chemical analysis of legacy rail steel	Chemical analysis	2 AM steels and ’77 & ‘80s rails[1]
Tensile test data	Uniaxial tension	5 samples; 3 AM steels[2] plus ’77 & ‘80s rails
Hardness data from AM - initial screening	Existing data	3 AM steels[2]
Rockwell Hardness mapping (all rails)		3 AM steels plus ‘77 & ‘80s rails
Light optical microscopy (LOM) – interpretation of the hardness map		3 AM steels plus ‘77& ‘80s rails
Hitachi 4300 High Resolution Field Emission SEM – samples removed based on LOM results		2 AM steels (AHH, HH) plus ’77 &’80s rails
Compact tension (CT) specimens – K_{Ic} plane strain toughness;	K_{Ic} ASTM E1820	5 CT locations[3]; 2 AM steels (AHH, HH) plus ’77 &’80s rails
Compact tension specimens – fatigue tests (da/dN tests); additional verification tests with center cracked tension specimen (CCT)	ASTM E647	5 CT locations, constant ΔK; 2 AM steels (AHH, HH) plus ’77 &’80s rails 2 CCT verification tests, 2AM steels
Rail samples – fatigue tests with constant ΔK tests → correlate with the CT results	constant ΔK	2 AM steels (AHH, HH) plus ’77 &’80s rails

2. RESIDUAL STRESSES		
Residual stress measurements – transverse and vertical stresses using thin slices	Neutron diffraction	3AM steels + ’77 & ’80s rails, 4 samples per rail
Residual stress measurements longitudinal direction (x “axial” stress component)	Neutron diffraction / contour	Single rail – AHH (highest strength)
3. STRESS GRADIENT		
Fatigue tests with under different stress states reflecting variable stress ratio	Variable stress ratio	3 CT – 2 steels (6 tests)

2.5 Organization of the Thesis

The next section of the thesis (Section 1) discusses the experimental test program including all pertinent tests performed in support of the thesis as well as a brief summary of the results. Measurement of the residual stresses in the rails, along with the supporting finite element simulations performed to optimize the test specimens and interpret the results are also included in Section 1. Section 4 presents the data analysis and the testing protocol to characterize the microstructural gradient and residual stresses in rails. Conclusions and discussion are given in Section 5 followed by references in Section 6. Appendices in the following order:

Appendix 1: Hardness data

Appendix 2: Tensile data

Appendix 3: Fracture toughness data

Appendix 4: Fatigue crack growth rate data

Appendix 5: Residual stress data

3 MECHANICAL TESTING OF RAILS

In order to characterize and quantify the mechanical behavior of head hardened rails of different types, grades and their properties, a methodical and repeatable testing plan was established. The primary purpose of the mechanical testing was to contrast the differences between different types of modern head hardened rails (AHH, HH) with standard modern rail (SS) and legacy rails that exhibit significantly lower head hardness (CF&I77, HAY84). The testing protocol required a sequence of chemical, mechanical, and metallurgical tests to be conducted. These tests may be listed under six main categories: (1) Characterization of alloy chemistry, (2) Characterization of metallurgical microstructure, (3) Characterization of uniaxial tensile properties, (4) Characterization of fracture toughness, (5) Characterization of fatigue crack growth behavior, and (6) Characterization of residual stress distribution. The mechanical testing and metallurgical observations were conducted primarily using facilities at Lehigh University. ArcelorMittal Global R & D performed the chemical analyses and the National Institute of Standards and Technology (NIST) performed the residual stress measurements at their neutron diffraction facilities in Gaithersburg, MD.

3.1 Test Articles

The main objective of this project is the characterization of the effects associated with rail head hardening, including the resulting residual stresses, on fatigue and fracture behavior of rails. This is achieved by establishing a reference set of properties obtained for non-head-hardened, i.e., SS and legacy rails, and comparing the properties of head-hardened rails to the reference rails. Most of the reference properties were established during the legacy rail integrity research program conducted during the 1980's and 90's [17, 20, 23, 29, 34, 36]. In addition, two legacy rails (CF&I77 and HAY84) and one new control-cooled rail (SS) are included in the current research program to provide further reference data for comparison with modern head hardened rail data. Thus, five distinct rails, given in Table 4, were used as test articles in this study.

Table 4 – Rails used as test articles with their designations

Rail Type	Designation	Manufacturer	Weight	Heat Treatment	Wear	Notes
Modern	**AHH** Advanced Head Hardened	ArcelorMittal	136 RE	Head hardened; fast cooled	New	Donated by AM
Modern	**HH** Head Hardened	ArcelorMittal	136 RE	Head hardened	New	Donated by AM
Modern	**SS** Standard rail	ArcelorMittal	136 RE	Control-cooled	New	Donated by AM
Legacy	**CF&I77**	Colorado Fuel & Iron, 1977	136 RE	Control-cooled	Never used	Donated by TTCI
Legacy	**HAY84**	Hayange Steel (currently Tata Steel)	136 RE	Vacuum heat treated and degassed	Never used	Donated by TTCI

Nominal dimensions for the 136RE – rail designation (136 lbs/yd) are shown in Figure 5. The AHH, HH, and SS rails were originally shipped in 30 ft. lengths to Lehigh University and then cut into smaller 3 ft. sections as shown in Figure 6 for subsequent sawing into plate stock and

machining into test specimens. The legacy rails (CF&I77 and HAY84), which were contributed to the project by TTCI are shown with their markings in Figure 7.

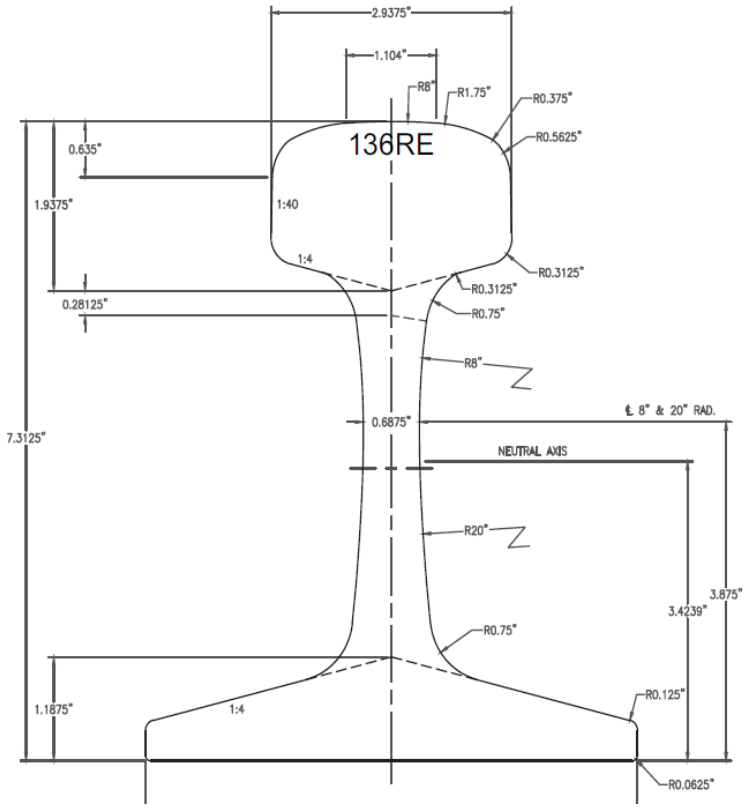

Figure 5 – Dimensions in inches for a 136RE rail cross-section.

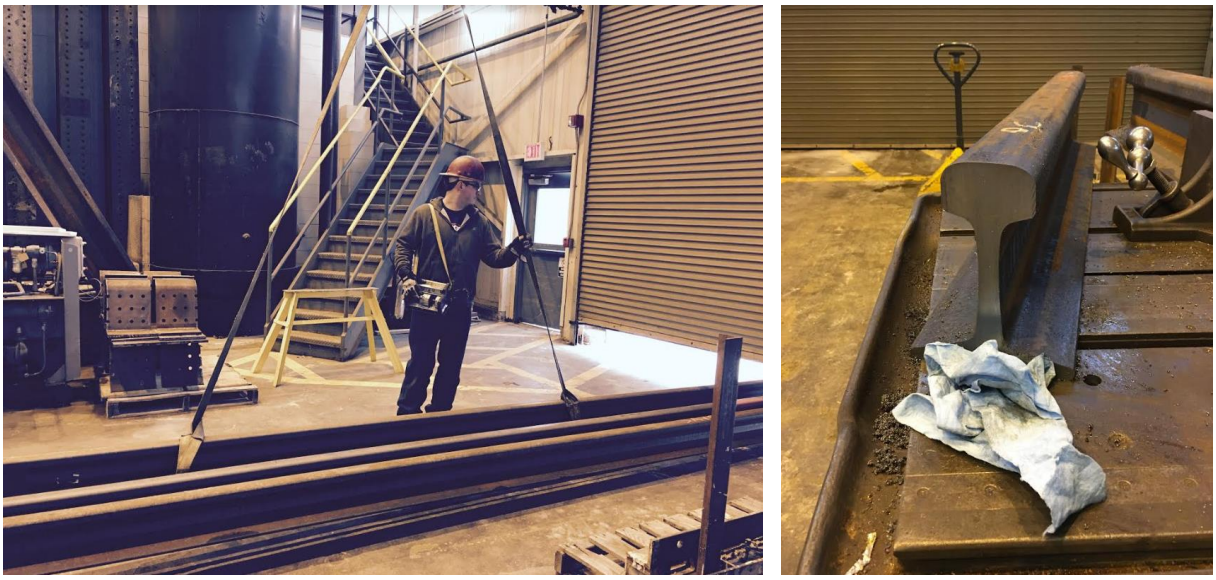

Figure 6 – Arrival of 30 ft. ArcelorMittal rails and sectioning at ATLSS Labs Lehigh University.

Figure 7 – Photographs of legacy rails, CF&I77 (top) and HAY84 (bottom), used to develop baseline data for comparisons with modern head hardened rails.

In the cutting and testing procedures, specimens were usually cut from horizontal slices in the rail head, or from vertical plates as shown in Figure 8. For example, Fig. 8a depicts the orientation of 0.025 in. thick horizontal plates cut for uniaxial tensile test specimens and Fig. 8b shows the plate thickness dimensions for two plates cut for fracture toughness (CT) specimens in the vertical direction. In both of these drawings the long dimension of the plates, usually 1 – 3 ft., coincides with the long axis of the rail.

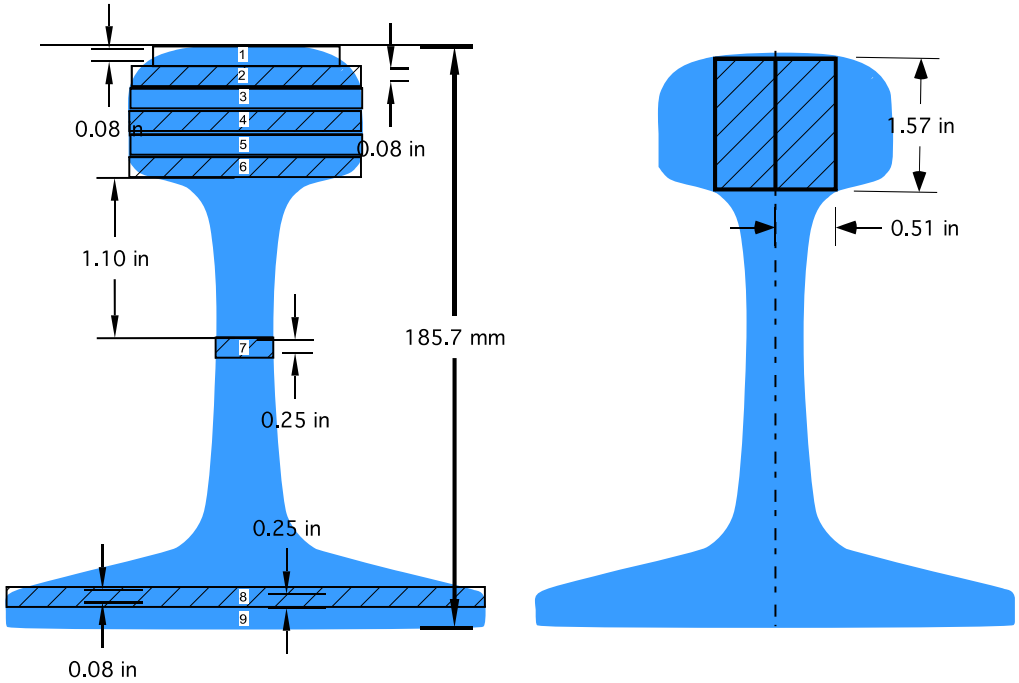

Figure 8 – (a) Locations of horizontal plates cut for uniaxial test specimens. (b) Location of vertical plate cuts for CT specimens with vertical crack orientations.

3.2 Chemical Composition

The chemical compositions of the modern rails employed in this study are shown in Table 3. The SS and HH rails comply with the requirements listed in AREMA for Carbon Rail Steel. Note that the HH rail is similar to the SS rail, with a small addition of titanium in the HH rail. The AHH rail has less manganese than the other two new rails, plus a small addition of vanadium. While AHH is not currently listed within the AREMA rail specification, AREMA permits the chemical composition limits of alloy high-strength rail steel grades to be subject to agreement between the purchaser and the manufacturer. Such agreements have enabled AHH rails to be placed in revenue service.

Table 5 – Chemical composition of ArcelorMittal rails designated AHH, HH, and SS

Type	C	Mn	P	S	Si	Cu	Ni	Cr	Mo	V	Nb	Ti	Al	B	N
AHH	0.84	0.69	0.012	0.012	0.54	0.26	0.09	0.24	0.023	0.086	0.002	0.022	0.004	0.0001	0.0087
HH	0.85	0.98	0.011	0.012	0.4	0.22	0.1	0.25	0.033	0.004	0.003	0.018	0.004	0.0003	0.0102
SS	0.83	1.11	0.011	0.012	0.54	0.25	0.11	0.21	0.023	0.004	0.003	0.003	0.004	0.0003	0.0087

Table 6 shows the compositions of the legacy rails. While the carbon content of the legacy rails is significantly less than the modern rails, the HAY84 rail meets the current AREMA chemical analysis for carbon rail steel. The CR&I77 rail contains only 0.72 %C which is less than the 0.74 %C minimum currently required by AREMA for carbon rail steel. The HAY84 rail contains much less copper than the other four rails and the CF&I77 rail has a significantly higher silicon content.

Table 6 – Chemical composition of legacy rails designated HAY and CF&I

Type	C	Mn	P	S	Si	Cu	Ni	Cr	Mo	V
HAY84	0.79	1.13	0.016	0.019	0.407	0.02	0.05	0.16	0.006	0.003
CF&I77	0.72	0.92	0.012	0.017	0.762	0.23	0.08	0.07	0.013	0.002

Chemical composition of legacy rails continued:

Type	Nb	Ti	Al	B	N	Sn	Sb	Co	Ca	Pb
HAY84	0.001	0.001	0.009	0.0002	0.0073	0.002	0.0009	0.015	0.0004	0.0029
CF&I77	0.002	0.003	0.009	0.0002	0.0073	0.013	0.003	0.0118	0.0007	0.0045

The five rails included in this study are all representative of many miles of rail in revenue service throughout the United States.

3.3 Hardness Testing

The purpose of the hardness testing was to determine the difference in hardness among the five rails examined in this study (AHH, HH, SS, HAY84, CF&I77). Since it was expected that the rails would not only exhibit different maximum hardnesses, but also very different spatial variations in hardness, a hardness map was generated for each rail head using 5 mm x 5 mm grid cells. The hardness measurements were performed using a standard Rockwell hardness tester on 8 mm thick plate cross sections from each of the rails. For the hardness tests, a C Brale penetrator was used with a 150 Kg load.

3.3.1 Sample Preparation

The preparation of test samples for hardness measurements involved saw-cutting 8 mm thick representative cross-sections from each of the 136RE rails. After cutting, the rail cross-sections were surface ground and marked with a 5 mm x 5 mm grid overlay using a low-power laser. Hardness measurements were made at the center point of each of the 5 mm x 5 mm cells over the entire head region of the rail, including along a vertical line at the center of the web, and along a line close to the bottom of the rail as shown in Figure 9.

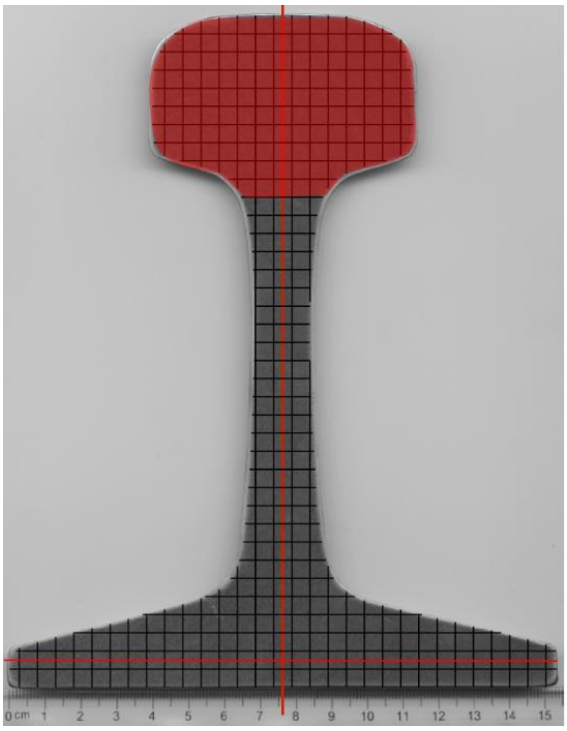

Figure 9 – Rail cross section showing grid used for hardness measurements in rail head and along vertical (web) and horizontal (base) lines.

3.3.2 Hardness Calibration

For hardness calibrations, 30.8 – 35.8 – 41.1 HRC and 61 HRA calibration blocks were used to calibrate the hardness tester. For each of the calibration blocks, an indirect verification was performed based upon ASTM E18 specifications. All E (error) values and all R (repeatability) values were within the maximum permitted ranges as shown in Tables 7 and 8 below. Therefore, the hardness calibrations satisfy the maximum error and repeatability requirements as specified in ASTM E18 and demonstrate that the reported hardness values are accurate.

Table 7 – Calibration block verifications 30.8 – 41.1 HRC

Calibration	HRC1	HRC2	HRC3	HRC4	HRC5	Avg	E	R	MAX E	MAX R
30.8	30.1	30.2	30.5	30.1	30.9	30.36	-0.1	0.8	2	1
35.8	35.5	36	36.1	36.1	36	35.94	-0.3	0.6	1.5	1
41.1	40.9	40.9	40.5	41	40.9	40.8	-0.26	0.5	1.5	1

Table 8 – Calibration block verification 61 HRA

Calibration	HR	HR	HR	HR	HR	Avg	E	R	MAX E	MAX R
61 HRA	61.5	61.0	60.9	61.8	61.8	61.4	0.8	0.9	2.0	1.0

3.3.3 Hardness Measurements

The hardness measurements were performed on the head portions of the rail cross-sections, as well as along a vertical line in the web and along a horizontal row on the lower portion of each rail as shown in Fig. 9. Detailed measurements superimposed on the rail cross section are reported in Appendix A, Figs. 114-118. Contour plots of the measured hardness values permit a better visualization of the variation in hardness on the face of the rail heads. Figure 10 contains contour plots of the HRC hardnesses shown with the same hardness scale. As can be seen in the images in Fig. 10, there are significant differences in the average and maximum head hardness values among the different rails. As expected, the progression in rail steel hardness coincides with chronological manufacturing history, i.e., the modern rails (AHH, HH and SS) exhibit the highest head hardness values. In addition, there are significant spatial variations in hardness within any given rail head. Because of the average hardness differences between the rails, the detailed spatial distribution of hardness within a given rail head is best visualized using different hardness scales for each rail head as shown in Figure 11. As expected, the rail head with the highest hardness in the crown is the AHH rail (Figs. 10a and 11a). The AHH rail had a minimum hardness of 36 HRC and a maximum of 43 HRC.

It is also useful to plot the hardness variation in the hardened heads along the central vertical line measured from the rail head running surface to the base of the head as shown in Figure 12 and horizontally across the midsection of the head as in Figure 13. As graphically shown in Fig. 12, modern head hardened rails (AHH and HH), exhibit considerably higher hardness in the crown of the rail, with hardness values that remains fairly constant within a zone extending at least 12 mm below the rail head running surface.

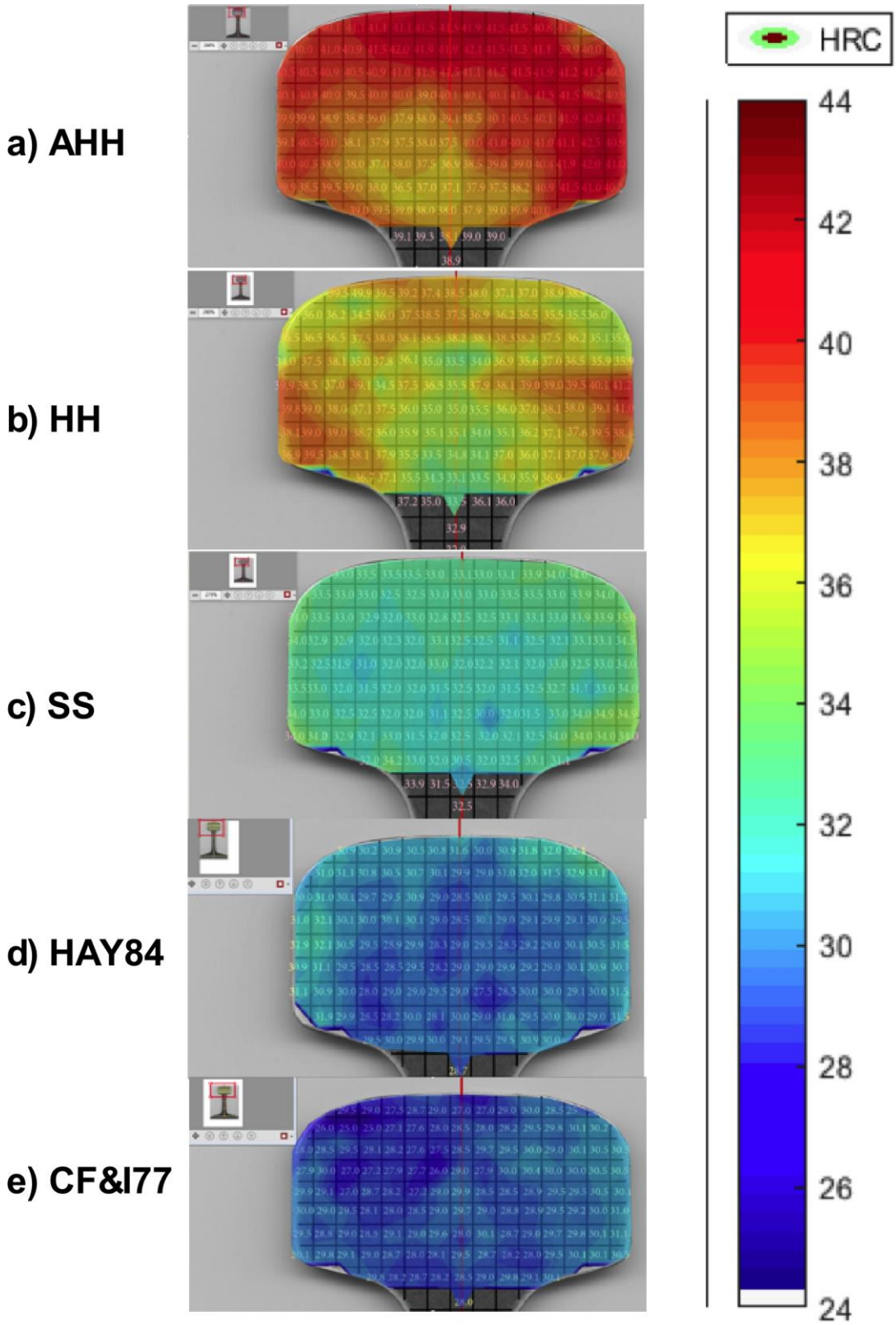

Figure 10 – Contour plots showing hardness variation in the rail heads using the same HRC scale.

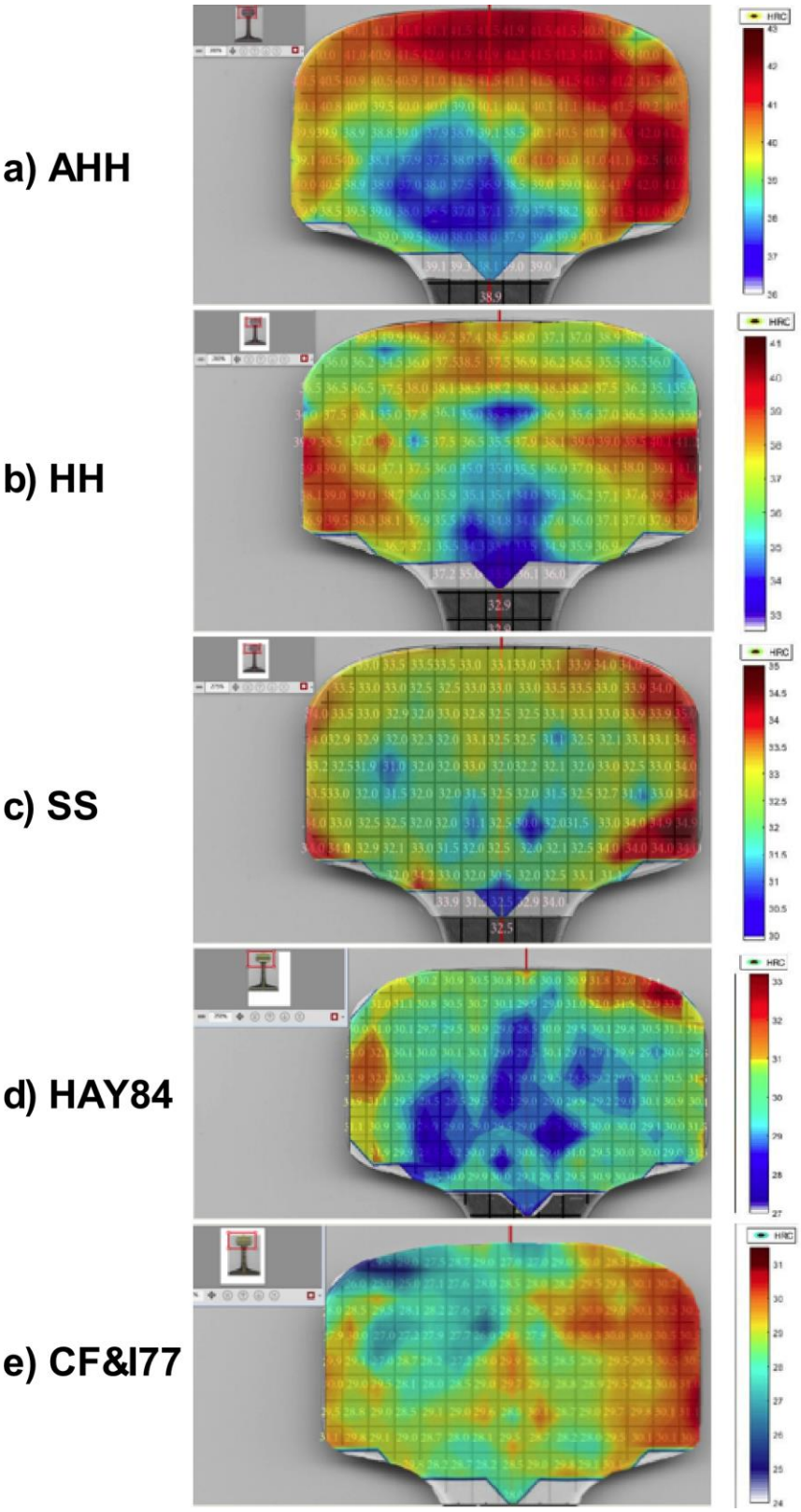

Figure 11 – Contour plots showing head hardness variations with different HRC scales. AHH (36 – 43), HH (33 – 41), SS (30 – 35), HAY84 (27 – 33), CF&I77 (24 – 31).

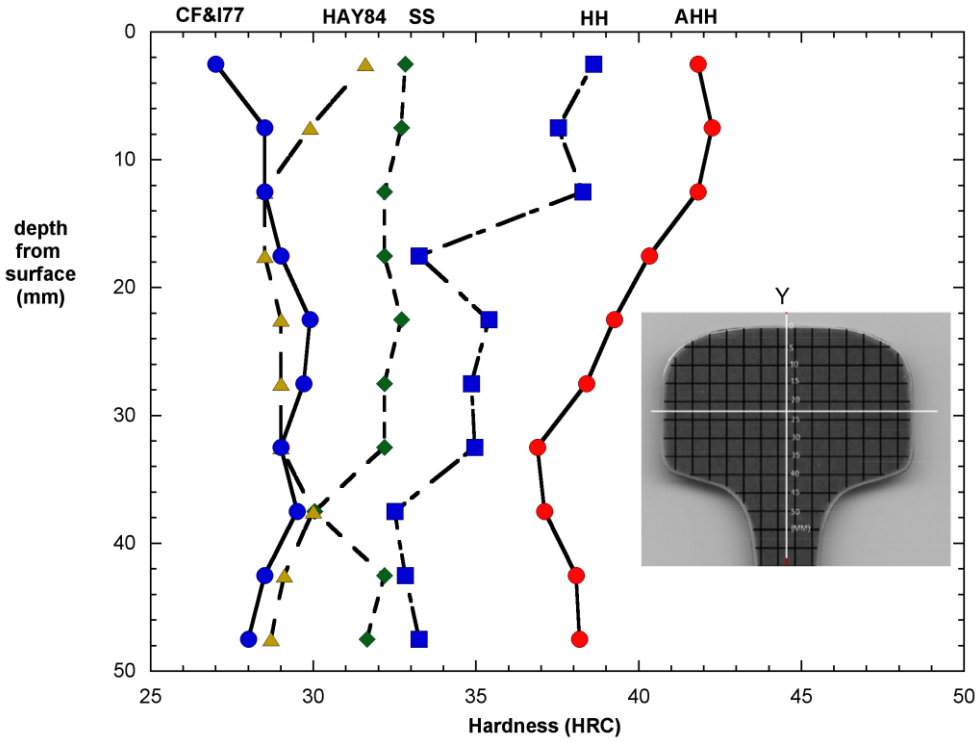

Figure 12 – HRC hardness as a function of vertical depth on the rail head's plane of symmetry (0 marks the running surface of the rail).

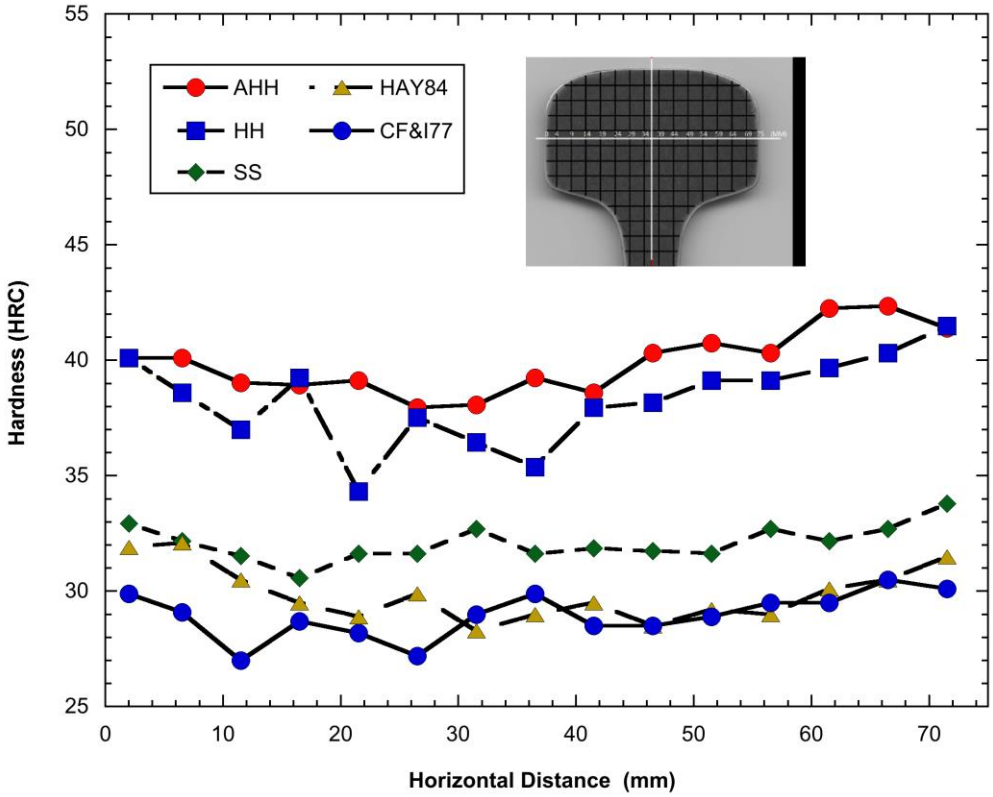

Figure 13 – HRC hardness as a function of horizontal position across the head mid-section.

3.3.4 Data Interpretation

Referring to Figure 10 above, there are clear differences in hardness values for the five rails in this study. Table 9 summarizes the hardness measurements. The average hardness for the outer 20 mm (row 1 in Table 9) is a good representation of the head material that is subject to abrasive wear in service. The legacy rails are noticeably softer than the modern rails in this important region of the heads. In particular, the AHH rail is significantly harder than even the HH rail. This finding suggests that the wear rates of the modern rails will be much lower than the legacy rails, implying that the fatigue behavior of the modern rails is more important than in the past because the modern rails will sustain longer lives, increasing the probability of fatigue crack development late in service life.

Table 9 – Representative Hardness Values of the Rails

	AHH	HH	SS	HAY84	CF&I77
20 mm Average	40.7	37.2	33.0	30.4	28.9
Maximum in Head	41.9	39.9	34.0	32.4	31.1
Overall Head Average	40.8	37.1	32.6	30.0	28.8
Web Average	35.4	32.2	33.2	29.8	29.3
Base Average	36.7	34.2	33.9	31.8	30.2

The other hardness values in Table 9 provide comparisons with the relative hardness of the outer 20 mm of the heads. For example, for all the rails the average head hardness is only slightly less than the outer 20 mm. So although the two head hardened rails exhibit some degree of hardness gradient from the surface into the head, the gradient is small, just as it is for the SS and legacy rails that were cooled in air after rolling. The hardness values in the webs of the head hardened rails, AHH and HH, are approximately 5 HRC softer than the corresponding heads, while the webs of the other rails are essentially the same as their heads. This characteristic is expected. There were no high hardness readings in the webs of any of the rails, demonstrating that the steels were not badly segregated. As expected, the bases of the two head hardened rails are 3 to 4 HRC softer than their heads, while the bases of the air-cooled rails are about 1 HRC harder than their heads.

The contour plots shown in Figure 10 suggest that there is reasonable symmetry in the hardness of all five rail heads. However, the higher resolution plots given in Figure 11 indicate that there is a degree of asymmetry, especially for the AHH rail. This condition is a consequence of the manufacturing method of rails. A typical hardness variability in the heads is observed for the five rails in this study, which leads to conclusion that the more advanced properties such as residual stress, fracture toughness, and fatigue crack growth rate reported below can be considered as representative of the rails that are in service.

In addition to the results discussed above, ArcelorMittal performed separate hardness measurement for comparison purposes with the AREMA standards. The running surface of the SS rail was 337 HB which meets the requirements of Standard Carbon Rail of 310 HB minimum hardness. The running surface of the HH rail was 384 HB which meets the 370 HB minimum hardness for High Strength Carbon Rail. The running surface of the AHH rail was 413 HB (AHH is not included in the current AREMA standards). All three modern rails comply with the hardness requirements of the AREMA rail specification.

3.4 Microstructural Observations with LOM and SEM

3.4.1 Experimental Procedure

Figure 14 shows the locations where five metallographic samples were removed from each rail, and the arrows show the viewing direction associated with each sample. Each sample was mounted in epoxy and ground to a 0.03 micrometer surface finish using colloidal silica. The samples were examined in either the as-polished or etched condition. Etching was conducted with a 2% nital solution. Examination by Light Optical Microscopy (LOM) was conducted on a Reichert Fe3 metallographic, while examination by Scanning Electron Microscopy (SEM) was conducted on a Hitachi 4300 SEM equipped with a field emission gun. Select samples were used for micro hardness measurements with a Vickers indenter and a 10 g load.

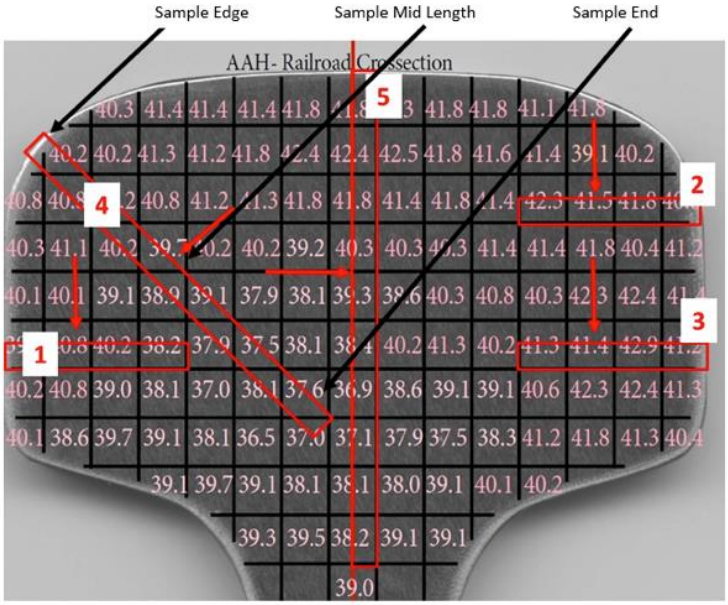

Figure 14 – The location and viewing direction of five metallography samples that were removed from each rail.

3.4.2 Results and Discussions

All five metallographic samples from each rail were initially examined along their entire viewing length. However, all samples showed similar microstructural features, so only results from Sample 4 of each rail are shown. Figures 15 through 19 show the outer edge of Sample 4 (Figure 7) for each rail. The rails exhibit a mixed ferrite/pearlite microstructure at the surface that eventually changed to a fully pearlitic microstructure with increasing distance from the rail running surface. (The white phase is the ferrite, while the darker constituent is pearlite.) The mixed ferrite/pearlite region is caused by decarburization that occurs during high temperature processing of the rails.

Figures 20 through 24 show LOM photomicrographs of the microstructure at the mid-length of Sample 4 for each rail, and similar LOM photomicrographs are shown for the end of the sample in Figures 25 through 29. (Figure 14 shows these locations.)

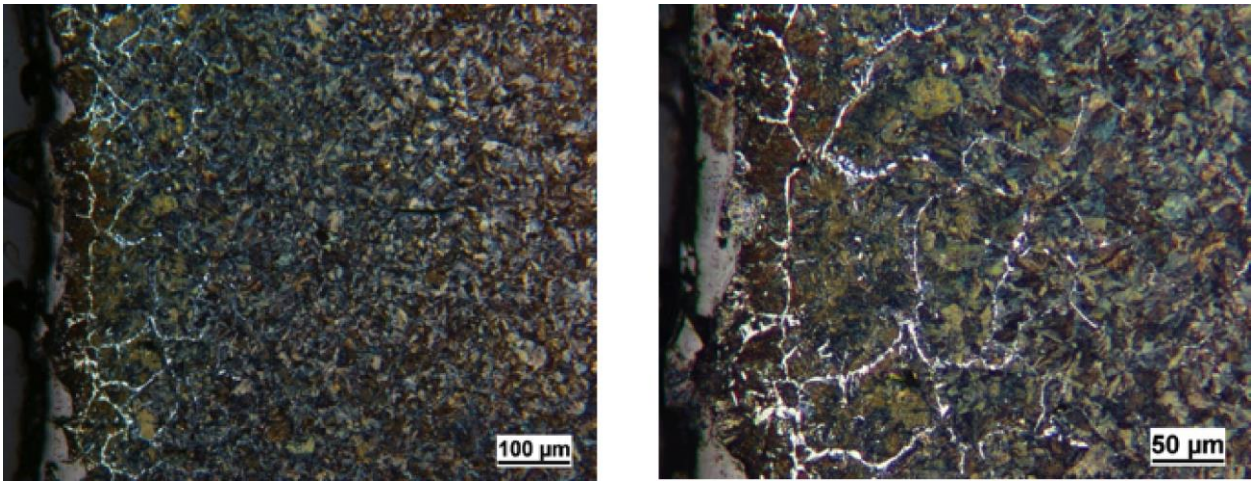

Figure 15 – LOM photomicrographs of Sample 4 from HH rail as viewed at the outer edge of the sample.

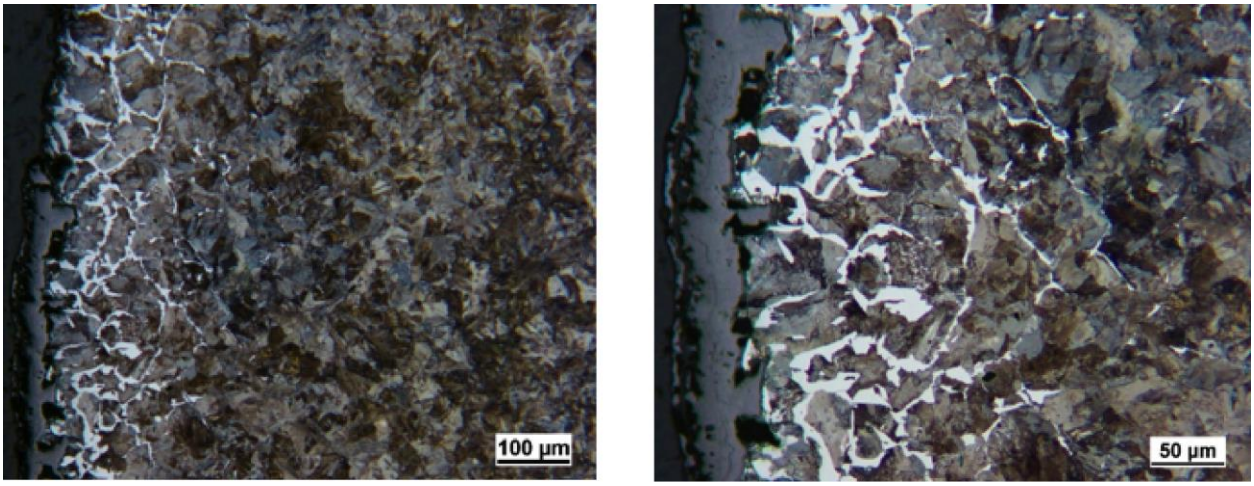

Figure 16 – LOM photomicrographs of Sample 4 from SS rail as viewed at the outer edge of the sample.

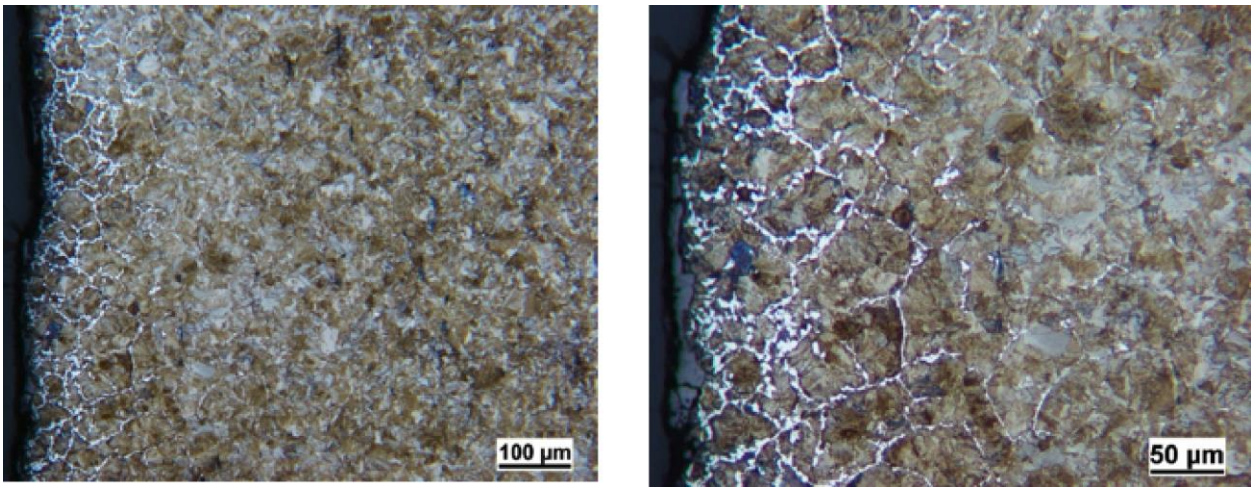

Figure 17 – LOM photomicrographs of Sample 4 from AHH rail as viewed at the outer edge of the sample.

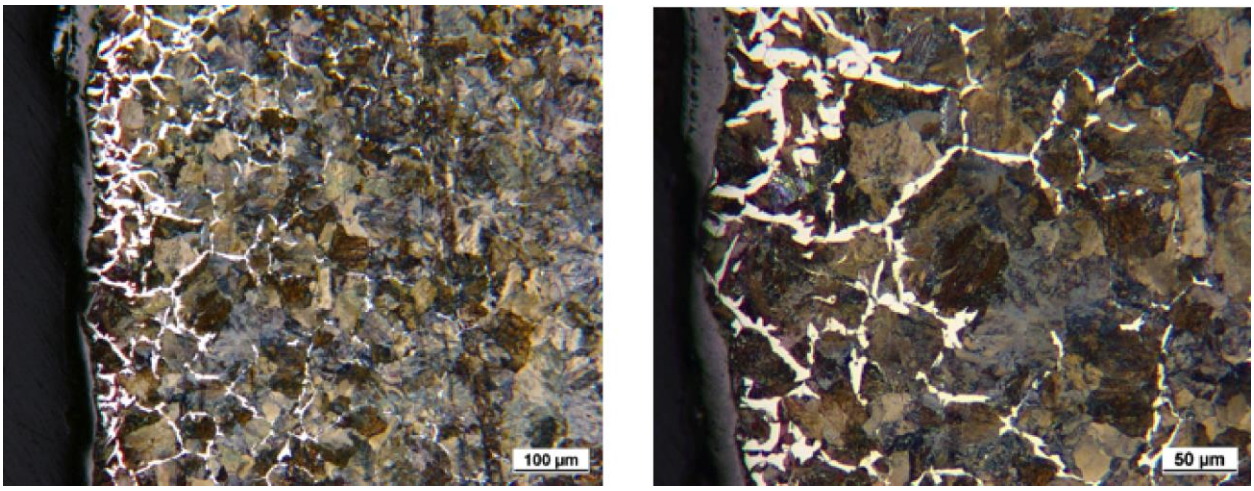

Figure 18 – LOM photomicrographs of Sample 4 from CF&I77 rail as viewed at the outer edge of the sample.

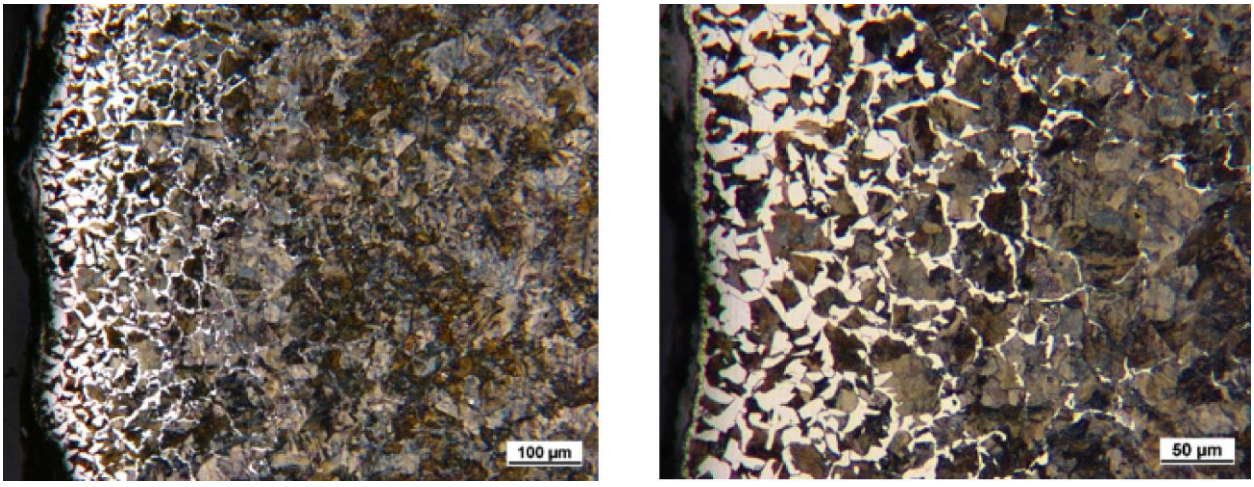

Figure 19 – LOM photomicrographs of Sample 4 from HAY84 rail as viewed at the outer edge of the sample.

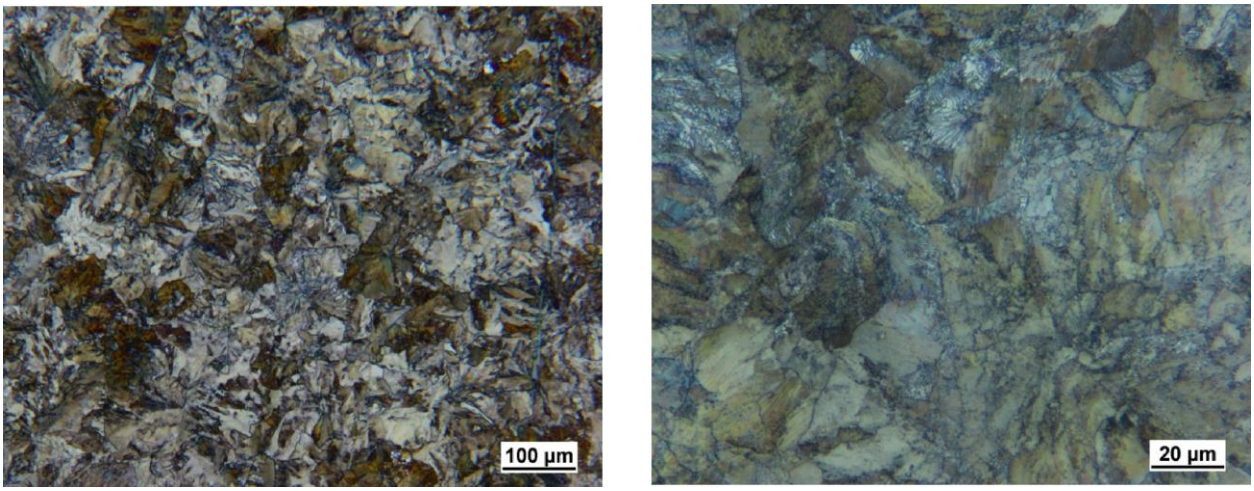

Figure 20 – LOM photomicrographs of Sample 4 from SS rail as viewed at the mid length of the sample.

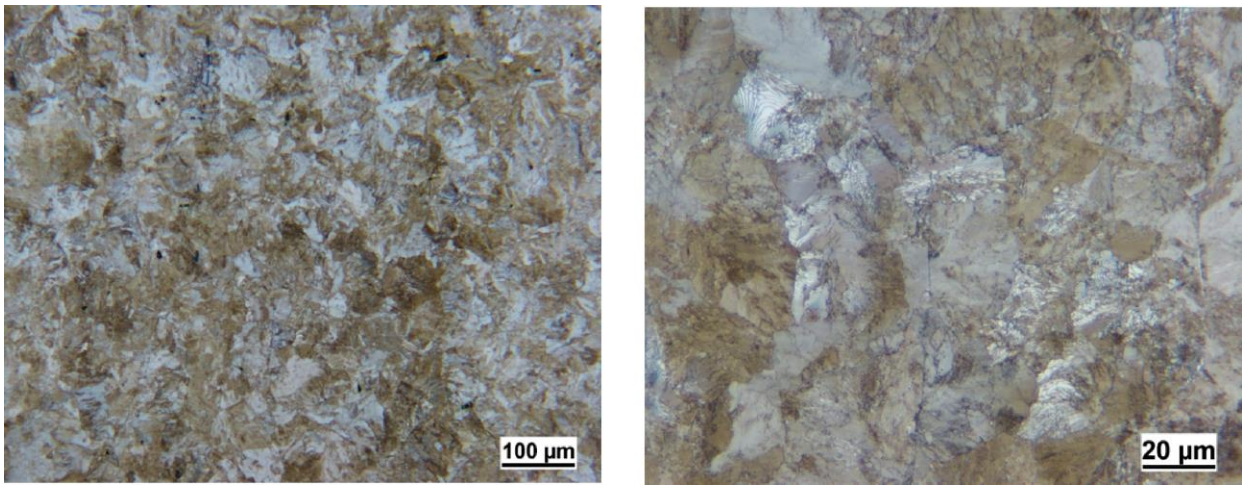

Figure 21 – LOM photomicrographs of Sample 4 from HH rail as viewed at the mid length of the sample.

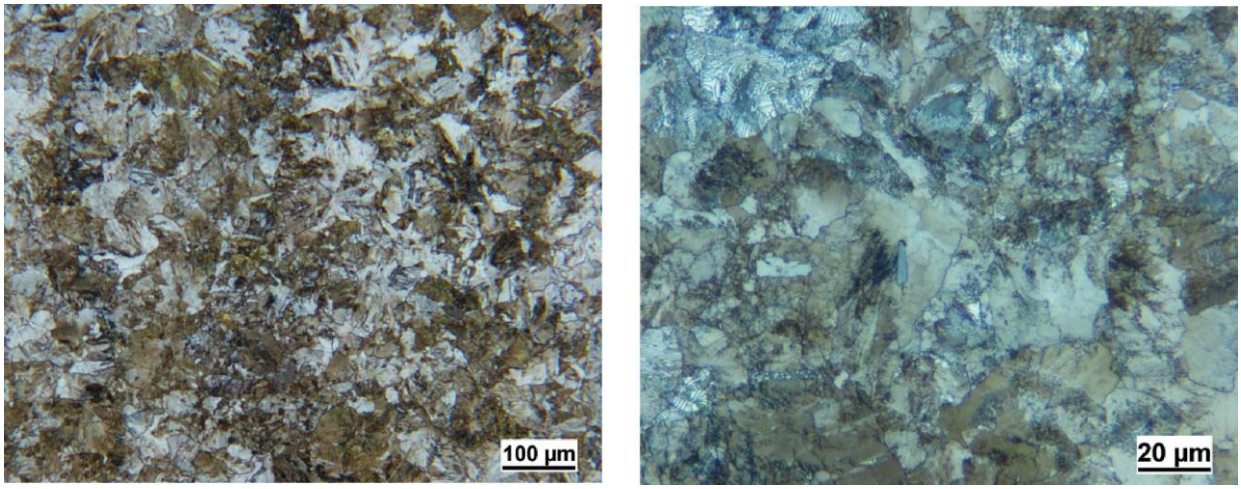

Figure 22 – LOM photomicrographs of Sample 4 from AHH rail as viewed at the mid length of the sample.

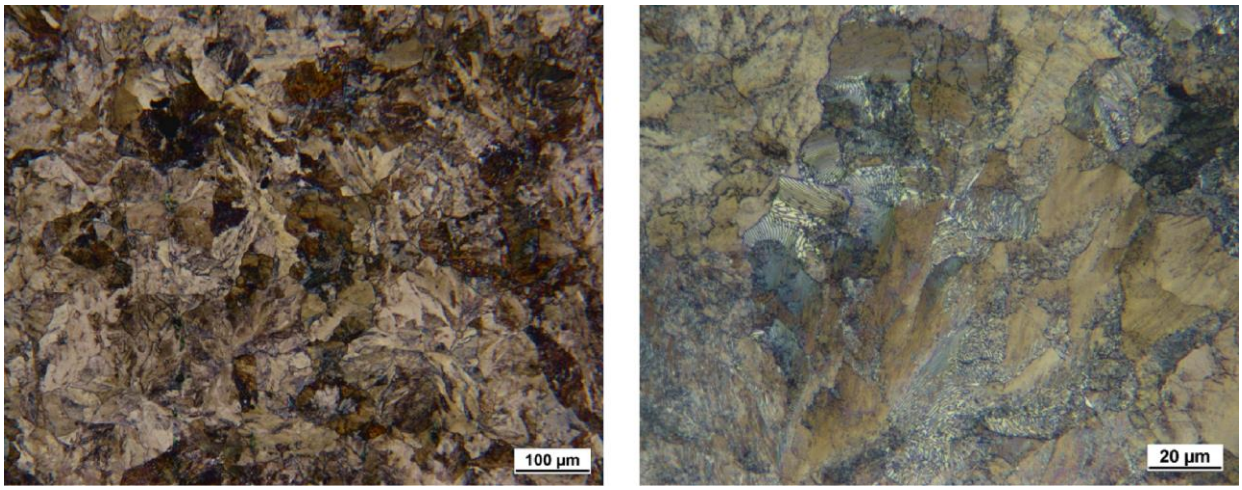

Figure 23 – LOM photomicrographs of Sample 4 from CF&I77 rail as viewed at the mid length of the sample.

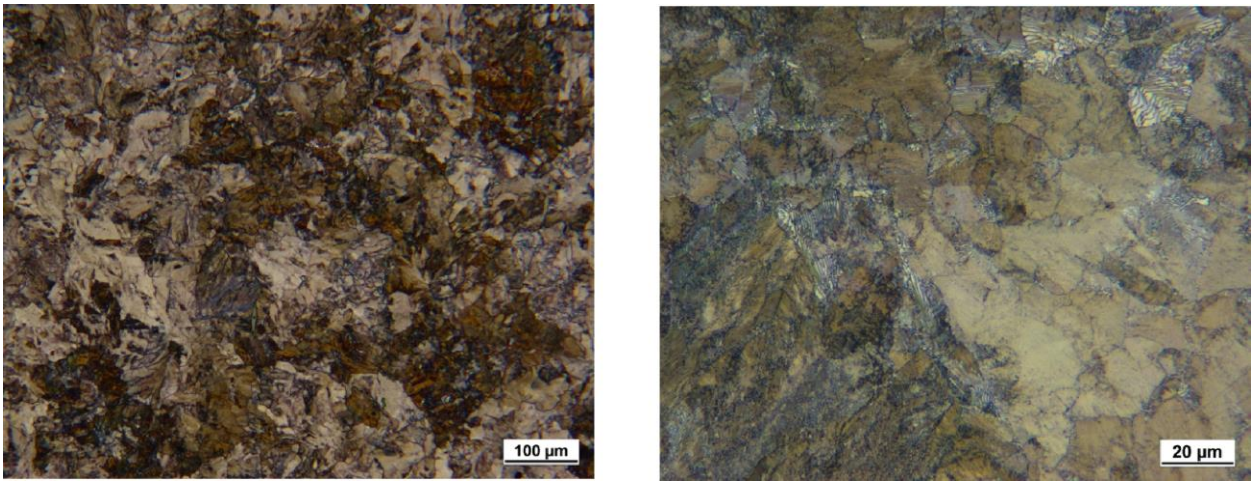

Figure 24 – LOM photomicrographs of Sample 4 from HAY84 rail as viewed at the mid length of the sample.

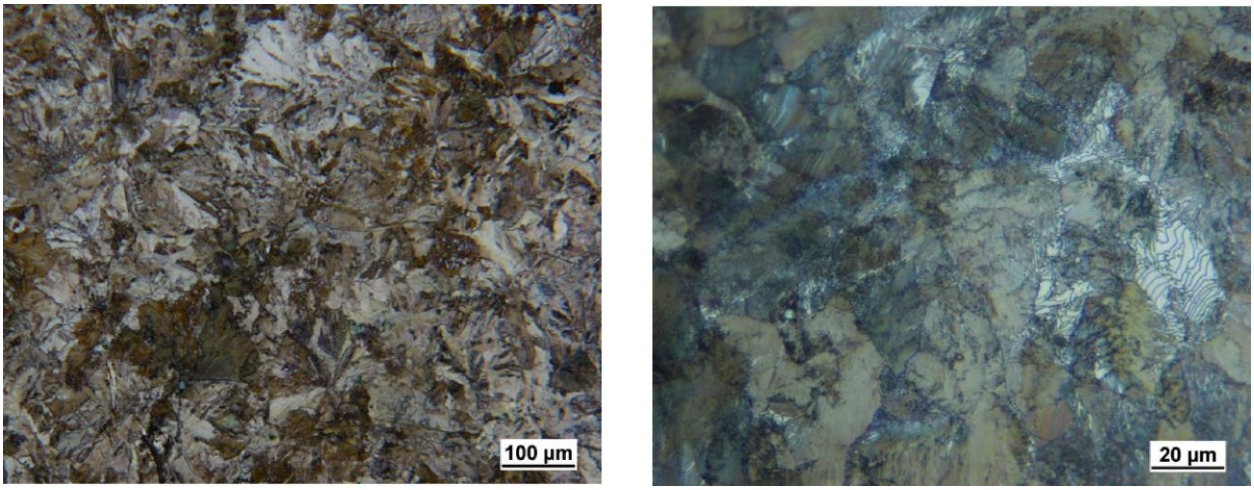

Figure 25 – LOM photomicrographs of Sample 4 from SS rail as viewed at the end of the sample.

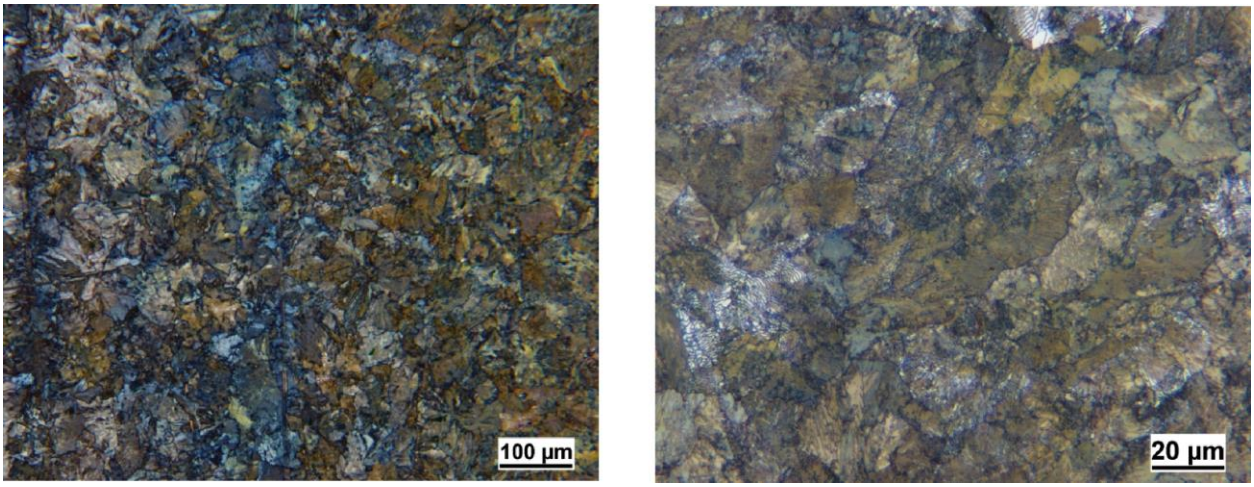

Figure 26 – LOM photomicrographs of Sample 4 from HH rail as viewed at the end of the sample.

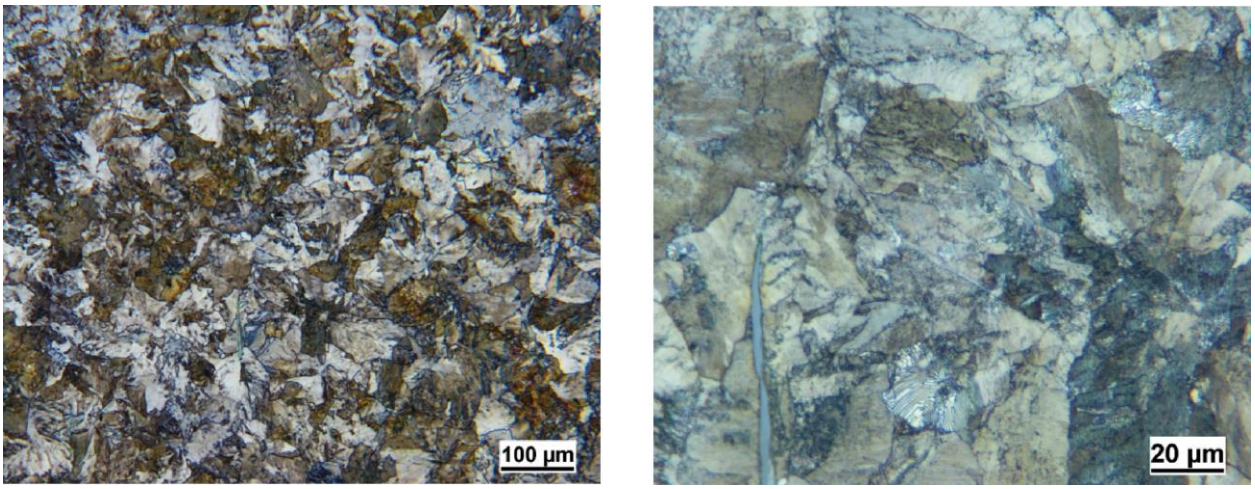

Figure 27 – LOM photomicrographs of Sample 4 from AHH rail as viewed at the end of the sample.

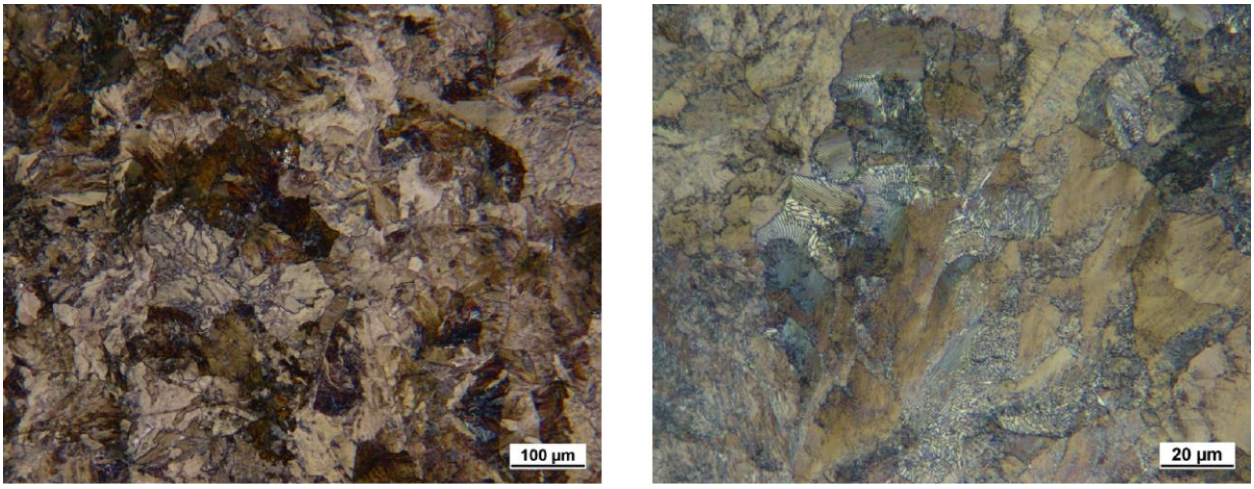

Figure 28 – LOM photomicrographs of Sample 4 from CF&I77 rail as viewed at the end of the sample.

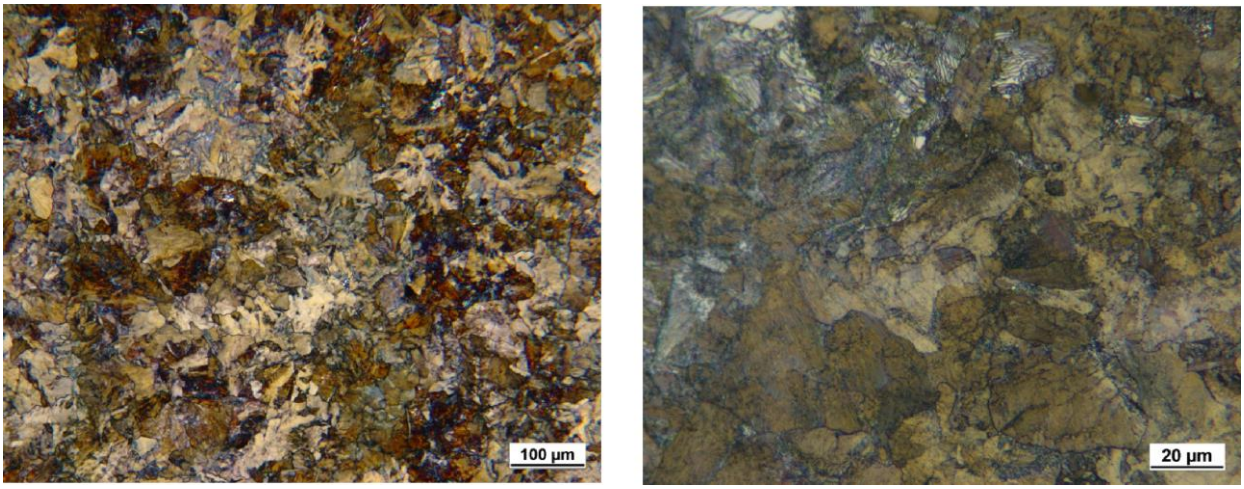

Figure 29 – LOM photomicrographs of Sample 4 from HAY84 rail as viewed at the end of the sample.

The SS, HH, and AHH rails were also examined by SEM at the same locations on Sample 4 for each rail (surface, mid-length, end), and the results are shown in Figures 30 through 38. In the low magnification SEM photographs on the left-hand side of Figs. 30 through 32, the pro-eutectoid ferrite appears as dark bands (example labeled in Fig. 30). Examples of the ferrite and pearlite are labeled for the SS rail in the higher magnification image on the right-hand side of Fig. 30, where the two phase cementite and ferrite mixture of the pearlite is readily resolved.

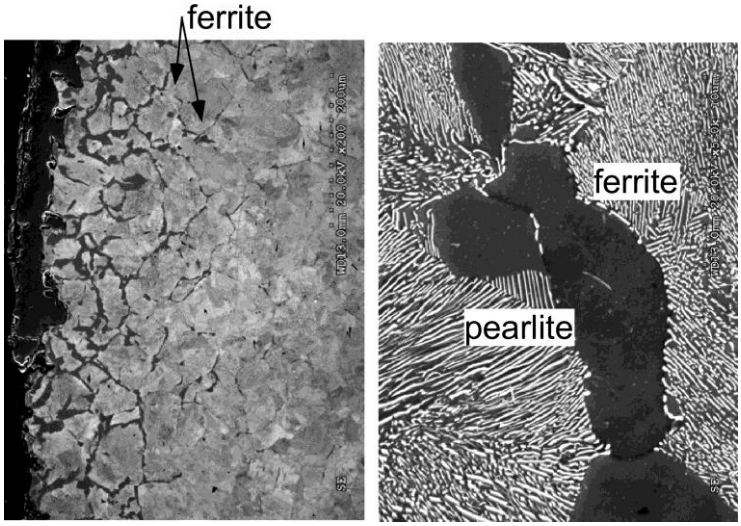

Figure 30 – SEM photomicrographs of Sample 4 from SS rail as viewed at outer edge of sample.

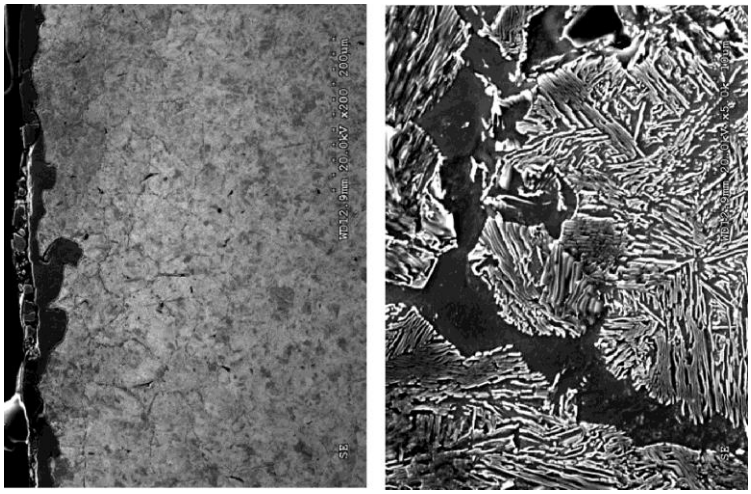

Figure 31 – SEM photomicrographs of Sample 4 from HH rail as viewed at outer edge of sample.

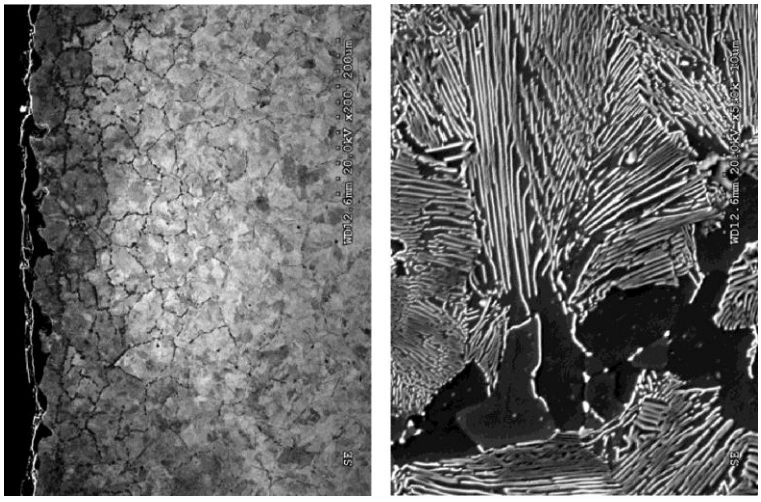

Figure 32 – SEM photomicrographs of Sample 4 from AHH rail as viewed at outer edge of sample.

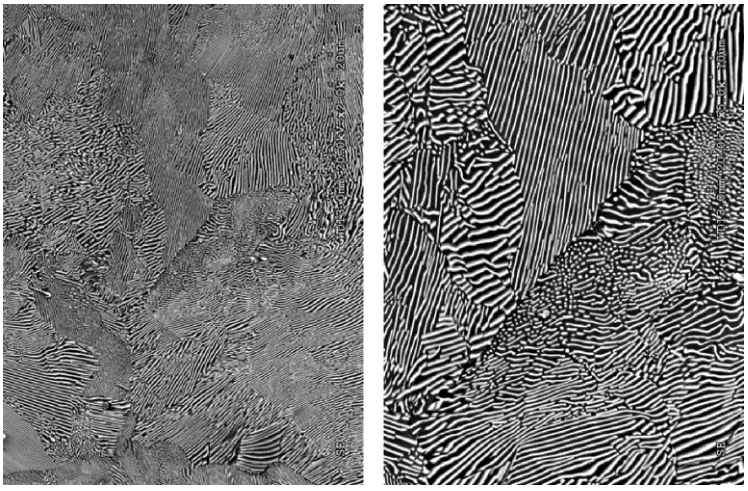

Figure 33 – SEM photomicrographs of Sample 4 from SS rail as viewed at mid length of sample.

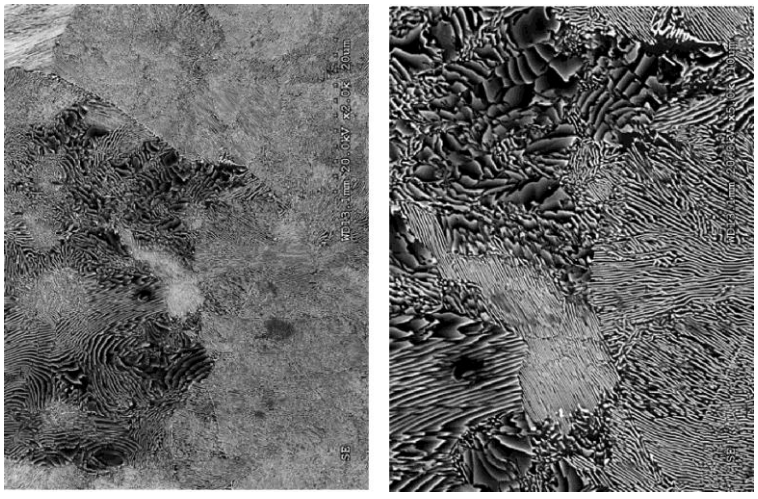

Figure 34 – SEM photomicrographs of Sample 4 from HH rail as viewed at mid length of sample.

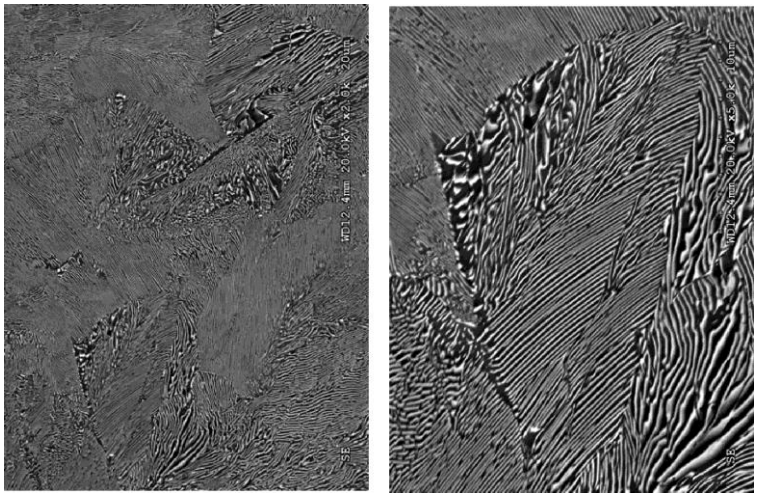

Figure 35 – SEM photomicrographs of Sample 4 from AHH rail as viewed at the mid length of the sample.

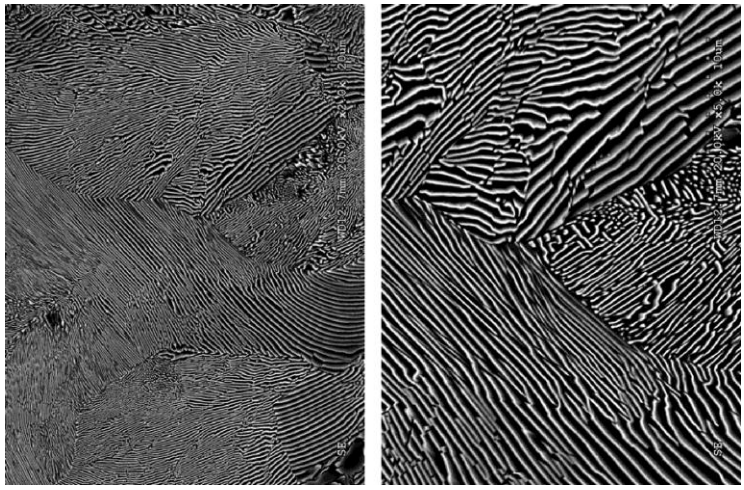

Figure 36 – SEM photomicrographs of Sample 4 from SS rail as viewed at the end of sample.

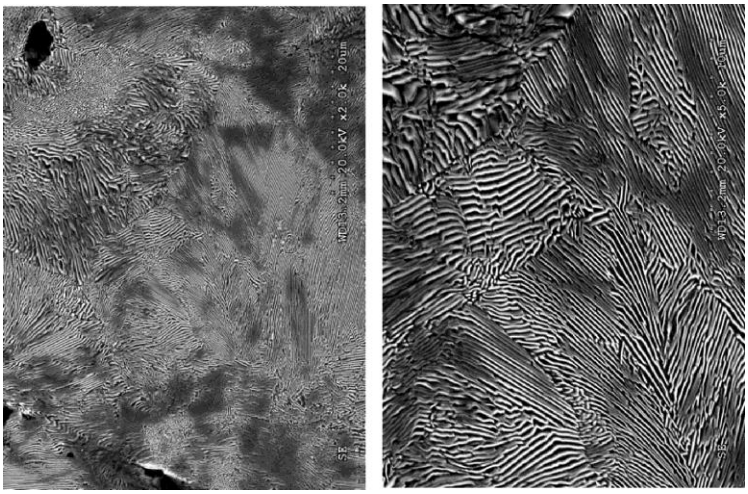

Figure 37 – SEM photomicrographs of Sample 4 from HH rail as viewed at the end of sample.

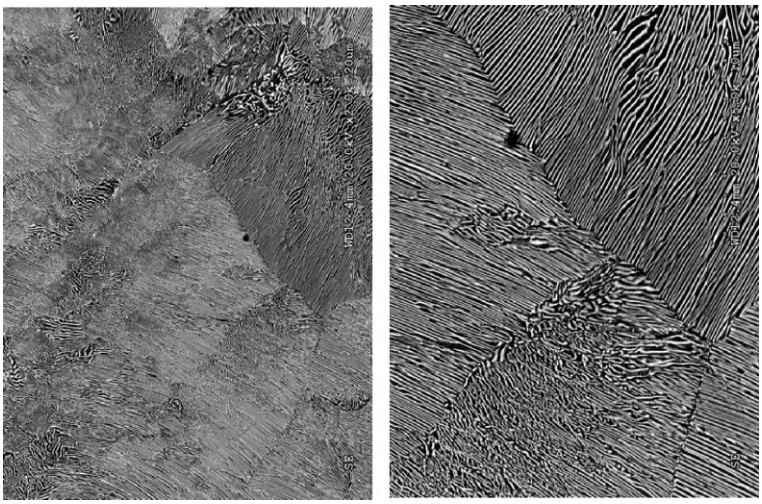

Figure 38 – SEM photomicrographs of Sample 4 from AHH rail as viewed at the end of sample.

Figures 39 through 41 show the results of microhardness traces conducted from the surface to the interior of Sample 4 for the SS, HH, and AHH rails. As expected, the decarburization layer at the surface results in a local decrease in hardness that is on the order of about one millimeter in length.

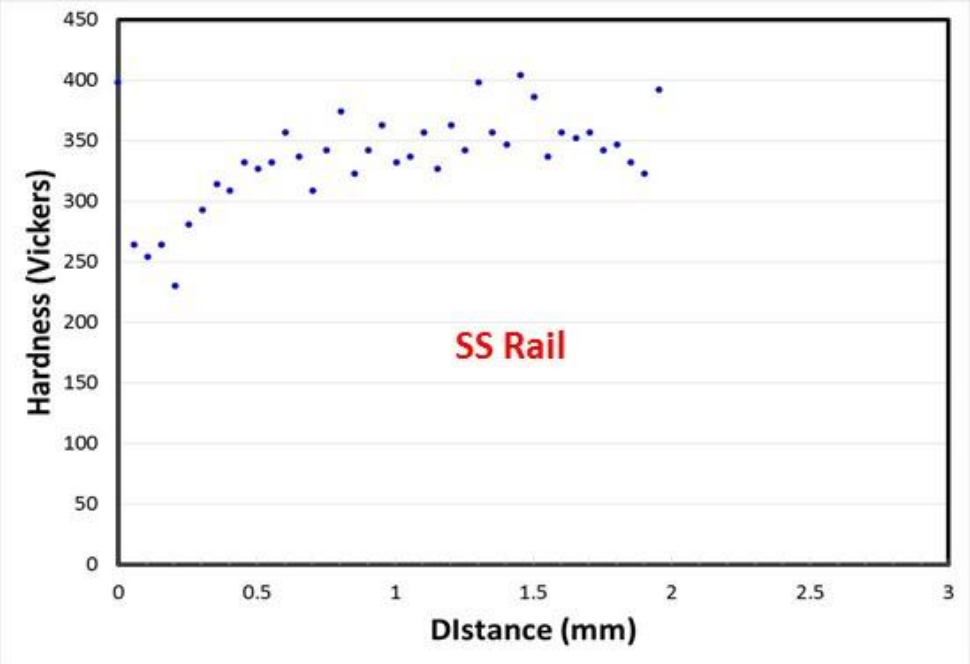

Figure 39 – Variation in microhardness near the outer edge of the SS rail for Sample 4.

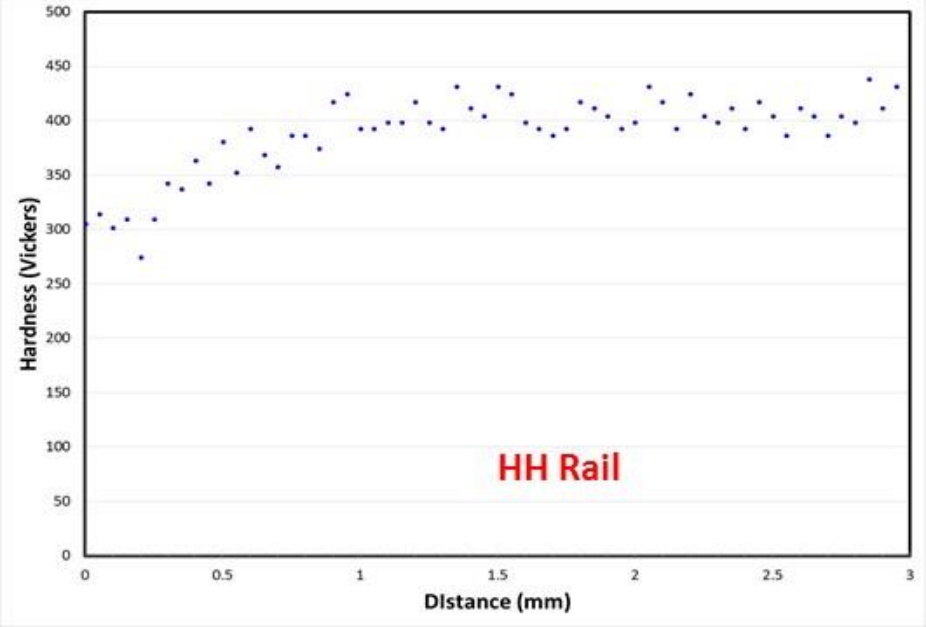

Figure 40 – Variation in microhardness near the outer edge of the HH rail for Sample 4.

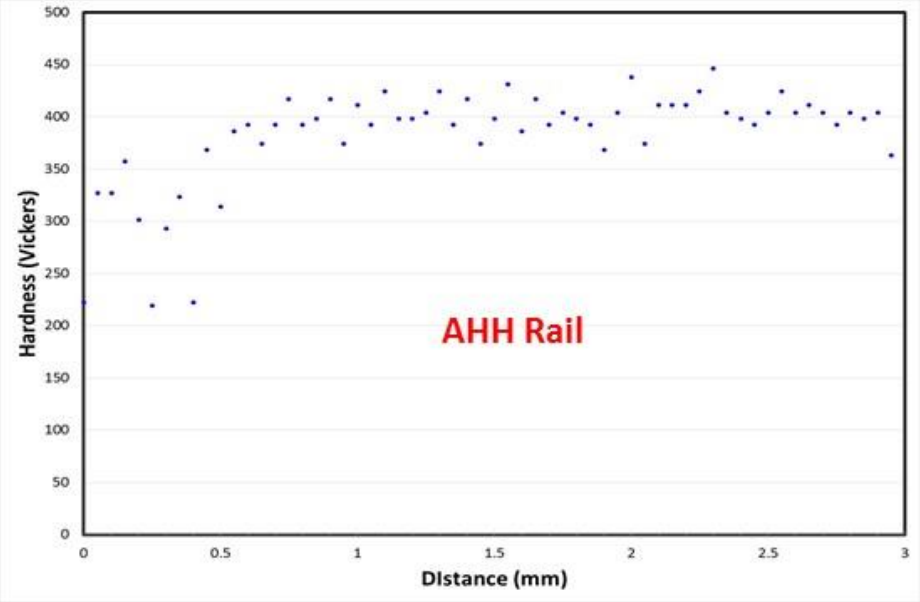

Figure 41 – Variation in microhardness near the outer edge of the AHH rail for Sample 4.

Inclusions were also observed in the rails, and an example is shown in the LOM images of Figure 42 that were acquired in the as-polished condition for Sample 4 on the SS rail. Two types of inclusions were observed. One inclusion type had a grey color and was elongated in the longitudinal direction of the rail. The second type of inclusion exhibited an orange appearance and was more equiaxed in shape.

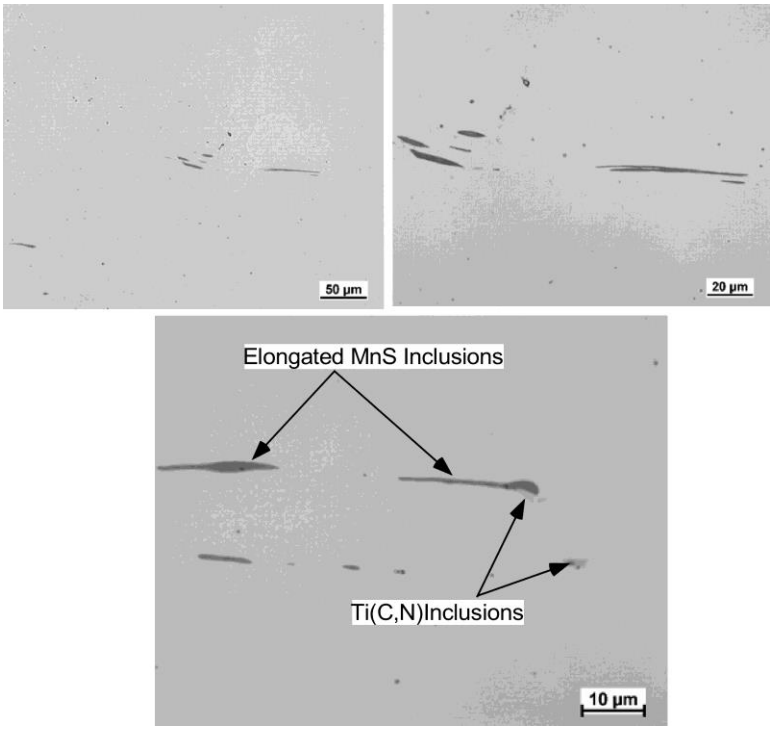

Figure 42 – LOM images acquired in as-polished condition showing typical inclusions observed in rails (Sample 4, SS Rail).

Higher magnification SEM images and Energy Dispersive Spectrometry (EDS) spectra of these phases are shown in Figures 43 and 44 (the red + sign in the SEM images denote the locations where the EDS spectra were acquired). The elongated particles are enriched in manganese (Mn) and sulfur (S), while the equiaxed particles are enriched in titanium (Ti). The elongated inclusions are MnS inclusions that are typically observed in steel. The Ti rich inclusions are likely titanium carbo-nitrides that form from the melt at the start of solidification of the ingot. The MnS inclusions are elongated along the length of the rail (i.e., perpendicular to the fatigue crack growth plane) and are therefore unlikely to have any significant effect on fatigue resistance. Similarly, the Ti rich inclusions are equiaxed and present in very small quantities, and therefore also unlikely to have any detrimental effect on fatigue properties.

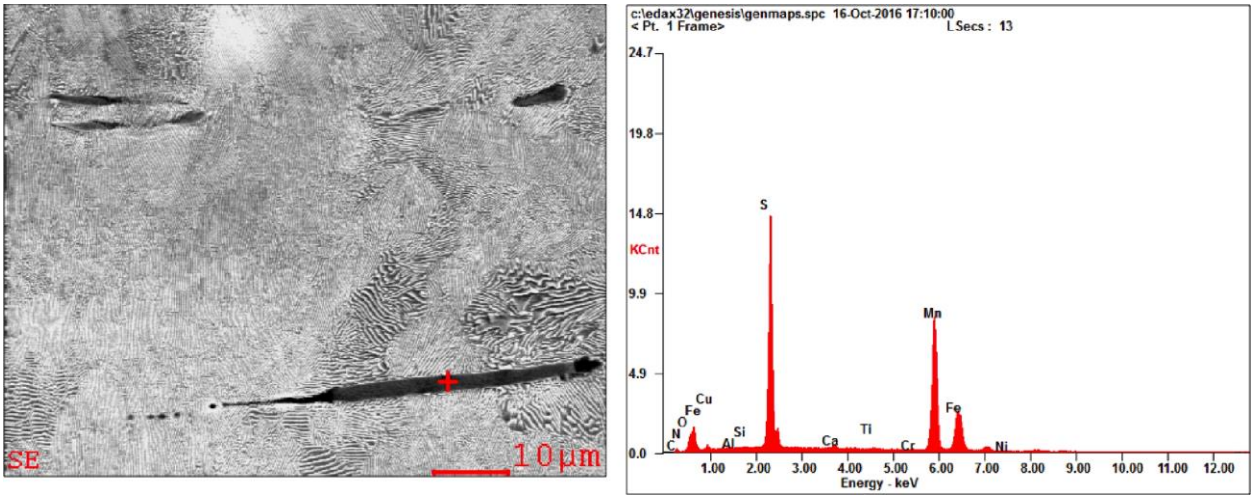

Figure 43 – SEM photomicrograph (left) and corresponding EDS spectrum (right) of typical MnS inclusions observed in rails (SS Rail, Sample 4).

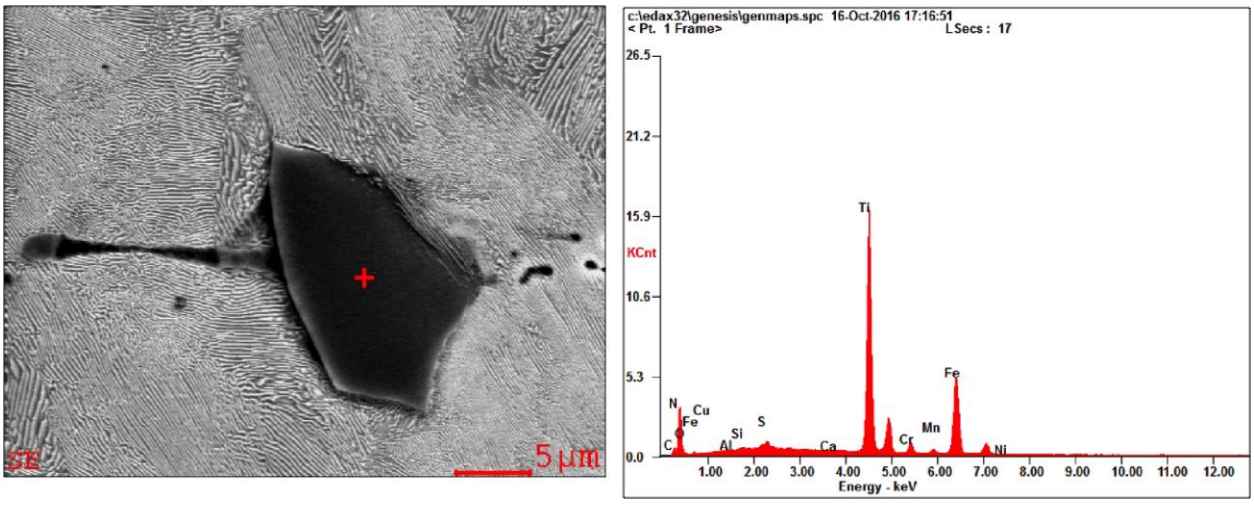

Figure 44 – SEM photomicrograph (top) and corresponding EDS spectrum (bottom) of typical Ti rich inclusions observed in rails (SS Rail, Sample 4).

The chemical composition of the rails is designed to produce a fully pearlitic microstructure. The mixed ferrite/pearlite microstructure associated with the surface of the rail is associated with decarburization that occurs during high temperature processing. This decarburization results in a local depletion of carbon near the surface. As a result of this local reduction in carbon

concentration, pro-eutectoid ferrite precipitates from austenite during cooling. Formation of the pro-eutectoid ferrite results in progressive carbon enrichment of the austenite during the austenite-to-ferrite transformation. The austenite-to-ferrite transformation continues until the remaining austenite is finally enriched to the eutectoid composition, at which point the remaining austenite transforms to pearlite. This accounts for the mixed ferrite/pearlite microstructure observed at the rail surfaces. The ferrite is softer than the pearlite due to reduced carbon and the associated absence of the hard cementite phase, and this accounts for the reduced hardness observed within the decarburized layer at the surface. Beyond the decarburized region, the carbon content of the rail is at the eutectoid composition, and the austenite transforms fully to pearlite during cooling from the processing temperature.

The hardness and strength of pearlite increases with decreasing pearlite spacing. The pearlite spacing, in turn, is controlled primarily by the cooling rate during the austenite-to-pearlite transformation and the alloy content of the steel. Higher cooling rates and additions of substitutional alloying elements such as vanadium (V) and titanium (Ti) decrease the pearlite spacing. (It should be noted that accurate pearlite spacing measurements require extensive sampling and measurements that were beyond the scope of this project.) During cooling of the rail from the processing temperature, the cooling rate will be highest at the surface and decrease with increasing distance from the surface. This variation in cooling rate accounts for the relatively high hardnesses observed near the rail surfaces and decrease in hardness with increasing distance from the surface. Of the modern rails, the SS rail exhibited the lowest hardness and strength, followed by increasing hardness/strength for the HH and then AHH rails. These differences can be attributed to the higher alloying elements (V and Ti) associated with these rails. During the austenite to pearlite transformation, the alloying elements must partition between the ferrite and cementite phases, and this process is diffusion controlled. The diffusion rate of the relatively larger V and Ti substitutional alloying elements is significantly slower than that of carbon, which diffuses interstitially. As a result, the diffusion distance during the austenite-to-pearlite transformation is reduced with the addition alloying elements, which reduces the pearlite spacing. This likely accounts for the higher hardness and strength observed for the HH and AHH rails.

3.5 Tensile Testing

Uniaxial tensile tests were conducted on the modern rails (AHH, HH, and SS) and legacy rails (HAY84, CF&I77), to compare uniaxial tensile properties among the different rail types and check for possible correlations with microstructural observations and residual stress measurements.

3.5.1 Sample Preparation

Uniaxial tensile specimens were machined from nine different ¼ in. thick plates, cut from each of the rail cross sections, as shown in Figure 45. The flat tensile test specimens were prepared in accordance with ASTM E8 standards using 1 in. gauge lengths. The other dimensions for the tensile specimen are given in Table 10. The tensile specimens were cut from long plates that were oriented with respect to the rails' primary axis, plates that may have contained significant internal residual stresses in the axial direction. However, it's believed that the residual stresses in the gauge length of the tensile specimens were minimal due to the relatively small thickness and width dimensions (6 mm x 6 mm) in the gauge length.

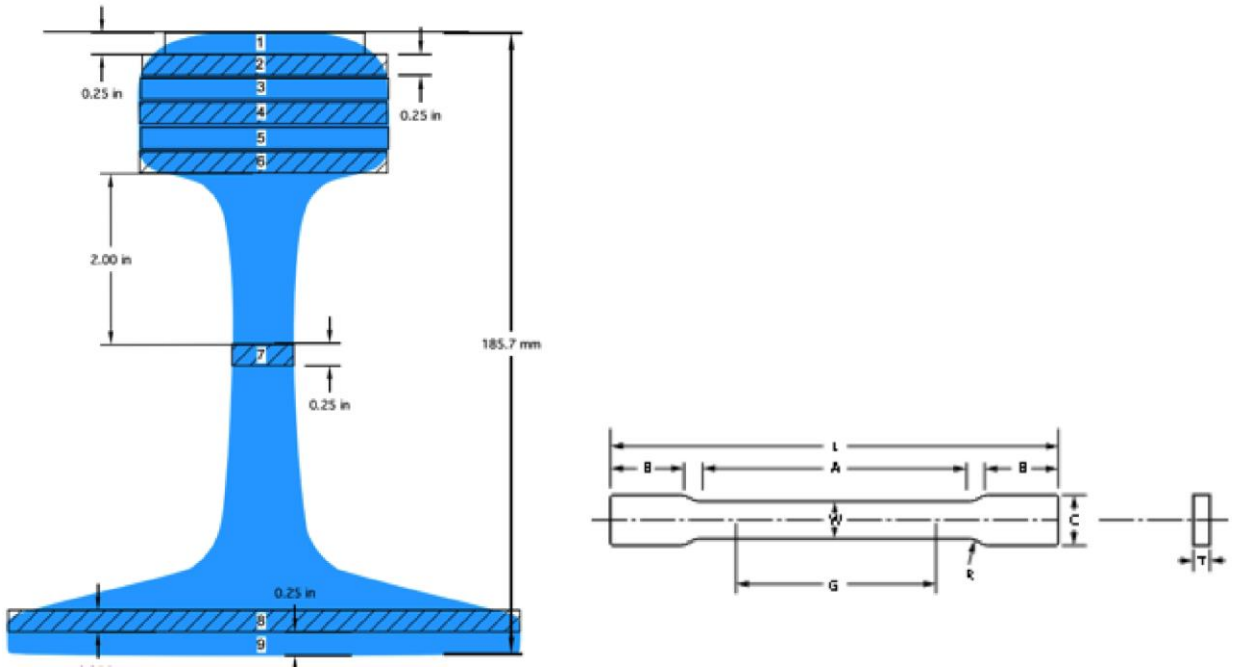

Figure 45 – ASTM E8 tensile specimens cut from specific vertical locations in 136RE rails.

Table 10 – Tensile Specimen Dimensions

	G Gauge Length	W Width	T Thickness	R Radius of fillet	L Overall Length	B Length of Grip	C Width of grip
Specimen Dimensions mm [in.]	25 [1]	6 [0.25]	6 [0.25]	6 [0.25]	100 [4]	30 [1.25]	10 [0.375]

3.5.2 Uniaxial Stress-Strain Curves

A total of 45 tensile tests were conducted (5 rails, 9 tensile specimens per rail). In these tests the engineering stress (force per unit original undeformed area) and engineering strain ($\Delta L / L$) within the gauge length, measured using a clip-on extensometer, were recorded. As described in Appendix B, Figure 119, the standard "offset method" was used to determine the tensile yield strength in accordance with the ASTM E8 standards. The individual stress/strain curves, taken from layer #2 for each of the rail heads (see Fig. 45), are given in Figs. 120 - 124. Figure 46 compares the uniaxial tensile behavior from all of these tests on a single plot. As can be seen, the modern head hardened rails (AHH, HH) exhibit significantly higher yield and ultimate tensile strength. Figure 47 shows the variation in the uniaxial yield strength as a function of depth from the surface of the rail head for the five rails. The AHH rail exhibited the highest yield strength at all depths. The yield strength close to the AHH's running surface is approximately 345 MPa (50 ksi) greater than the yield strength observed in the CF&I77 rail at the same location. It's also interesting to note the variation in the yield strength between the head region and the base for all of the rails. For example, in the AHH rail, the yield strength decreased from a maximum of 862 MPa (125 ksi) slightly below the running surface, to a yield strength of 689 MPa (100 ksi) in the rail base.

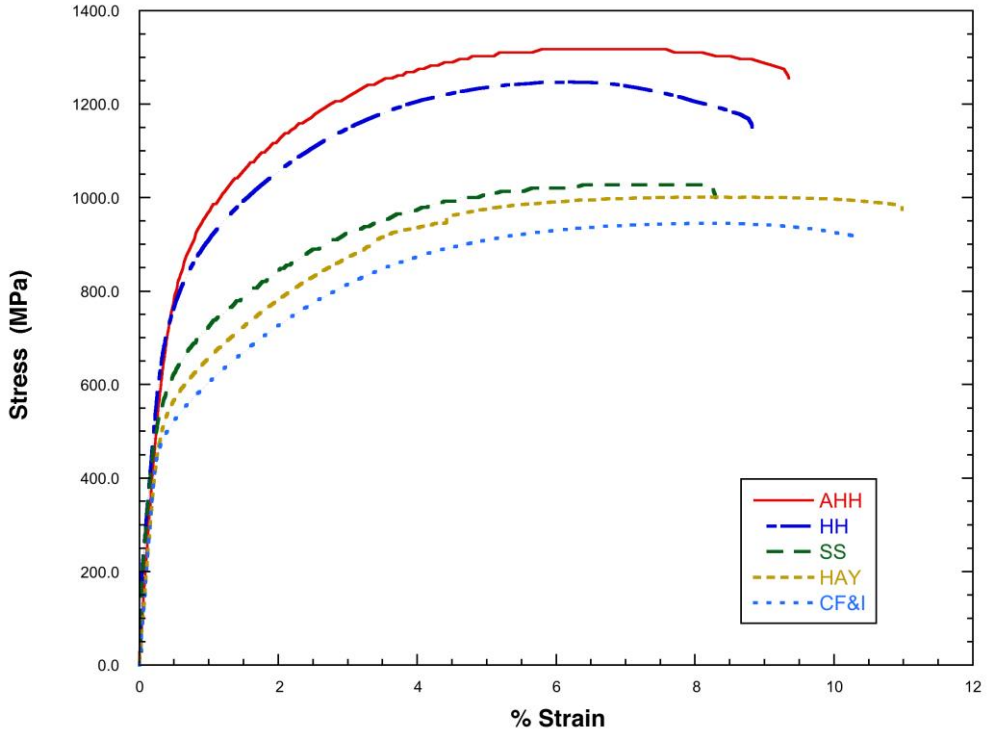

Figure 46 – Comparison of uniaxial tensile behavior at a specific location (layer #2) for all rails.

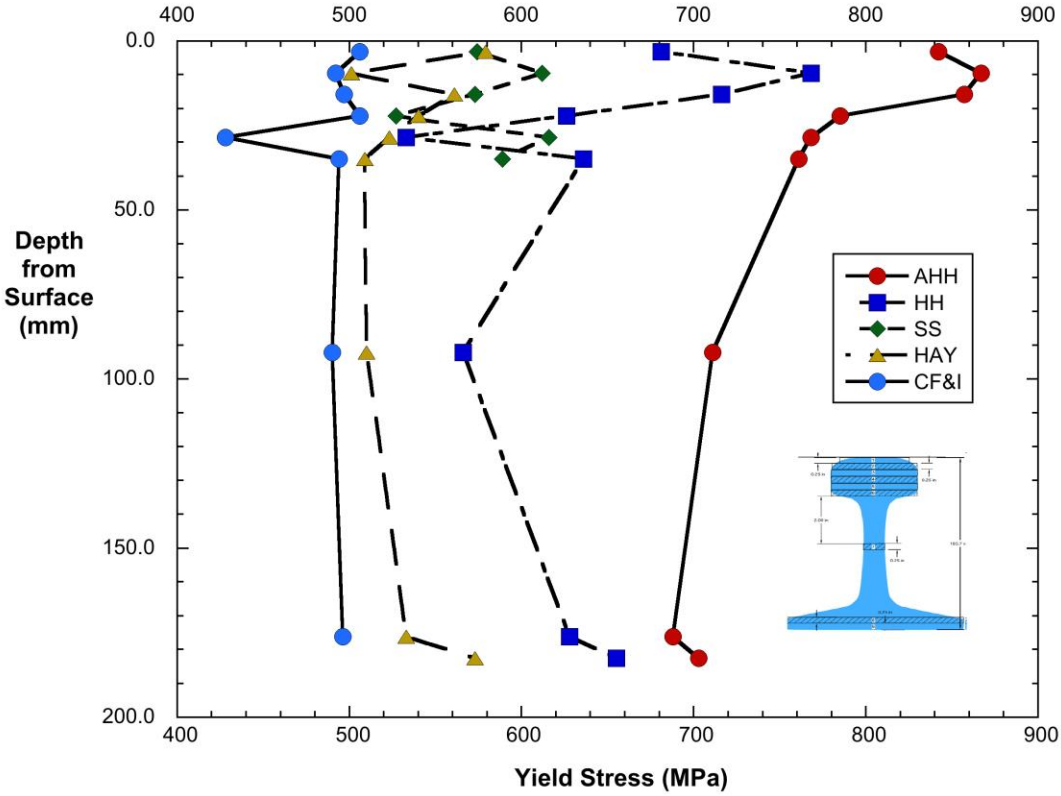

Figure 47 – Uniaxial yield stress as a function of depth measured from the rail head running surface.

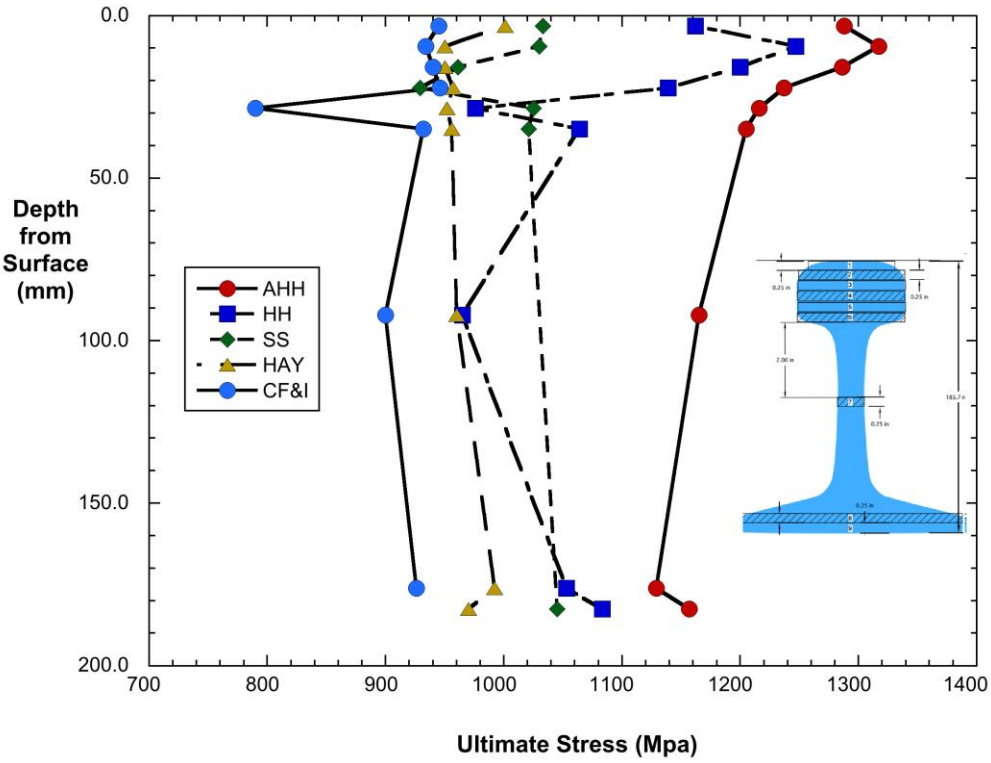

Figure 48 – Ultimate tensile strength as a function of depth measured from the rail head running surface.

As observed in Fig. 48, the ultimate tensile strength has a spatial variation with respect to depth that is very similar to that seen in the yield strength plot (Fig. 47). As expected, the greatest ultimate tensile strength was measured close to the surface of the AHH rail, with a maximum ultimate strength > 1,310 MPa (190 ksi). For comparison, the legacy rails (HAY84, CF&I77) exhibited ultimate tensile strengths generally below 965 MPa (140 ksi) in the rail head.

Both yield and tensile strength data collected here was compared to previously collected data documented by Orringer et al. [35]. In all cases, the results obtained here are consistent with the past results, except in the case of the AHH rail, which exceeds strength of previously investigated rails [35]. In addition, tensile tests of modern rails were conducted by AM following the AREMA specification for rails (including specimen locations). The SS rail had a yield strength of 690 MPa (100 ksi), a tensile strength of 1100 MPa (160 ksi), and an elongation of 9%, which meets the AREMA standard for Standard Strength Carbon Rail Steel. The HH rail exhibited a yield strength of 880 MPa (128 ksi), a tensile strength of 1310 MPa (190 ksi), and an elongation of 10 %. These measurements confirmed that the HH rail meets the AREMA High-Strength Carbon Rail requirements (830 MPa (120 ksi) minimum yield strength, 171 ksi (1180 MPa) minimum tensile strength, and 10 % minimum elongation). Finally, the AHH rail used in this study had a yield strength of 960 MPa (139 ksi), a tensile strength of 1380 MPa (200 ksi), and an elongation of 10 %, all of which are typical for this high-strength rail.

3.6 Fracture Toughness Testing Equation Chapter 2 Section 6

A prime objective in this study was to measure the fracture toughness of different rail types and determine the variation in the fracture toughness with respect to position and orientation in the rail head.

3.6.1 Specimen Preparation

The majority of the fracture and fatigue tests conducted in this study utilized compact tension (CT) test specimens as shown in Figure 49. The test specimens were prepared following ASTM E399 and E647 standards. For valid fracture toughness (K_{IC}) measurements, conditions of small scale yielding must be maintained. This is ensured by using a test specimen with sufficient thickness to maintain plane strain conditions along the bulk of the crack front. The size of the yield zone at the crack tip depends on the magnitude of K_{IC}, as well as the uniaxial yield strength σ_Y. Thus, it is not possible to know in advance whether a fracture toughness test is valid until after a provisional K_{IC} has been measured and a check made to ensure that conditions of small scale yielding have been satisfied. The ASTM requirements for valid plane strain fracture toughness measurements are:

$$a \geq 2.5\left(\frac{K_{IC}}{\sigma_Y}\right)^2 \tag{2.6.1}$$

$$B \geq 2.5\left(\frac{K_{IC}}{\sigma_Y}\right)^2 \tag{2.6.2}$$

$$W \geq 5.0\left(\frac{K_{IC}}{\sigma_Y}\right)^2 , \tag{2.6.3}$$

where a is the distance from the center of the pin holes to the crack tip, B the specimen thickness, and W the width distance from the pin holes to the back edge of the specimen. Based on previously reported values for rail fracture toughnesses, it was assumed that the largest K_{IC} values would most likely be less than 40 $\mathrm{MPa}\sqrt{\mathrm{m}}$. The uniaxial yield strength, as reported in Section 2.5, was estimated to be no less than 552 MPa and in most cases was considerably higher, e.g., the yield strength for the AHH rails is always greater than 690 MPa. Thus, a conservative thickness dimension suitable for the fracture toughness tests in this study was estimated to be 13 mm. The resulting overall dimensions for the main CT specimen used in the testing program is shown in Fig. 49.

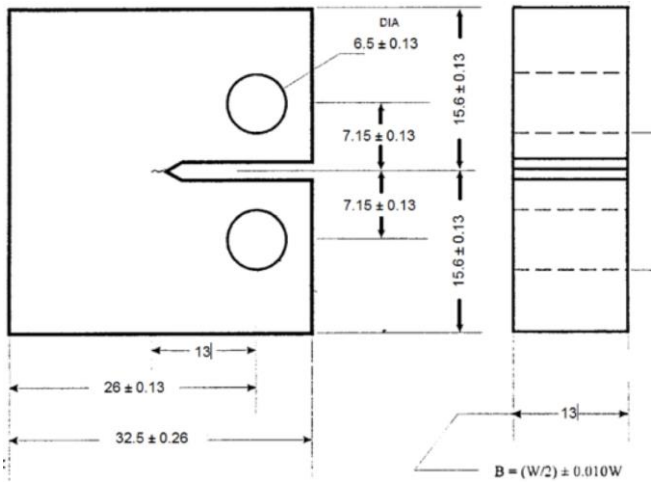

Figure 49 – Compact tension (CT) specimen (Dimensions in mm).

In an effort to determine the fracture toughness and fatigue behavior as a function of position and orientation in the five different rails examined, specimens were cut in both horizontal and vertical orientations. For example, Figure 50 shows the orientation of CT specimens machined from horizontal plates cut at different depths within the rail head. Specimens were extracted along the center of the rail and to the left and right of center by waterjet cutting the specimens from plates of specified thickness as shown in Figure 51. The specimen layout shown in Fig. 50 permitted fracture measurements both as a function of depth and lateral (off-center) position within the rail head. The relatively small size of the CT specimens minimized the magnitude of the residual stresses normal to the crack surface and thus the fracture measurements obtained with these specimens are primarily a function of local metallurgical properties and orientation.

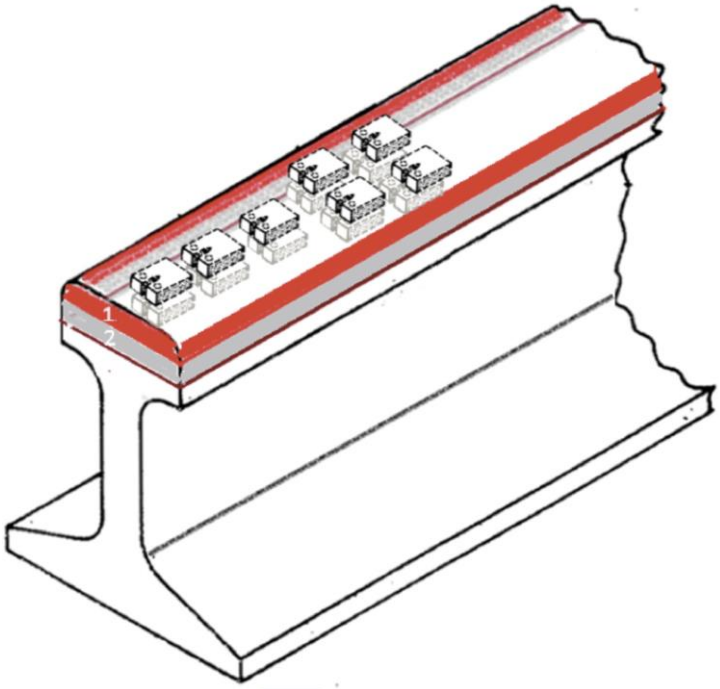

Figure 50 – Orientation of CT specimens cut from horizontal slices in the rail head.

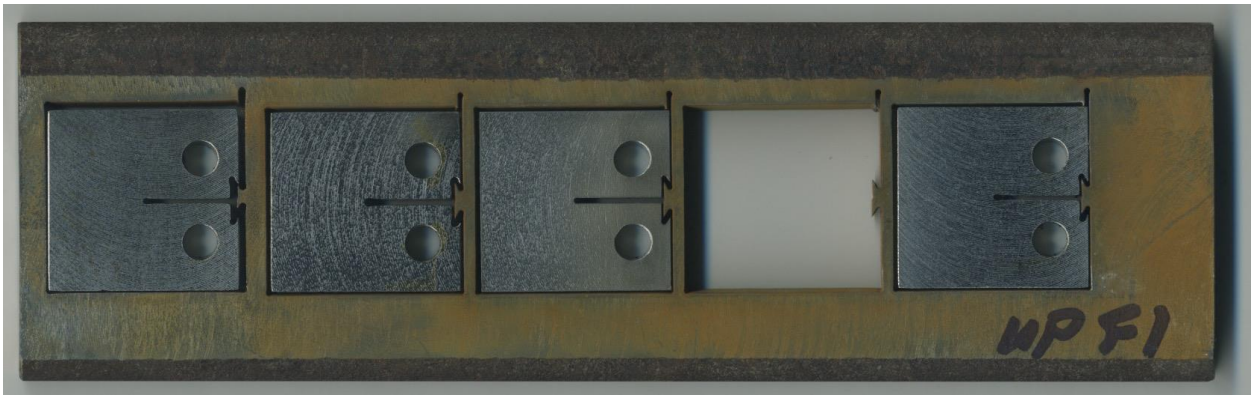

Figure 51 – Single column of CT specimens waterjet cut from region close to the rail head running surface.

Additional machining steps included milling the CT specimens to obtain flat surfaces, boring the pin loading holes, and cutting the notch. In the initial phases of the test program, notches were cut with a very fine (0.006 in.) diameter wire (EDM). However, it was determined that waterjet cut notches (notch widths between 0.020 – 0.030 in.) were perfectly acceptable for the precracking process, especially if a fine jewelers saw (blade width 0.012 in.) was used to make a fine saw cut at the base of the waterjet cut notch as shown in Figure 52. All CT fracture specimens were precracked in fatigue to obtain a precrack length of $a = 12.5$ mm using a constant amplitude sine loading with a maximum load of 4000 N and a minimum load of 400 N at a frequency of 15 – 20 Hz. Figure 53 shows a polished CT specimen with a close-up image showing the fatigue crack growth from the tip of the notch. The photomicrograph in Figure 54 also clearly shows the precrack from the notch tip in a CT specimen.

Figure 52 – Cutting sharp notch at the base of waterjet cut notch using jeweler's saw.

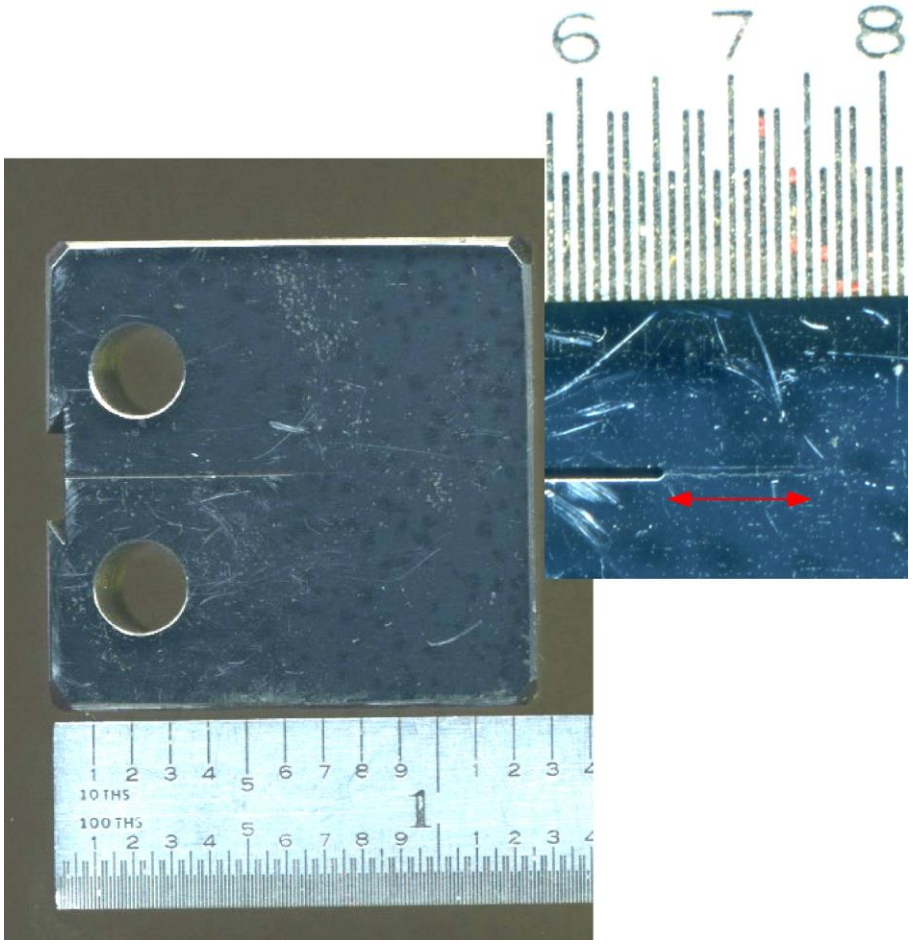

Figure 53 – CT specimen with wire EDM notch and polished surface. Inset shows ~0.1 in. fatigue precrack at base of notch.

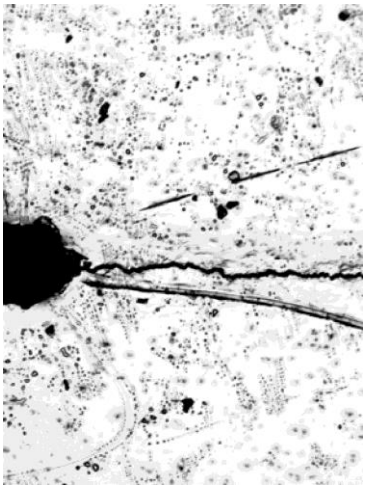

Figure 54 – Photomicrograph showing precrack from notch tip in CT specimen.

Following the ASTM E399 fracture toughness testing protocol, the load and crack opening displacement (COD) were monitored during the test to detect the proper type of crack "pop in" and advance that will ensure a valid K_{Ic} measurement. Figure 55 shows a typical CT specimen

with the attached COD clip gauge during fracture toughness testing. Appendix C contains sample load vs COD measurements taken from valid K_{Ic} tests for the different rail types. This Appendix also contains the CT formulas for K_1 and crack opening displacement d_1. The formulas for K_1 and d_1 are given as a polynomial function of the crack length a and applied load P. Thus, the crack length a and the stress intensity factor K_1 can be determined indirectly from the measured values of P and d_1 during a test.

Figure 55 – Compact tension fracture toughness test showing COD clip gauge.

3.6.2 Fracture Toughness Results

The photograph in Figure 56 shows typical fracture surfaces from sample CT specimens taken from the five different rail types. In each of the samples, the lower surface represents the region of the pre-cut notch; in this photo a wire EDM notch was cut for the AHH, HH, SS specimens, and waterjet notch cut for the CF&I77 and HAY84 specimens. The portion of the "smooth" fracture surface immediately ahead of the notch region represents the extent of the fatigue precrack as seen from the side view in Fig. 53. As part of the ASTM K_{Ic} measurement standards, it is required that the fatigue crack front obtained during precracking be straight within specified limits. In Fig. 56, the final, rough portion of the fracture surface beyond the precrack, represents the zone of rapid crack advance, which occurs during the K_{Ic} test.

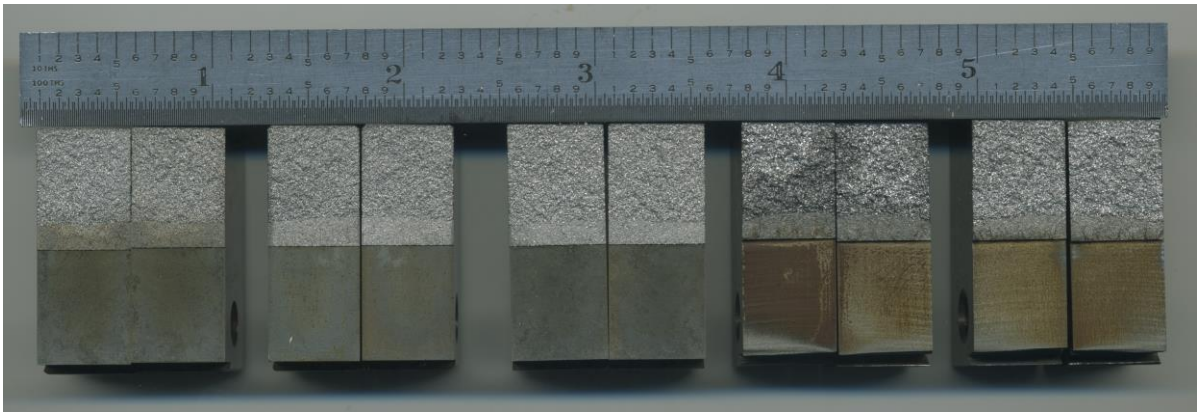

Figure 56 – Fracture surfaces after fracture toughness testing. From left to right: AHH, HH, SS, CF&I77, and HAY84.

Results from the fracture toughness measurements are given in Figs. 57 – 60. In these figures, the fracture toughness values, K_{Ic}, are given in $\mathrm{MPa}\sqrt{\mathrm{m}}$ at designated locations in the rail head. The miniature images indicate the location where specimens where cut from the rail. Red shading indicates K_{Ic} tests and blue indicates fatigue specimens. The grey miniature images represent specimens that were cut as backup for future testing, or specimens that that were tested, but did not fully comply with ASTM requirements for a valid K_{Ic} measurement (see further explanation in Appendix C). The location of the plate centers (as measured from the rail head running surface) where the CT specimens were taken, are: Slice 1 (6.5 mm), Slice 2 (19.5 mm), and Slice 3 (32 mm). Thus, as shown in Fig. 57, the fracture toughness for Slice 1, from the AHH rail, at an approximate depth of 6.5 mm from the rail head running surface, was measured to be $K_{Ic} = 40\,\mathrm{MPa}\sqrt{\mathrm{m}}$. For the CT specimens from the same rail, but at the 19.5 mm depth level (Slice 2), K_{IC} was determined be slightly less, i.e., between $K_{Ic} = 34\,\mathrm{MPa}\sqrt{\mathrm{m}}$ and $K_{Ic} = 36\,\mathrm{MPa}\sqrt{\mathrm{m}}$. At a depth of 32 mm from the rail head running surface, the measured K_{IC} in the rail was $K_{Ic} = 38.8\,\mathrm{MPa}\sqrt{\mathrm{m}}$. As can be seen in Fig. 57, the maximum value of K_{IC} is close to the rail head running surface. However, the vertical variation in fracture toughness seems to be relatively small. Likewise, there does not appear to be any significant variation in the fracture toughness across the width of the rail head as shown in the 2nd slice in Fig. 57.

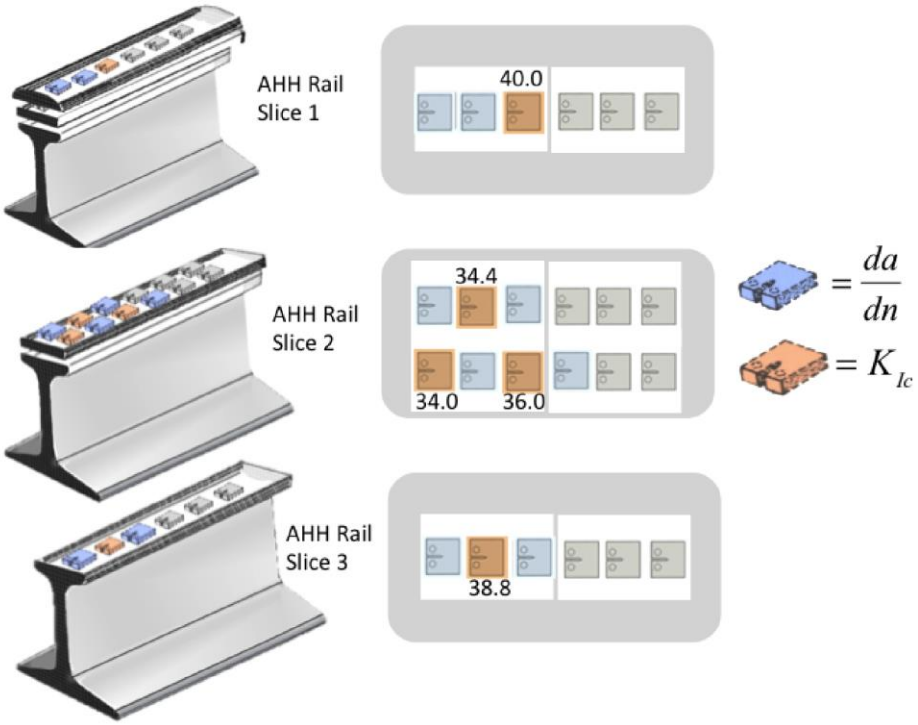

Figure 57 – Schematic showing location of CT specimens cut from three different levels in AHH rail head. Fracture toughness values given in terms of $\mathrm{MPa}\sqrt{\mathrm{m}}$. Red designates K_{Ic} test specimens and Blue designates fatigue crack growth specimens.

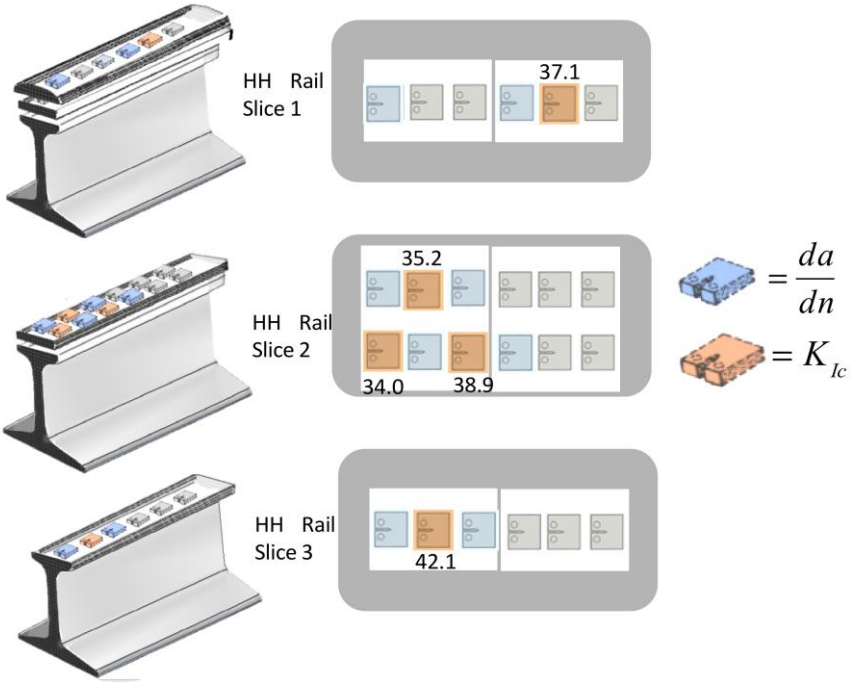

Figure 58 – Schematic showing location of CT specimens cut from three different levels in HH rail head. Fracture toughness values given in terms of $\mathrm{MPa}\sqrt{\mathrm{m}}$. Red designates K_{Ic} test specimens and Blue designates fatigue crack growth specimens.

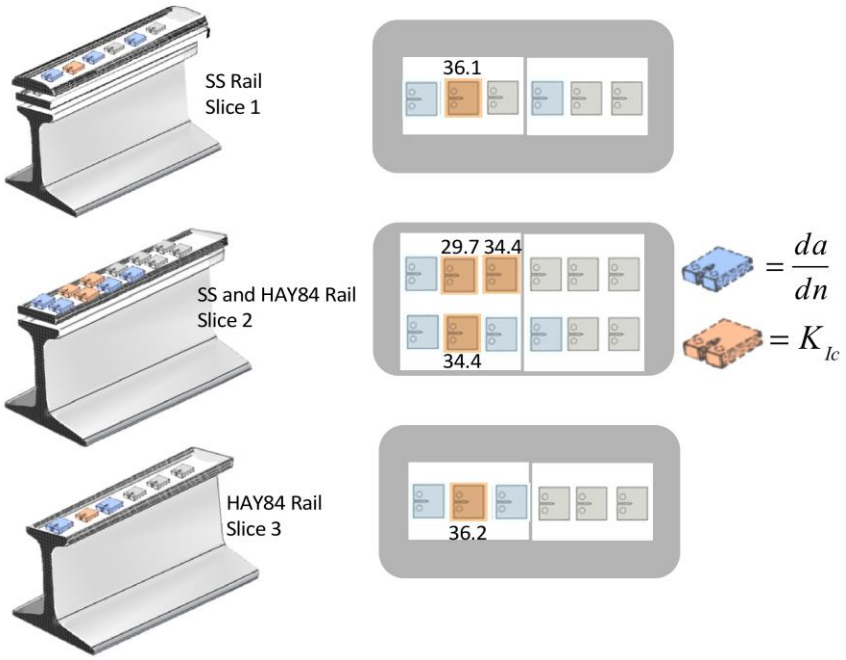

Figure 59 – Schematic showing location of CT specimens cut from three different levels in SS and HAY84 rail heads. Fracture toughness values given in terms of $\mathrm{MPa}\sqrt{\mathrm{m}}$. Red designates K_{Ic} test specimens and Blue designates fatigue crack growth specimens.

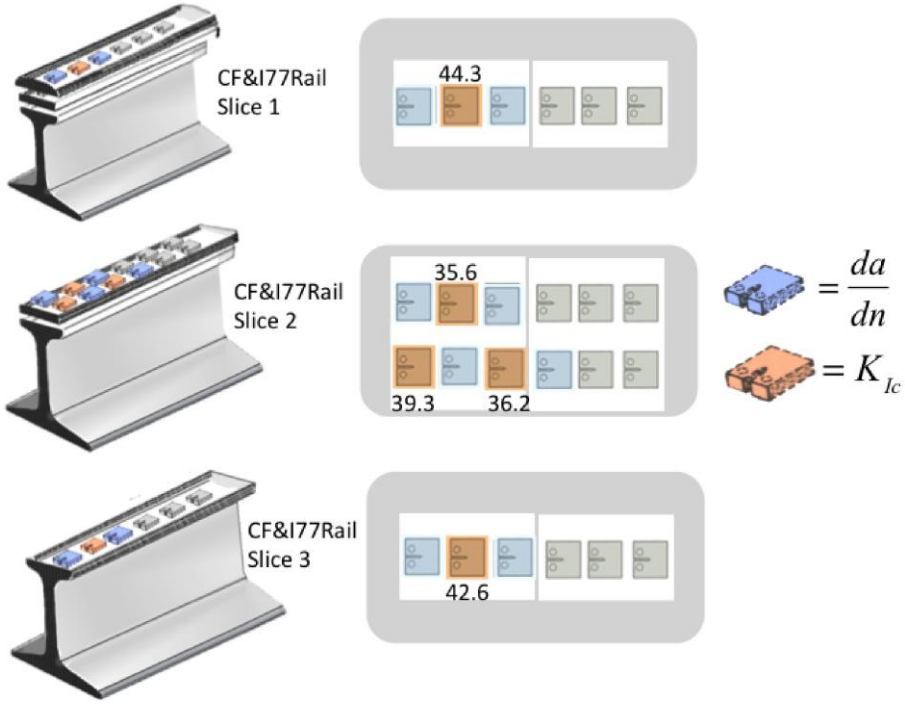

Figure 60 – Schematic showing location of CT specimens cut from three different levels in CF&I77 rail head. Fracture toughness values given in terms of $\mathrm{MPa}\sqrt{\mathrm{m}}$. Red designates K_{Ic} test specimens and Blue designates fatigue crack growth specimens.

It is quite possible, as one looks at thinner and thinner layers within the rail heads, that there may be a greater vertical variation in the fracture toughness. However, to achieve a finer fracture toughness spatial resolution would require much thinner specimens, specimens that would violate the ASTM small scale yielding requirement. If such measurements were desired, it would be more appropriate to use J_{Ic} testing procedures.

Small variations in fracture toughness values were determined from all of the rail heads, as shown in Figs. 57 – 60. In the early phase of the testing program, it was recognized that the SS and HAY84 rails would have very similar fracture toughness values. Thus, the fracture toughness results from these two rails are combined in a single figure, Fig. 59.

Taking into account all of the fracture toughness measurements obtained from the horizontally cut plates in the rail heads, average fracture toughnesses for the different rails can be taken as: AHH = 36.6 $\mathrm{MPa}\sqrt{\mathrm{m}}$, HH = 37.5 $\mathrm{MPa}\sqrt{\mathrm{m}}$, SS & HAY84 = 34.2 $\mathrm{MPa}\sqrt{\mathrm{m}}$, and CF&I77 = 39.6 $\mathrm{MPa}\sqrt{\mathrm{m}}$. Thus, it can be concluded that there is a negligible difference in the average fracture toughness for the different rails. Table 11 summarizes the variation in the average fracture toughness in each rail type as a function of depth (measured from the rail head running surface) to the center of the test specimen.

Table 11 – Fracture Toughness K_{Ic} ($\mathrm{MPa}\sqrt{\mathrm{m}}$) as a function of depth measured from the rail head running surface.

Depth in mm	AHH	HH	SS & HAY84	CF&I77
6.5	40.0	37.1	36.1	44.3
19.5	34.7	36.0	32.8	37.0
32.0	38.8	42.1	36.2	42.6

3.7 Fatigue testing

Equation Section (Next)

The same type of Compact Tension (CT) specimens that were used for fracture toughness testing, were also used for the majority of the fatigue measurements, e.g., Fig. 49. The specimens were precracked as shown in Fig. 53 and continuous fatigue crack growth measurements were made on CT specimens subjected to varying amplitude sinusoidal loading at a frequency of 20 Hz. The fatigue crack growth rate $\left(da/dn\right)$ for each specimen was monitored as a function of the change in the stress intensity factor (ΔK), where $\Delta K = K_{max} - K_{min}$. The magnitude of the R-ratio $\left(R = K_{\min}/K_{\max}\right)$, in the majority of the tests, was maintained at $R = 0.1$. As noted in Section 2.6, it was anticipated that the relatively small dimensions of the CT specimen would minimize any residual stress effect on the fatigue crack growth rate measurements. Thus, it is expected that the da/dn measurements from the CT specimens are primarily a function of the local metallurgical properties and orientation. During measurement of the crack growth rates, the measured value of the load amplitude P and the clip gauge measurement of the crack opening displacement (COD), or d_1, provides sufficient information for computing the crack length a and the instantaneous value of K_1, based on the compliance formula for the CT specimen (see Appendix C). Using feedback control, crack growth rate tests were conducted under controlled ΔK conditions, i.e., under decreasing, or increasing ΔK.

3.7.1 Fatigue crack growth rate results

Fatigue crack growth rate measurements were performed on compact tension specimens cut from two different orientations in the rail heads. The first orientation, the orientation used for most of the fatigue testing, relied on CT specimens cut from horizontal plates taken at three different levels within the rail head as depicted in Figures 61 - 64. These locations were identical to the locations used for the fracture toughness measurements described in Section 2.6. The crack propagation direction for these specimens was therefore along the major axis of the rail, a direction with very uniform material properties. The second orientation utilized CT specimens cut from vertical plates taken from either side of the plane of symmetry in the rail head as shown in Figure 65. The CT specimens cut from these vertical plates permitted the measurement of fatigue crack growth behavior in two different crack propagation directions. As shown in Fig. 65, cracks from the vertically oriented CT specimens were designed to measure crack propagation behavior either vertically downwards (away from the rail running surface) or vertically upwards (towards the rail running surface).

During the fatigue crack growth rate measurements, load and COD were continuously measured to determine the change in the crack length (Δa) over a specified number of cycles (Δn), as a function of ΔK. In the majority of the fatigue crack growth rate tests, the fatigue measurements were started at a moderate ΔK value, e.g., 16 $\mathrm{MPa}\sqrt{\mathrm{m}}$. As the crack grew under fatigue conditions, ΔK was decreased, resulting in decreasing crack growth rates. Though no attempt was made to precisely ascertain values for ΔK threshold (ΔK_T), it can be seen from the da/dn data plots that as the crack growth rate approaches ~ 2×10^{-6} mm/cyc, it can be inferred that ΔK_T must be close to ~8 $\mathrm{MPa}\sqrt{\mathrm{m}}$ for the tests conducted with an R-ratio, R=0.1. Once crack growth rates were established at low values of ΔK, the value of ΔK was slowly increased during fatigue testing until the specimen failed. As expected, at high ΔK values the crack growth rates became quite large ($> 2 \times 10^{-3}$ mm/cyc), as K_{max} approached K_{Ic}.

Figure 61 shows the locations for the horizontal CT specimens taken from the AHH rail head. For example, specimen AHH-1B is the designation given to a fatigue specimen cut from the 1st plate, as measured from the rail head running surface. The center planes of the horizontal specimens are at 6.5 mm (level 1), 19.5 mm (level 2), and 32.0 mm (level 3).

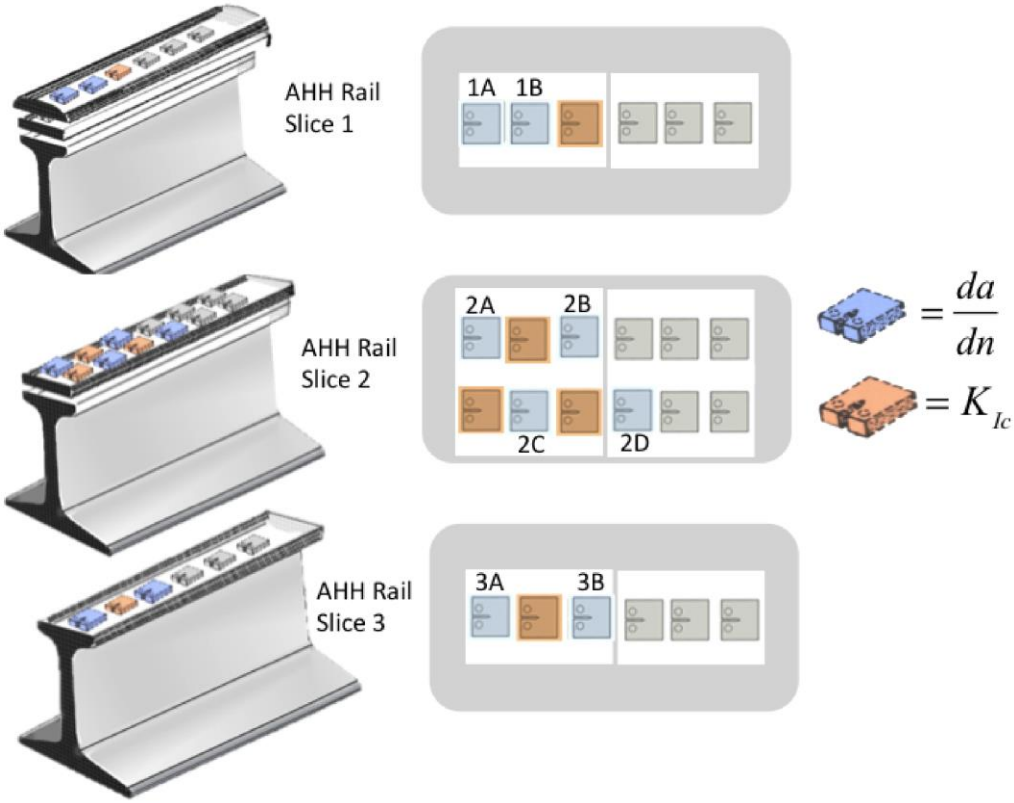

Figure 61 – Designations for fatigue specimens taken from different levels in AHH rail.

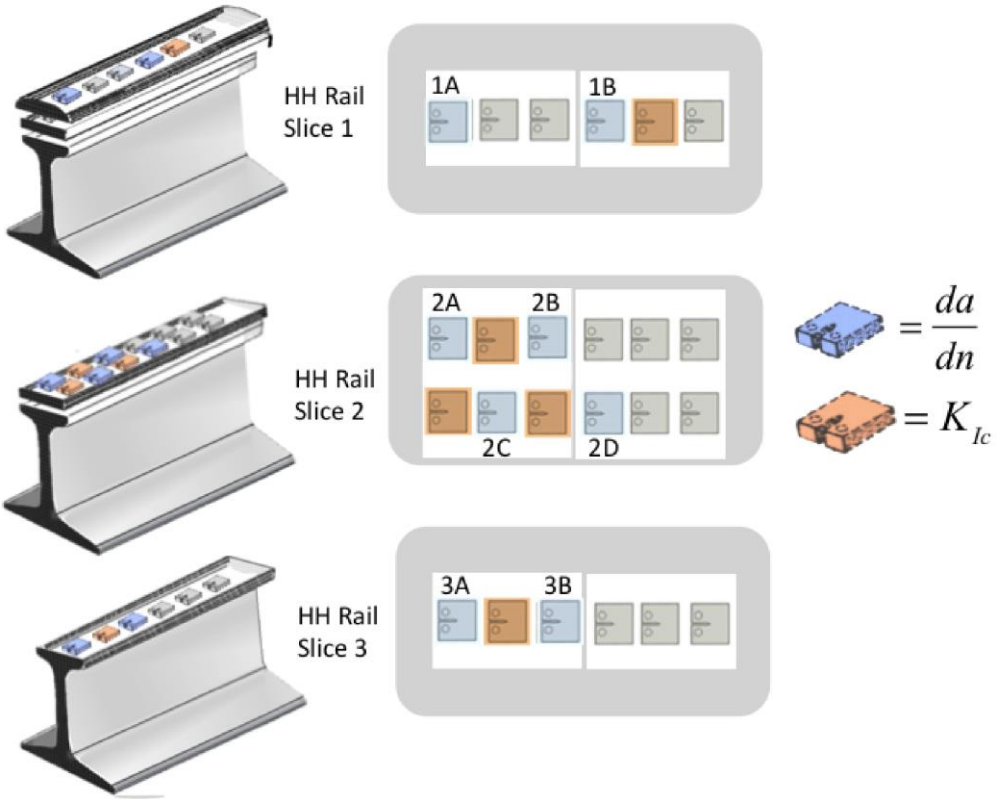

Figure 62 – Designations for fatigue specimens taken from different levels in HH rail.

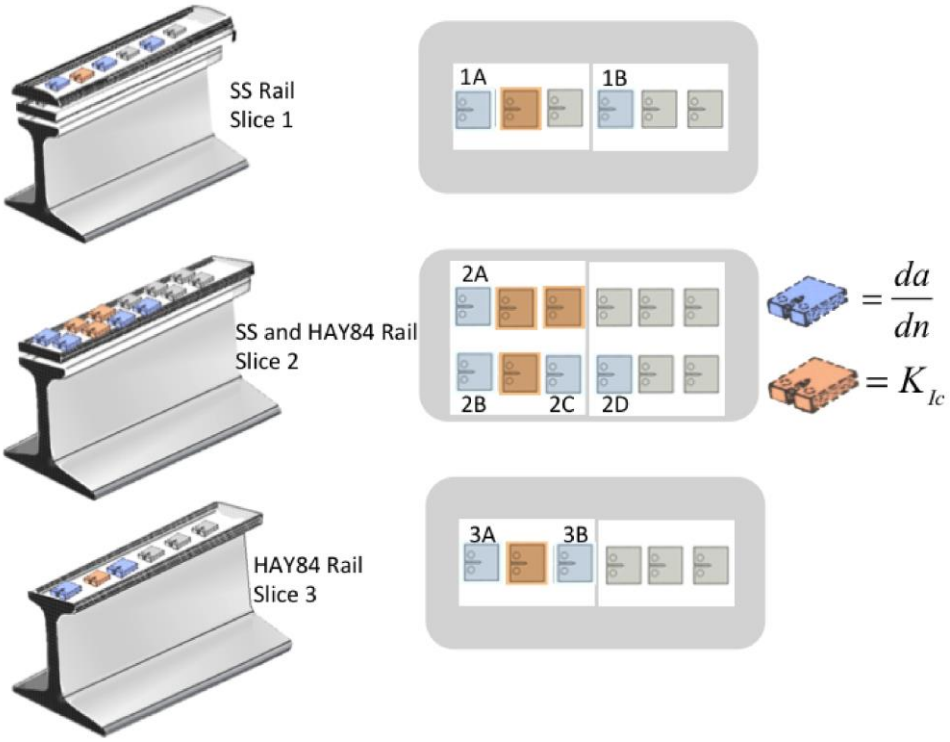

Figure 63 – Designations for fatigue specimens taken from different levels in SS and HAY84 rails.

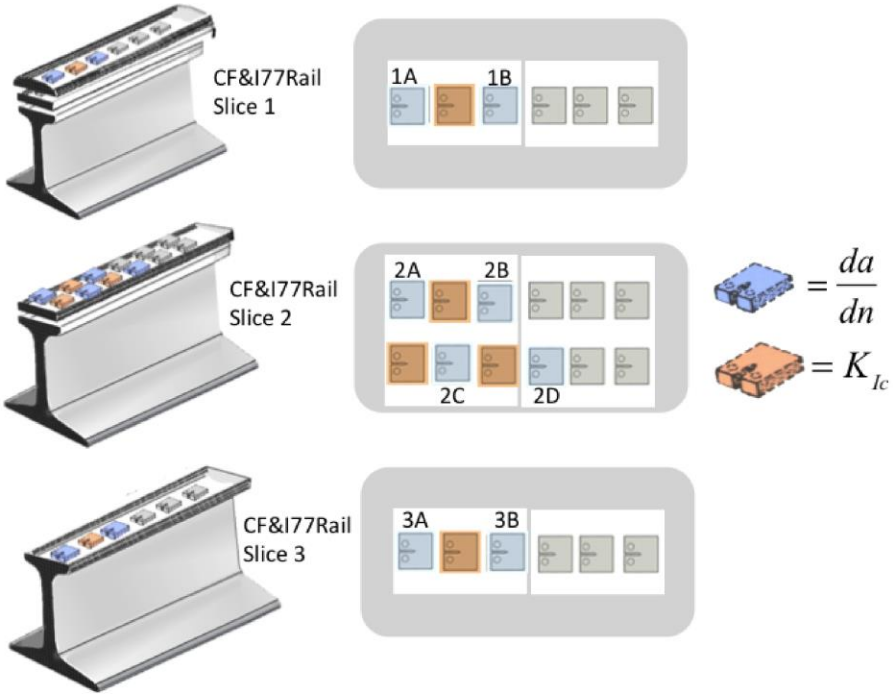

Figure 64 – Designations for fatigue specimens taken from different levels in CF&I77 rail.

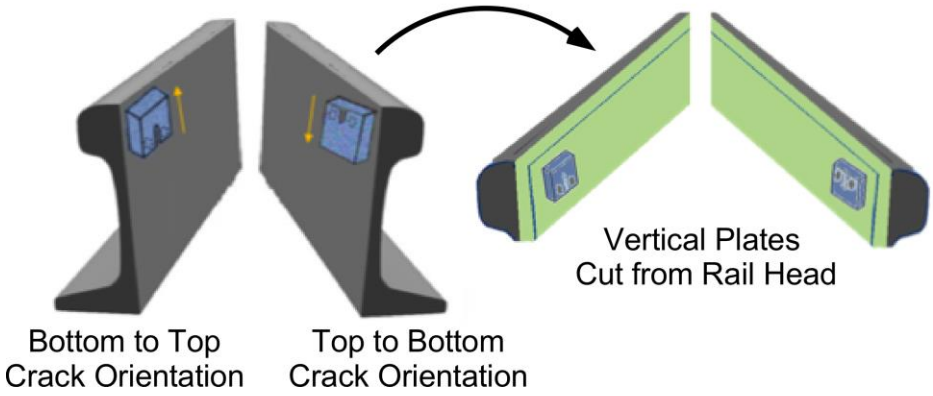

Figure 65 – Schematic showing orientation of CT specimens cut from vertical plates in rail head.

A typical plot from one of the crack growth rate fatigue tests is shown in Figure 66. In this figure a semi-log plot of the crack growth rate data (da/dn) is given as a function of ΔK, for specimen AHH-1B (see Fig. 61). This test was conducted at an R-ratio of $R = 0.1$, $\left(R = K_{\min}/K_{\max}\right)$. As can be seen from the plot, ΔK_T appears to be ~8 $\text{MPa}\sqrt{\text{m}}$. Very high crack growth rates, on the order of 2×10^{-3} mm/cyc, are recorded as ΔK approaches ~29 $\text{MPa}\sqrt{\text{m}}$. In this plot, three different nonlinear least-square curve fits were fit to the data:

Paris-Erdogan fit:
$$\frac{da}{dn} = C\left(\Delta K\right)^p \quad , \tag{2.7.1}$$

with, $C = 3.72 \times 10^{-10}$, $p = 4.18$.

Forman-Standard fit:
$$\frac{da}{dn} = C\frac{\left(\Delta K\right)^p}{K_c - \Delta K} \quad , \tag{2.7.2}$$

with, $C = 3.69 \times 10^{-7}$, $p = 2.52$, $K_c = 29.4$.

NASA NASGRO fit:
$$\frac{da}{dn} = C\left(\Delta K\right)^p \frac{\left(1 - \frac{\Delta K_{th}}{\Delta K}\right)^m}{\left(1 - \frac{\Delta K}{K_c}\right)^q} \quad , \tag{2.7.3}$$

with, $C = 1.37 \times 10^{-8}$, $p = 2.74$, $m = 0.278$, $q = 0.568$, $\Delta K_{th} = 8.5$, and $K_c = 29.5$.

As shown in Fig. 66, the Forman-Standard curve fit provides a good representation of the crack growth rates at high ΔK and the NASA-NASGRO fit provides a reasonable fit close to ΔK_T. Since the experimental effort in this study was focused on generating data in Region II, the broad midrange of crack growth rates where "power law" dependence prevails, the Paris-Erdogan crack growth rate fit was used to correlate the bulk of the fatigue data for this report.

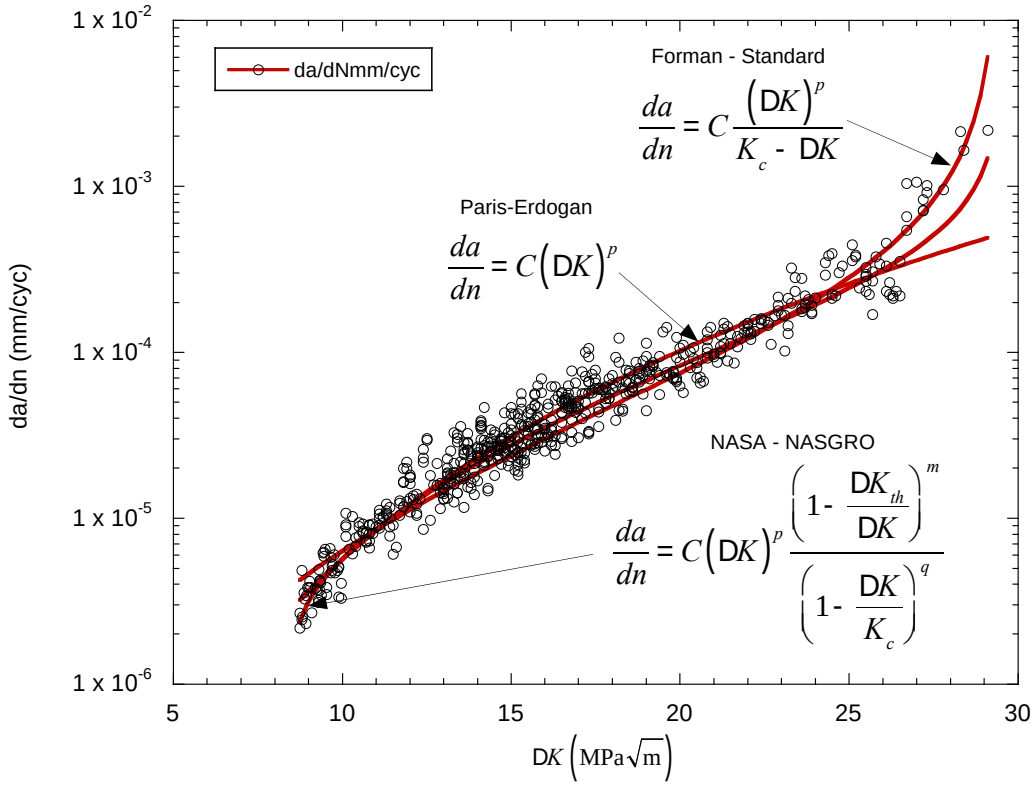

Figure 66 – Crack growth rate data from horizontal AHH rail specimen AHH-1B (R=0.1). Curve fit parameters *C*, *p*, *m* and *q* are given in (2.7.1) - (2.7.3).

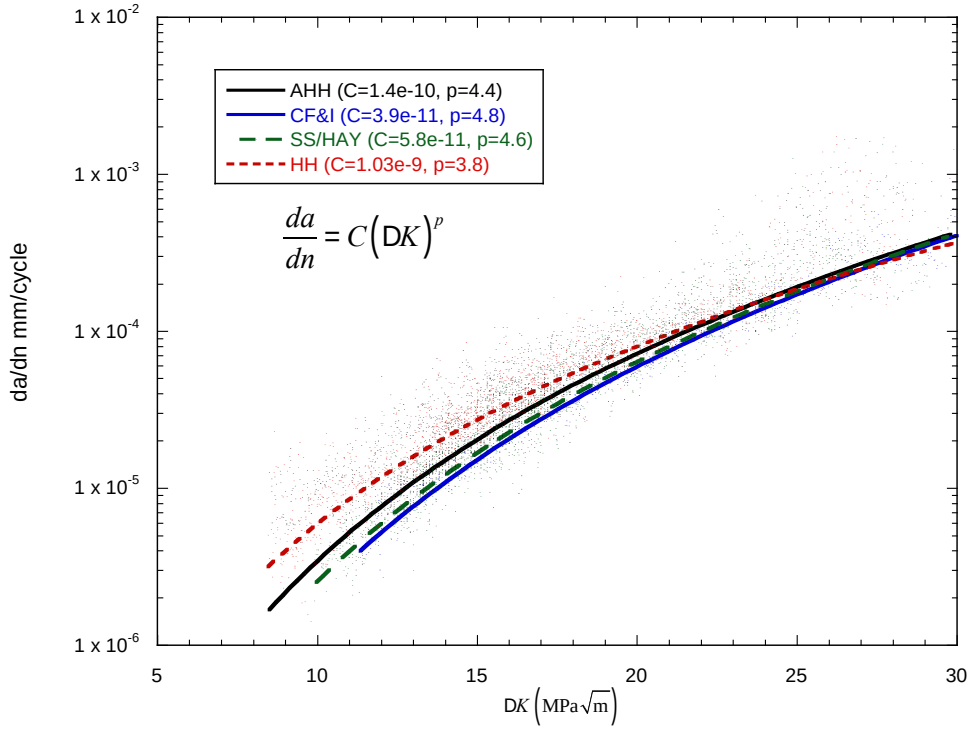

Figure 67 – Average fatigue crack growth rates for horizontal cracking in all rails (*R*=0.1). All curve fits based on data from seven test specimens per rail type.

Figure 67 contains a plot of the fatigue crack growth rate data obtained from the horizontal plates shown in Figs. 61 - 64, cut from the different rail types, and tested at the same R-ratio (R=0.1). Test results from seven CT specimens were used to obtain the curve fits for each of the rail types shown in Fig. 67. The purpose of this plot is to show the relative similarities in the fatigue crack growth rates in all of the rails for the horizontally oriented CT specimens. The main difference in fatigue crack growth rates for the different rails seems to occur at low ΔK values. However, it should be pointed out that at low crack growth rates, the relative error associated with determination of Δa also becomes greater, and this may exaggerate the differences between the crack growth rates at small da/dn. Overall, the fatigue crack growth rate behavior as a function of ΔK is very similar for the different rails.

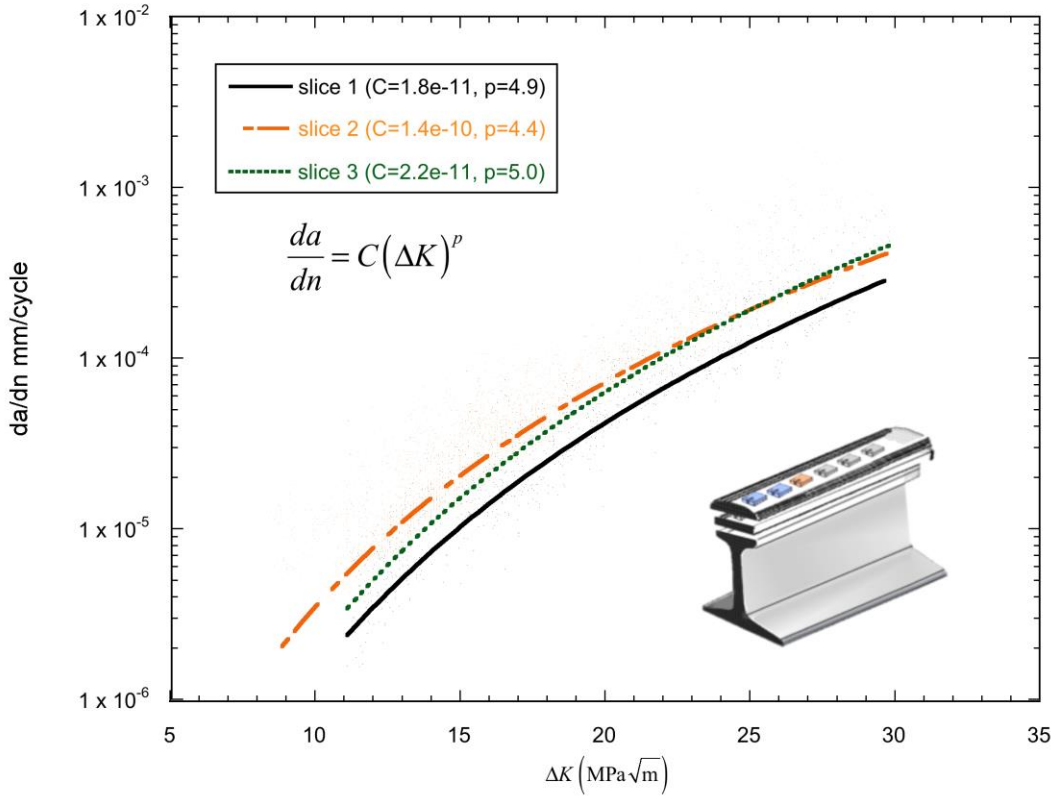

Figure 68 – Fatigue crack growth rate in AHH rail at different slice levels. Slice 1 is closest to rail running surface, Slice 3 furthest. *R*=0.1.

Figure 68 shows the variation in the fatigue crack growth rates at different slice levels within the AHH rail. The curve fit for Slice 1 was obtained using data from two CT specimens, Slice 2 from four specimens, and Slice 3 from one CT specimen. Though the differences in crack growth rates at the different depths in the rail head are not great, it does appear that the crack growth rates are lowest in the layer closest to the rail's running surface (~6.5 mm beneath the running surface). In addition to fatigue measurements on horizontally cut layers, fatigue specimens were also fabricated from vertically cut CT specimens (Fig. 65). Figure 69 compares the vertical fatigue crack growth behavior in the AHH rail with the horizontal fatigue behavior at various depths in the rail. In Figure 69 the dashed lines represent fatigue cracking measured in the specific horizontal planes depicted in the inset figure, while the solid red line represents the curve fit to the vertical crack growth behavior. The vertical crack growth rate data lies between the crack growth rates measured from the 1st and 3rd horizontal slice test specimens.

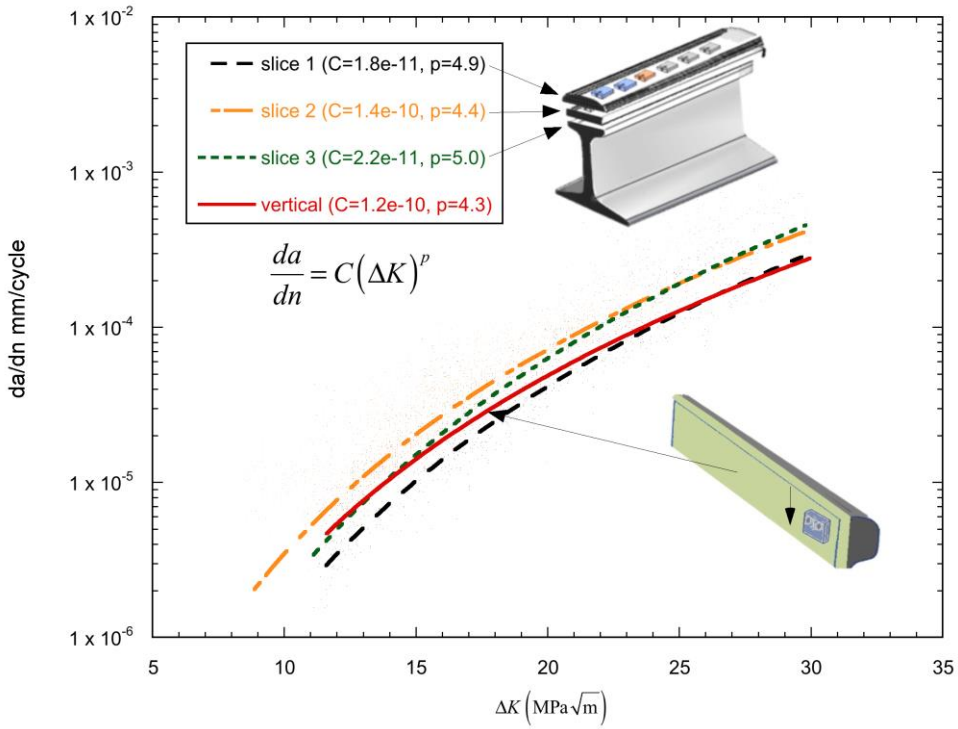

Figure 69 – Comparison of average fatigue crack growth rates for horizontal and vertical cracking in AHH rail. *R*=0.1.

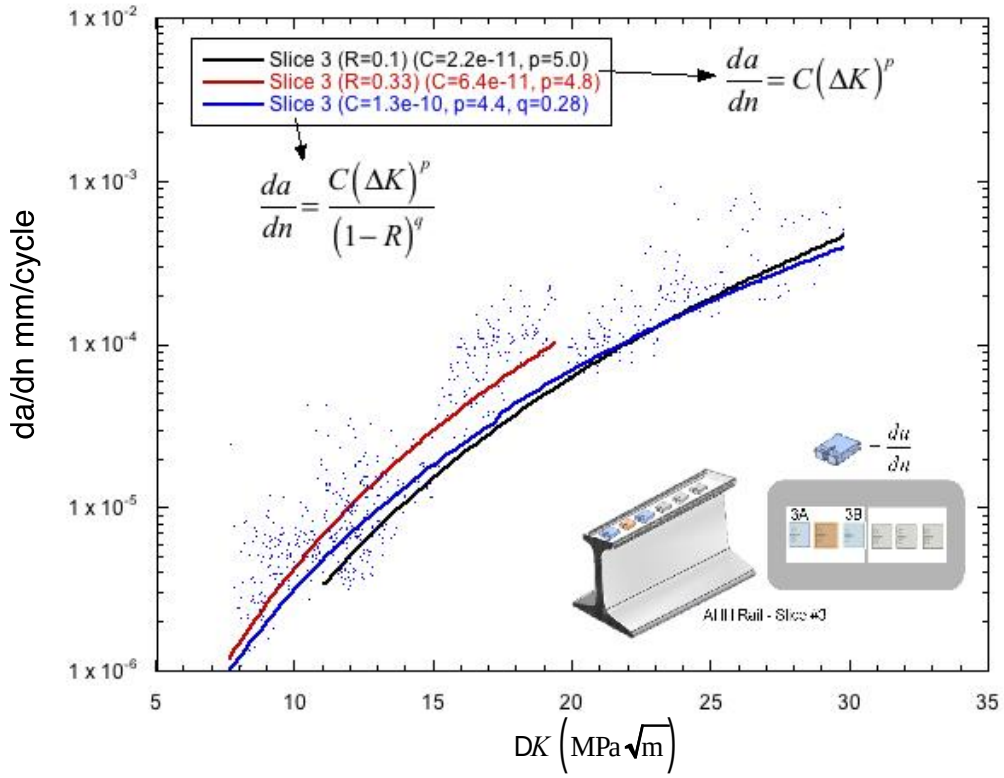

Figure 70 – Comparison of horizontal fatigue crack growth rates at two different R-ratios, R=0.1 and R=0.33, in Slice #3 of AHH rail.

Though it is well known that ΔK is the primary parameter that controls fatigue crack growth rates, it is also known that the R-ratio can exert an important secondary effect on fatigue crack growth. The R-ratio, defined as $R = K_{\min} / K_{\max}$, introduces a mean load on the test specimen, in addition to the amplitude of the sinusoidal loading. The R-ratio effect can be particularly important for rails subjected to high residual stresses and thus is an important factor that should be quantified for accurate predictions of fatigue reliability in head hardened rails.

Figure 70 provides a comparison of crack growth rates at two different R ratios, R = 0.1 (Black line) and R = 0.33 (Red line). The crack growth rates depicted in this figure are for specimens AHH-3A and AHH-3B, taken from the same slice level (Slice 3) in the AHH rail (see Fig. 61). These two fatigue specimens were located on either side of the AHH fracture toughness specimen that had $K_{Ic} = 38.8\ \text{MPa}\sqrt{\text{m}}$ (Fig. 57). Figure 70 exhibits classical R-ratio fatigue behavior, i.e., at the higher R-ratio there is an increased crack growth rate and lower ΔK_T values. Supplementing the Paris-Erdogan curve fit, an additional curve fit parameter, q, can be introduced to incorporate the stress ratio effect. One empirical form that is often used to include the R-ratio in the curve fit, is the so-called Walker equation given by

$$\frac{da}{dn} = \frac{C(\Delta K)^p}{(1-R)^q} \quad . \tag{2.7.4}$$

When curve fitting da/dn data over a broad range of *R*-ratio values, *R* can be treated as an additional independent variable, which allows the characterization of da/dn behavior as a function of both ΔK and *R*. As can be seen in Fig. 70, using the data from two sets of *R*-ratio tests, the 3 parameter least-squares fit results in an interpolated curve between the Paris-Erdogan curve fits obtained at the two different *R*-ratios. In this particular case, $C = 1.3 \times 10^{-10}$, $p = 4.4$, $q = 0.28$, for eqn. (2.7.4). However, in this study, da/dn testing was conducted only at two different *R*-ratios, *R* = 0.1 and *R* = 0.33. Thus, the benefit of considering *R* as a separate independent variable, for the purposes of curve fitting over such a limited range of *R*, is questionable. As can be seen in this figure, for the two different *R*-ratios, there is an overlap in the measured da/dn data only between ($11\ \text{MPa}\sqrt{\text{m}} < \Delta K < 20\ \text{MPa}\sqrt{\text{m}}$). Thus, for this particular Walker curve fit, the da/dn data at *R* = 0.33 dominates the curve fit for $\Delta K < 11\ \text{MPa}\sqrt{\text{m}}$, and for $\Delta K > 20\ \text{MPa}\sqrt{\text{m}}$ the *R* = 0.1 data dominates. A much more accurate representation of the fatigue data is to simply give the Paris-Erdogan curve fits for the specific values of *R* as shown by the black and red curves in Fig. 70. It should also be noted that for higher *R*-ratios, e.g., *R* > 0.5, K_{max} very quickly approaches critical K_c for small values of ΔK. Thus, the available ΔK range of data for a 3-parameter da/dn curve fit can be quite small at high *R*-ratios. This often leads to a situation where fitting the q term in the Walker eqn. (2.7.4) is essentially done by trial and error until a value is found that best consolidates the data along a single straight line on the log-log plot of da/dn.

The *R*-ratio results obtained from two adjacent vertical crack specimens is shown in Figure 71. The da/dn behavior for the vertical cracking appears to be very similar to the horizontal cracking shown in Fig. 70.

Figure 72 provides a comparison of the vertical fatigue crack growth behavior in the HH rail with the horizontal fatigue behavior at various depths in the same rail. The fatigue crack growth rates in the HH rail are very similar to the behavior in the AHH rail (Fig. 69). However, for the HH rail, the lowest horizontal crack growth rates were measured in Slice #3, the layer furthest away from the running surface. This is in contrast to what was observed in the AHH rail, where the lowest crack growth rates were measured in Slice #1. The higher crack growth rates in the HH rail for Slice #1 and Slice #2 were almost identical to each other. As was observed in the fatigue crack growth rate behavior for the AHH rail head, the vertical crack growth rates in the HH rail lie between the crack growth rates measured in the 1st and 3rd horizontal slice test specimens.

The fatigue crack growth rate measurements in the AHH and HH rails appear to be very similar. However, there are some subtle structural differences in the nature of the fatigue cracking. This is shown in Figure 73, which contains a side-by-side comparison of the fatigue/fracture surfaces for CT specimens AHH 2A (see Fig. 61) and HH 2A (see Fig. 62) respectively. These two specimens were cut from identical locations in the two different rails and tested under identical fatigue conditions (*R*=0.1). As can be seen in the photographs, the fatigue surfaces in the AHH rail are noticeably smoother than counterpart fatigue/fracture surfaces in the HH rail. This difference in fatigue fracture surface roughness was also noted in the fatigue tests conducted on the CCT test specimens.

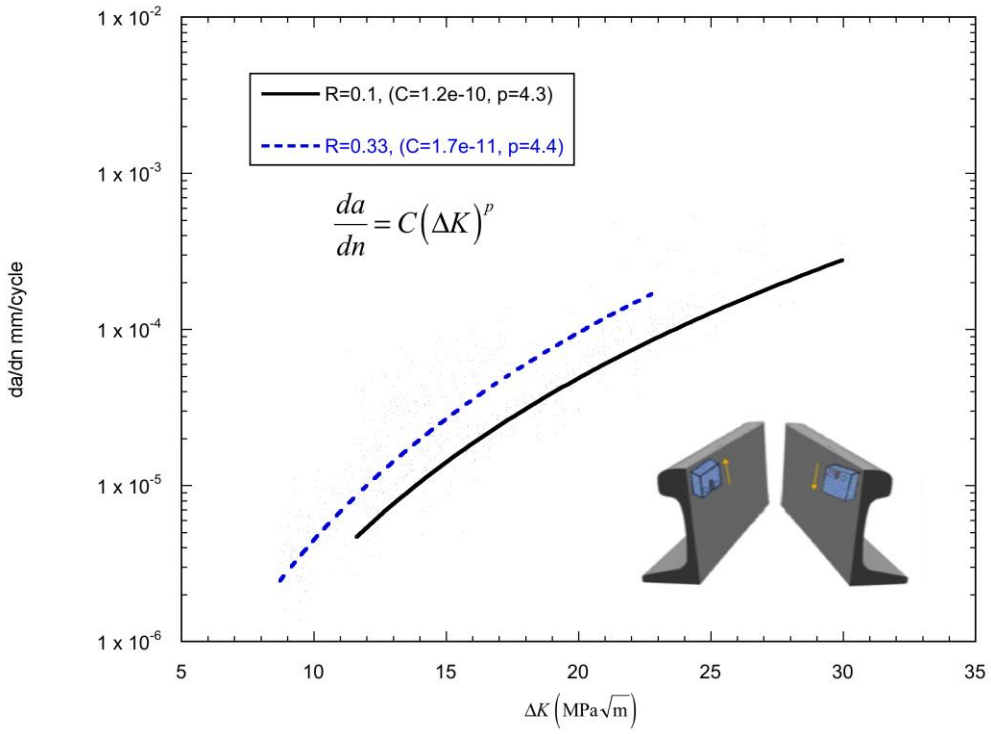

Figure 71 – Comparison of vertical fatigue crack growth rates in AHH rail for CT specimens at two different R ratios, *R*=0.1 and *R*=0.33.

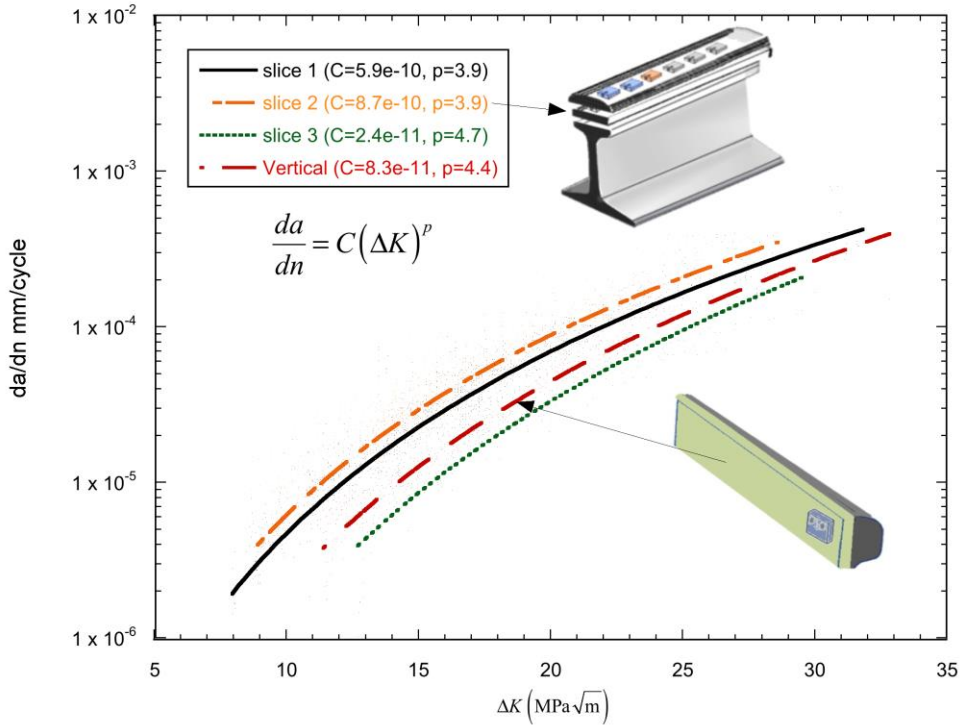

Figure 72 – Comparison of fatigue crack growth rates for horizontal and vertical cracking in HH rail. *R*=0.1. Slice 1 (2 tests), slice 2 (4 tests), slice 3 (1 test), vertical (1 test).

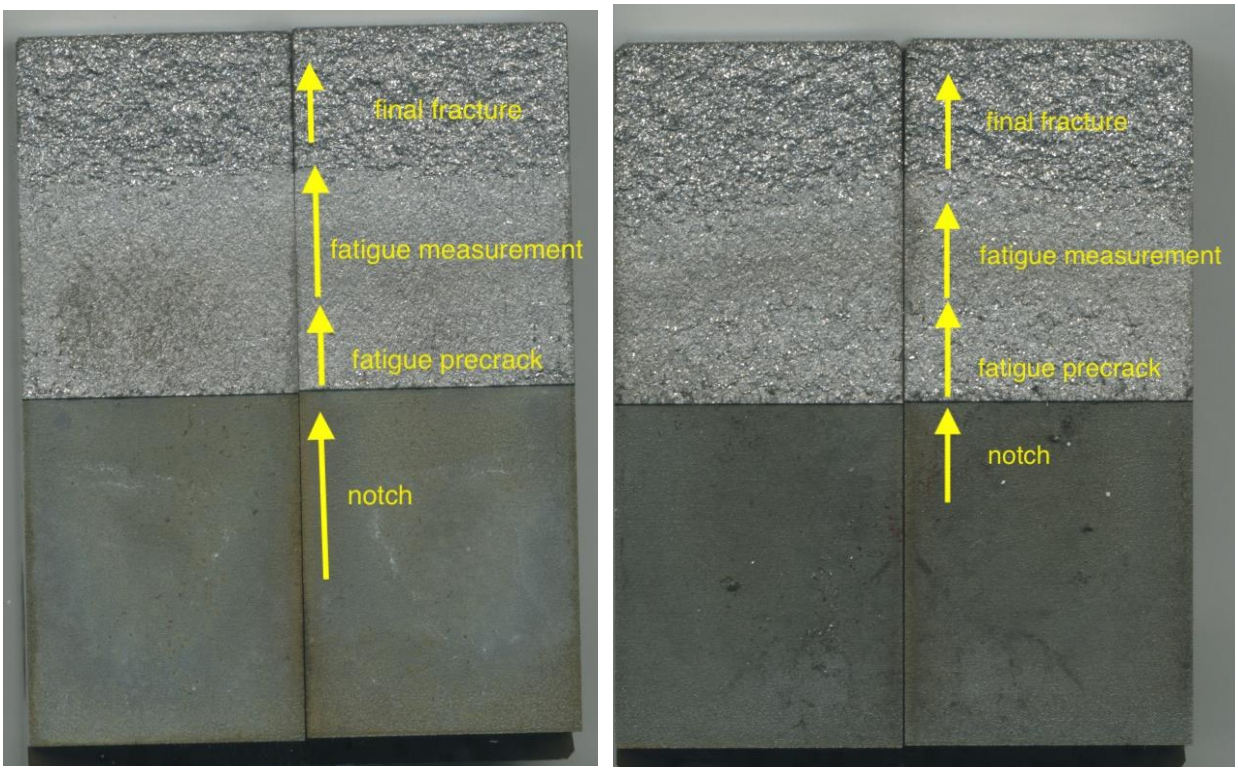

(a) (b)

Figure 73 – Fatigue/fracture surfaces: a) AHH Slice 2 (smooth fatigue crack surface), b) HH Slice 2 (rougher fatigue crack surface). *R*=0.1.

The fatigue curve fits for the HH rail at *R*-ratios 0.1 and 0.33 are given in Figures 74 and 77, for horizontal and vertical cracking, respectively. As was observed in the AHH rails, the fatigue cracking at different *R*-ratios in the HH rails represents classical *R*-ratio behavior with increasing *R*, i.e., increased crack growth rates, lower ΔK_T, and a decrease in the maximum value of ΔK before the onset of rapid (Region III) crack growth rates. Figures 75 and 76 contain photographs of the fatigue fracture surfaces for the HH horizontal fatigue test specimens taken from Slice 3, i.e., location HH 3B and HH 3A (Fig. 62), respectively. These two CT test specimens have very similar (rough) fatigue/fracture surfaces. Note that the discoloration on the crack surfaces was due to oxidation, which occurred a number of weeks after the original testing. Specimen HH 3B was tested at *R*=0.1 and HH 3A at *R*=0.33. Tests at these different *R*-ratios do not appear to have any significant effect on the relatively rough appearance of the fatigue surfaces. Referring to Figure 58, the fracture toughness at this location in the HH rail is also relatively high, measured to be $K_{Ic} = 42.1\,\mathrm{MPa}\sqrt{\mathrm{m}}$.

Figures 78 - 80 contain the fatigue crack growth results from the SS and HAY84 rails. The plots in Fig. 78 are average da/dn results from both rails. The results for vertical cracking in Fig. 80 are solely from the HAY84 rail. Figures 81 - 83 contain the fatigue crack growth rate measurements from the CF&I77 rail.

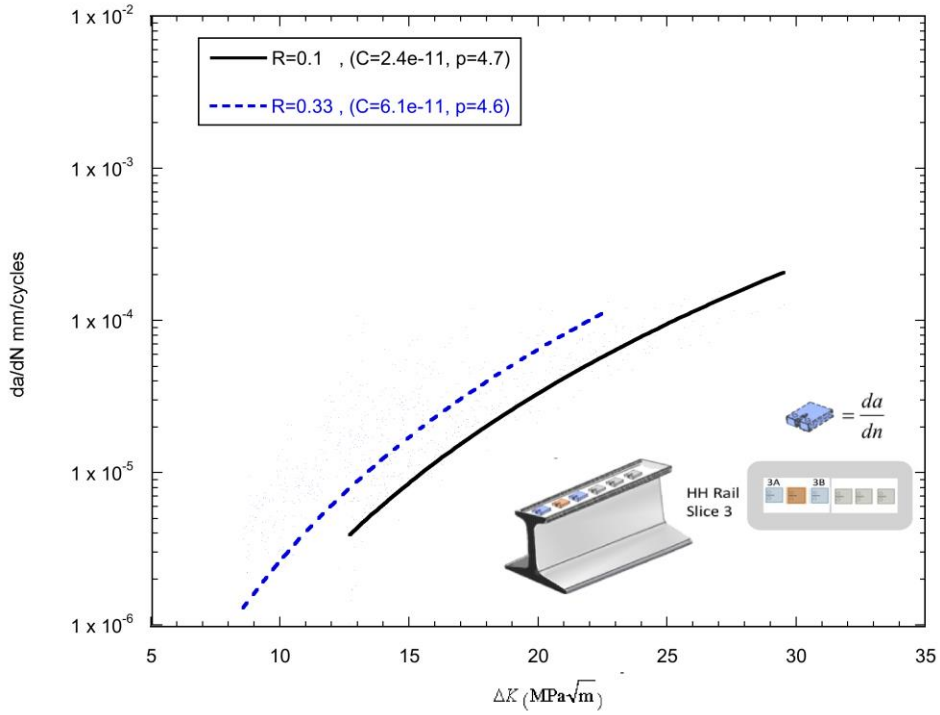

Figure 74 – Comparison of horizontal fatigue crack growth rates at two different R-ratios in Slice #3 of HH rail. *R*=0.1 and *R*=0.33.

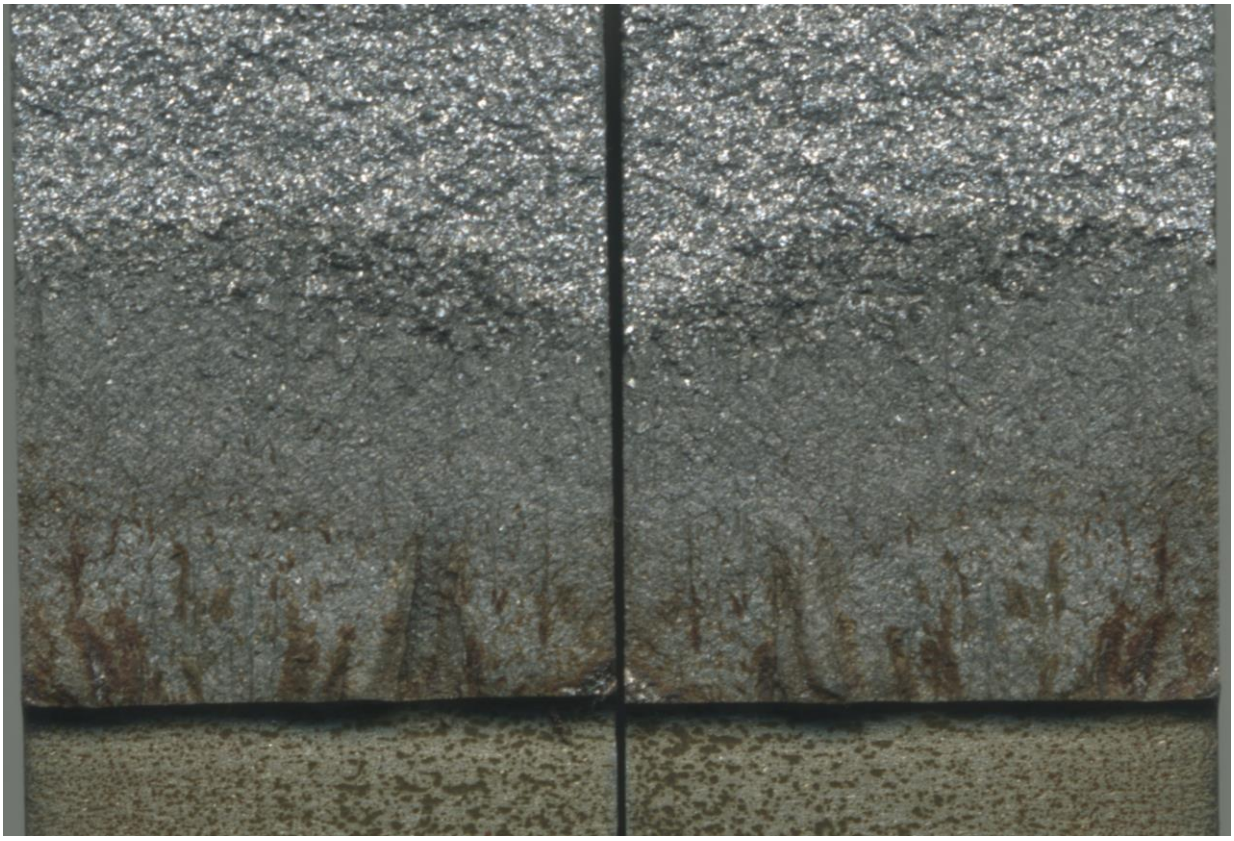

Figure 75 – Fatigue/fracture surface for HH 3B tested at *R*=0.1.

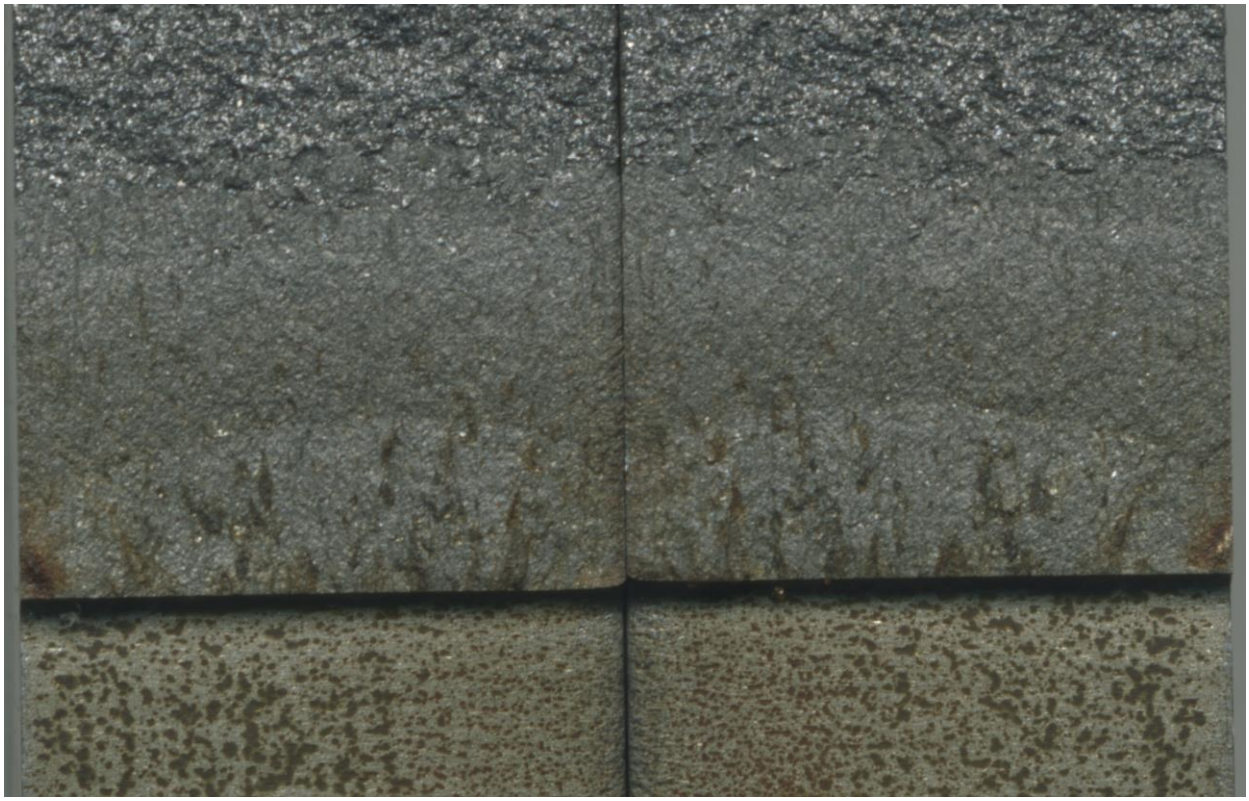

Figure 76 – Fatigue/fracture surface for HH 3A tested at R=0.33.

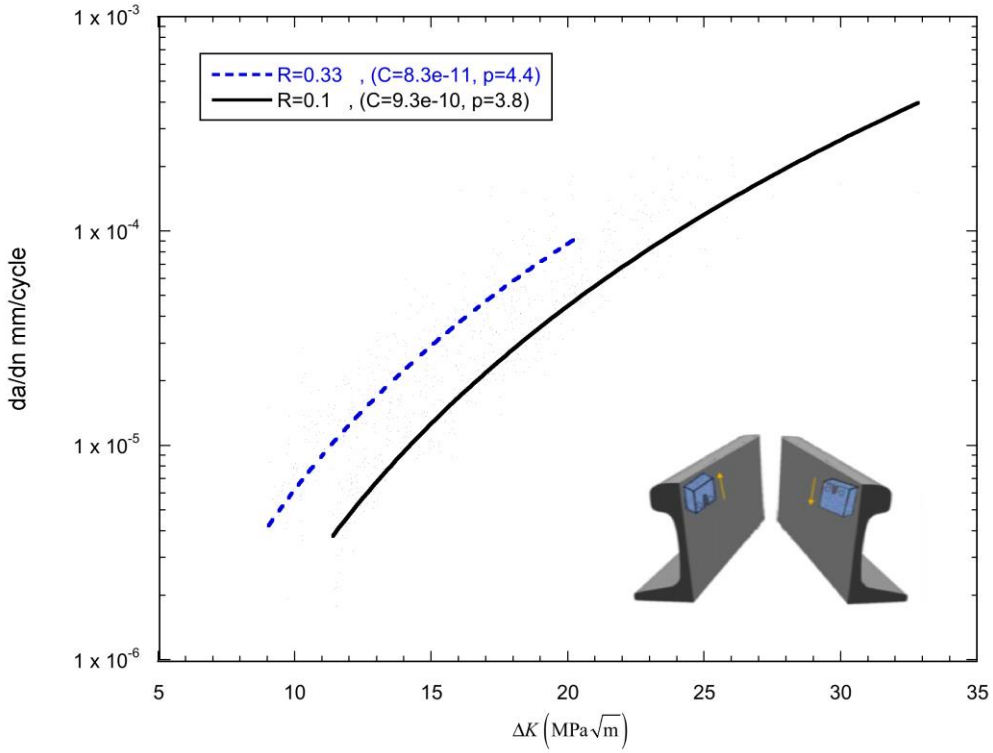

Figure 77 – Comparison of vertical fatigue crack growth rates in HH rail for CT specimens at two different R ratios. *R*=0.1 and *R*=0.33.

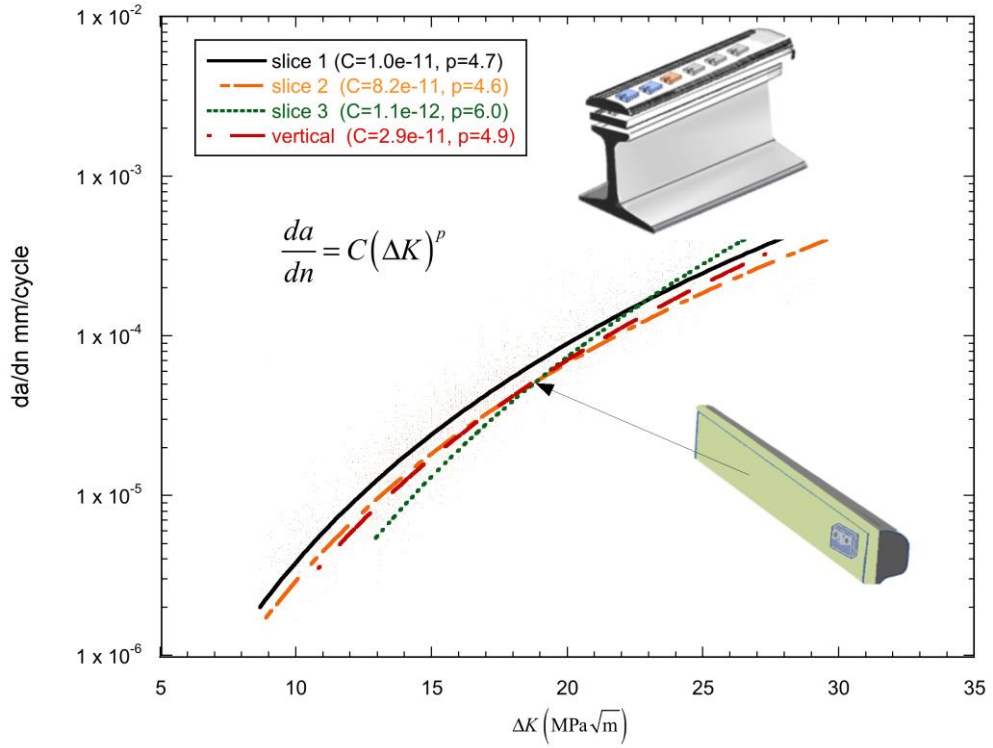

Figure 78 – Comparison of fatigue crack growth rates for horizontal and vertical cracking in the SS and HAY84 rails. *R*=0.1.

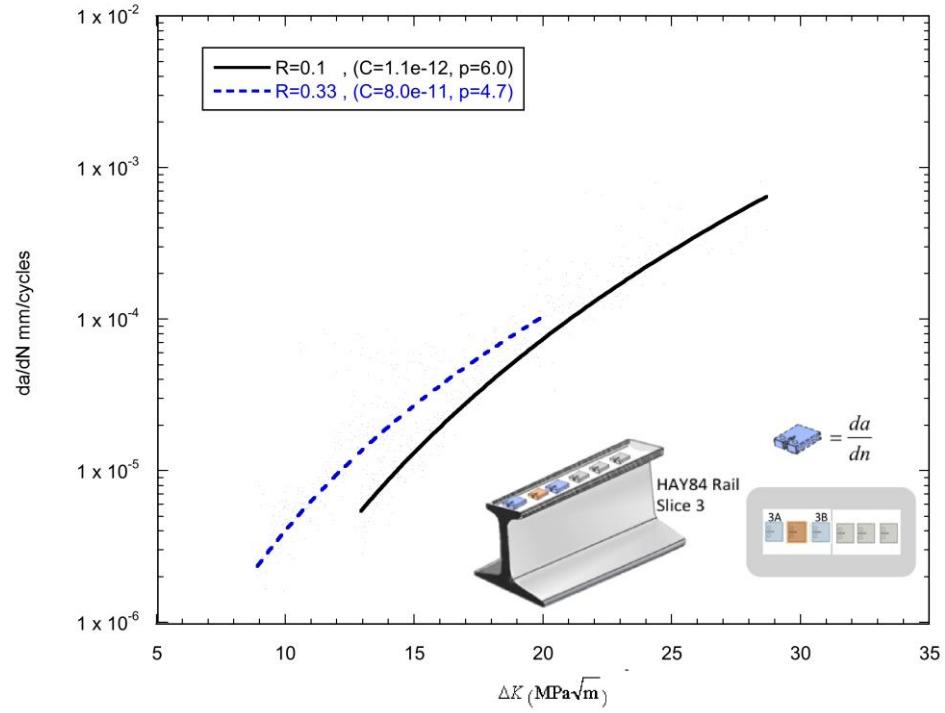

Figure 79 -– Comparison of horizontal fatigue crack growth rates at two different R-ratios in Slice #3 of HAY84 rail. *R*=0.1 and *R*=0.33.

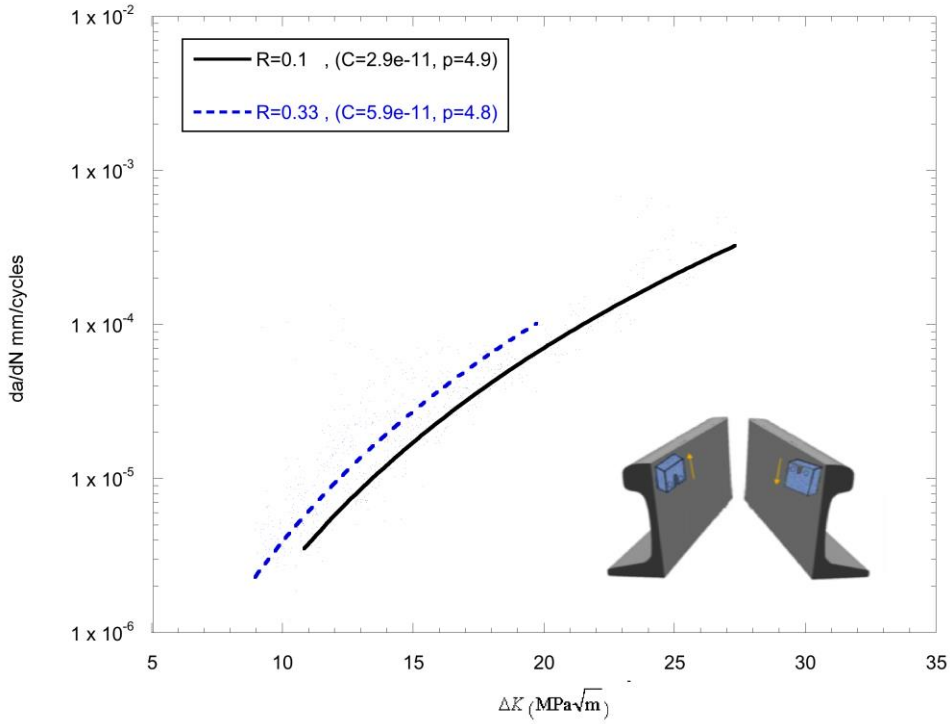

Figure 80 – Comparison of vertical fatigue crack growth rates in the HAY84 rail for CT specimens at two different R ratios. *R*=0.1 and *R*=0.33.

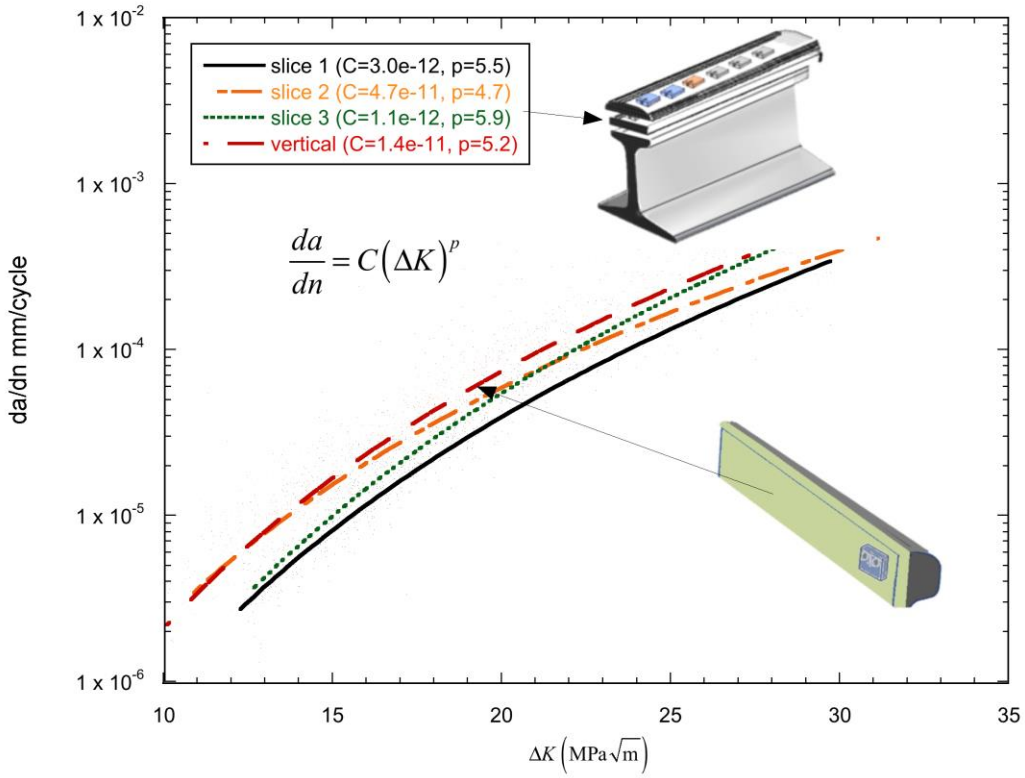

Figure 81 – Comparison of fatigue crack growth rates for horizontal and vertical cracking in the CF&I77 rail. *R*=0.1.

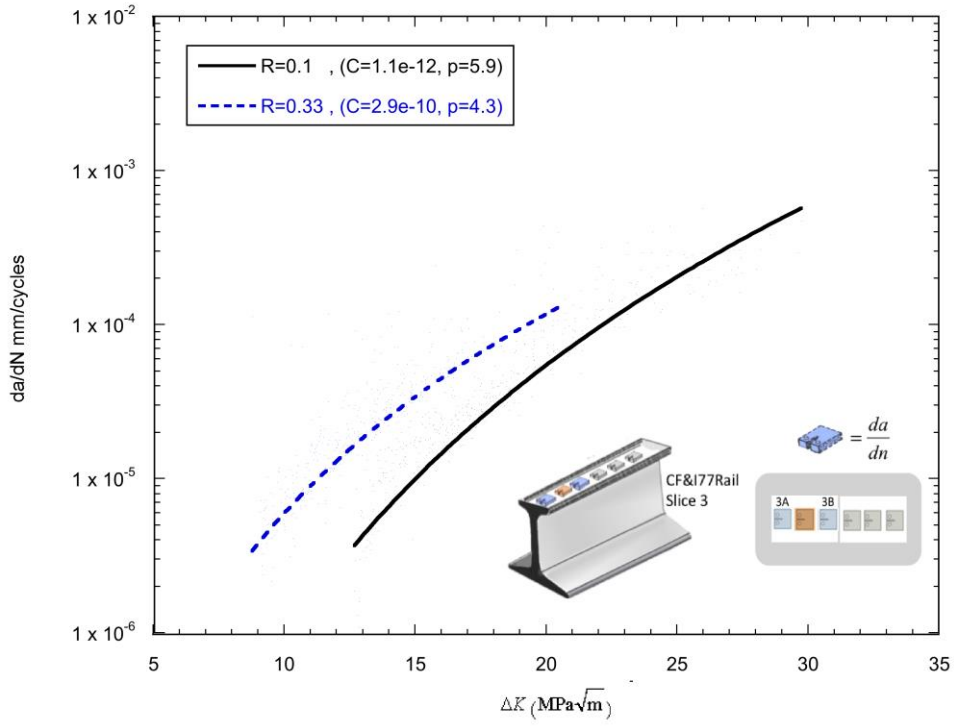

Figure 82 – Comparison of horizontal fatigue crack growth rates at two different R-ratios in Slice #3 of CF&I77 rail. *R*=0.1 and *R*=0.33.

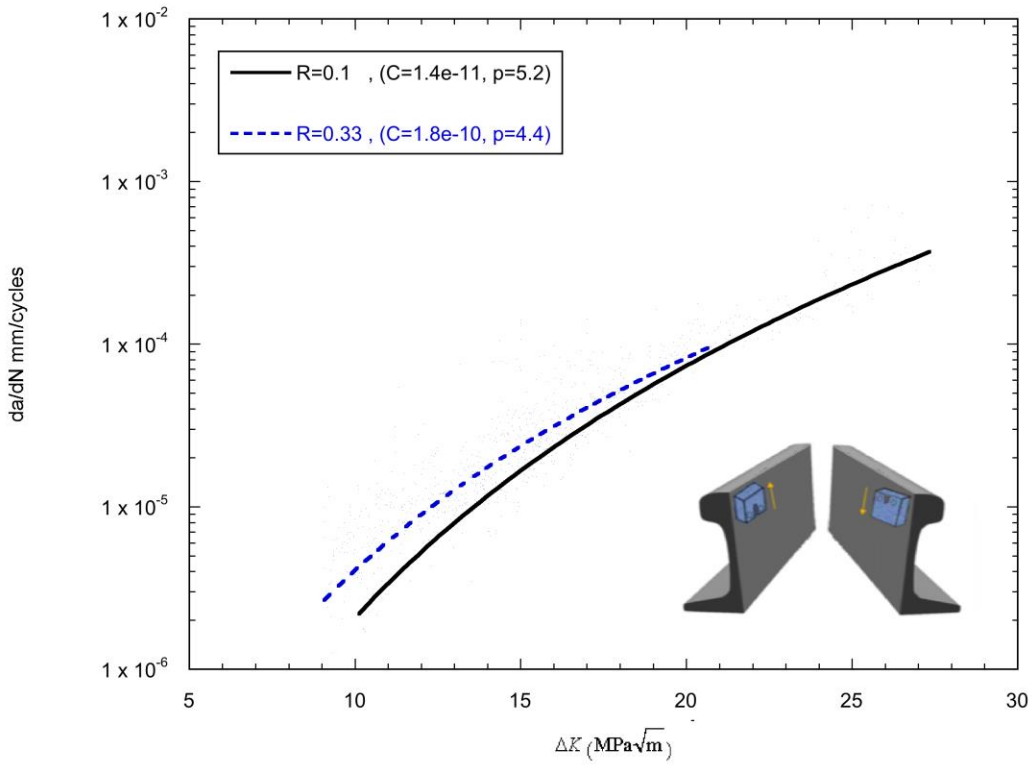

Figure 83 – Comparison of vertical fatigue crack growth rates in CF&I77 rail for CT specimens at two different R ratios. *R*=0.1 and *R*=0.33.

In addition to the Compact Tension (CT) test specimens, four large Center Cracked Tensile (CCT) specimens were also used to measure fatigue crack growth rates within the AHH and HH rail heads. The CCT specimens were cut from long plates taken from the widest portion of the rail heads as shown in Figure 84. As can be seen in this figure, the CCT specimen widths span the entire width of the rail head. The gray area in Figure 84 indicates the location of the notch/precrack. Figure 85 gives the dimensions of the CCT specimen prepared for the fatigue tests. The CCT specimens had a 0.010 in. width notch cut using wire edm prior to precracking and the specimens were loaded in uniaxial tension via pin loading as shown in Figure 86. The fatigue testing of the CCT specimens was conducted at Laboratory Testing Inc. (LTI) in Hatfield, PA, under the supervision of Dr. M. Adler.

The main purpose of conducting fatigue tests on the much larger CCT specimens is that, unlike the CT test specimens, there is a high likelihood the CCT specimens will have a significant residual stress component normal to the crack surface. If there is a significant variation in the residual stresses across the width of the rail head, then this should be continued over to the CCT plate cross-section, even though the material (and residual stresses) above and below the CCT plates have been removed due to cutting. The tensile residual stress component that exists in the axial direction in the interior of the rail head arises during the rail head hardening process. A sufficiently high tensile residual stress component normal to the crack surface in the CCT specimen will cause an increase in the fatigue crack growth rates compared with the residual stress free CT specimens.

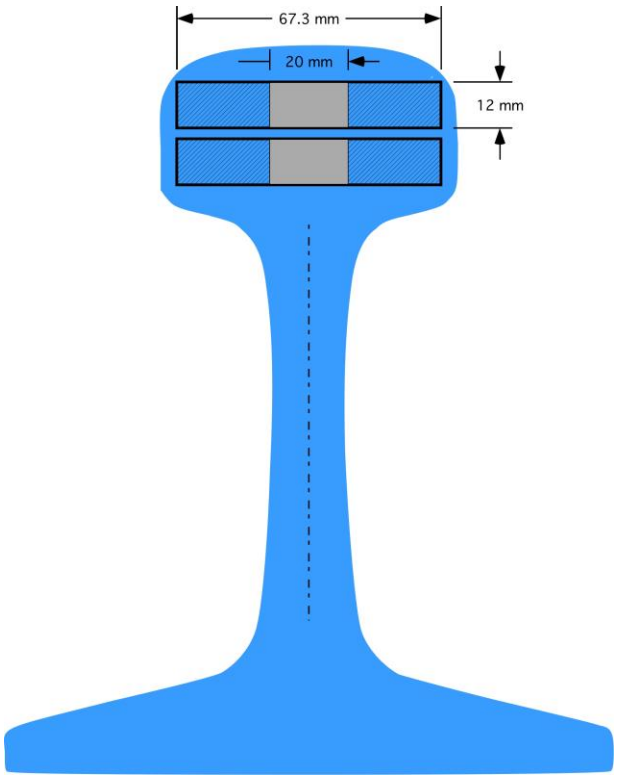

Figure 84 – Cross-section view of CCT fracture specimens cut from rail heads.

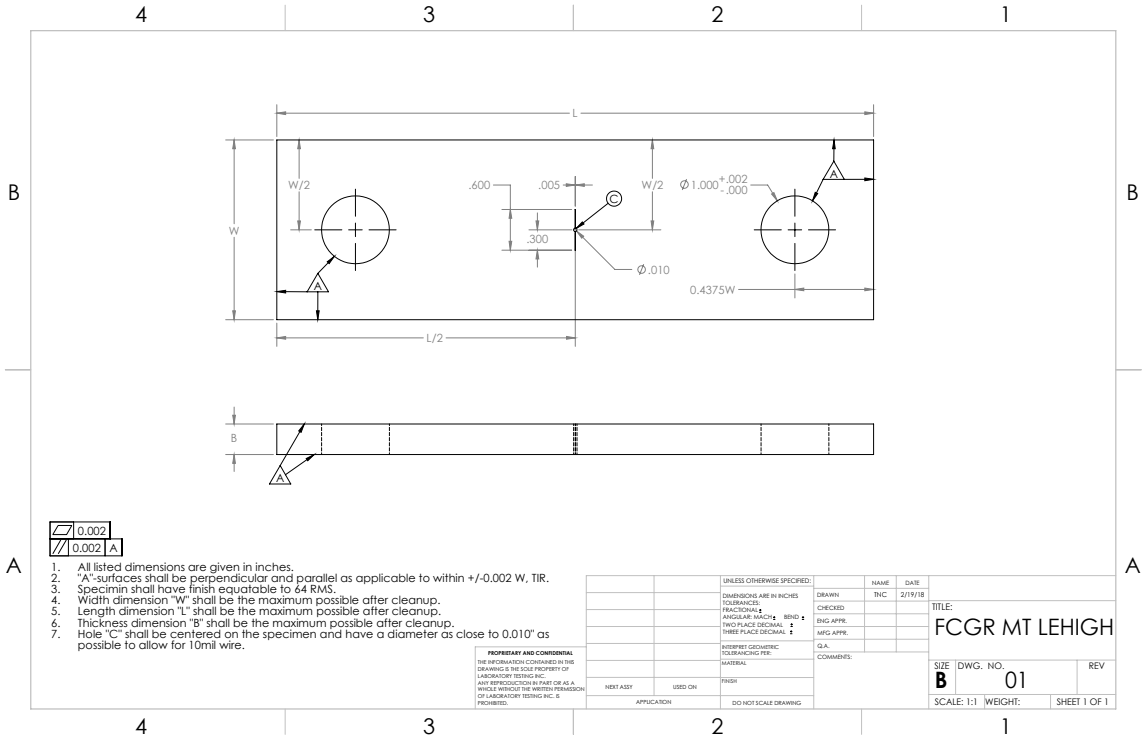

Figure 85 – Dimensions used for center cracked test specimen.

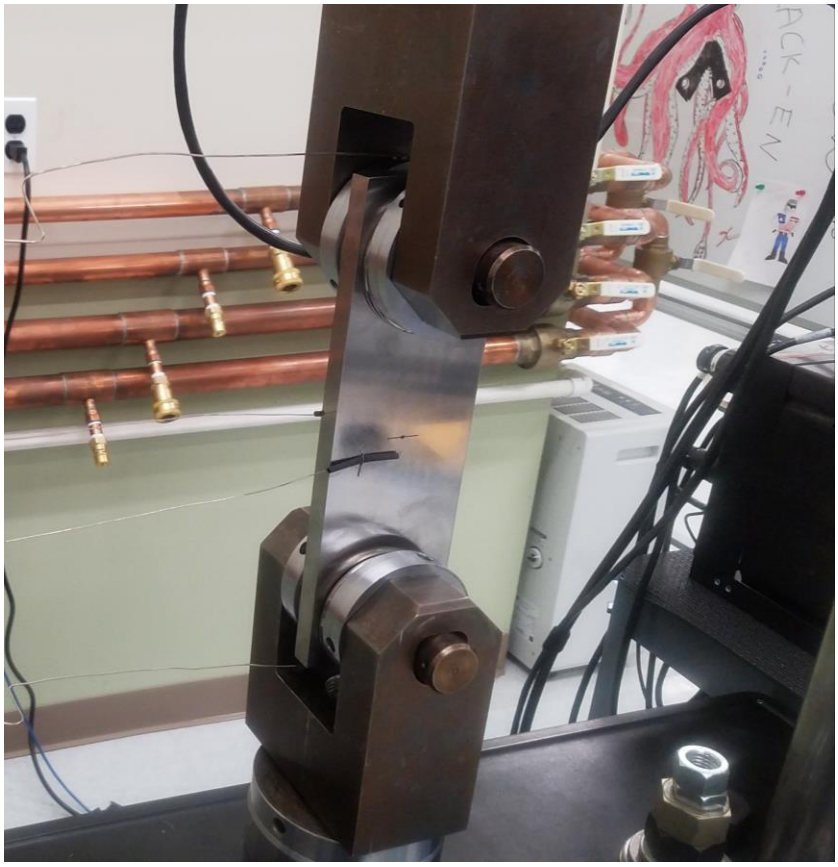

Figure 86 – Testing of center cracked tension (CCT) specimen at LTI.

The da/dn measurements at different *R*-ratios for the CT specimens can be considered to represent a baseline, i.e., residual stress free measurements. This cannot necessarily be assumed for the CCT specimens, due to their much larger size, where the specimen width spans the entire cross-sectional width of the hardened head. The apparent differences in crack growth rates from the two different specimen types for the HH rail can be seen in Figure 87. As shown in this figure, the crack growth rates obtained from the CCT tests were generally higher than the crack growth rates obtained from the CT specimens, tested at an *R*-ratio of *R*=0.1. In addition, the CCT testing seems to enter into the Region-III, i.e., high crack growth rate fatigue behavior, at ~ $\Delta K = 26$ $\mathrm{MPa}\sqrt{\mathrm{m}}$. This is indicative of a lower fracture toughness than would have been measured in an HH rail specimen with negligible residual stress, e.g., $K_{Ic} > 35$ $\mathrm{MPa}\sqrt{\mathrm{m}}$ (Table 11). It can be seen that a much better match with the CCT crack growth rates occurs when compared with the CT crack growth rates performed at *R*=0.33 (Figure 88).

Figure 89 shows the fatigue surface taken from the HH rail CCT specimen. This photograph is taken looking down on the left side of the central crack surface with the wire edm notch surface to the right and the rough fatigue crack surface on the left. The roughness of the fatigue surface is similar to the rough fatigue surfaces observed in the CT specimens (Figs. 75 and 76).

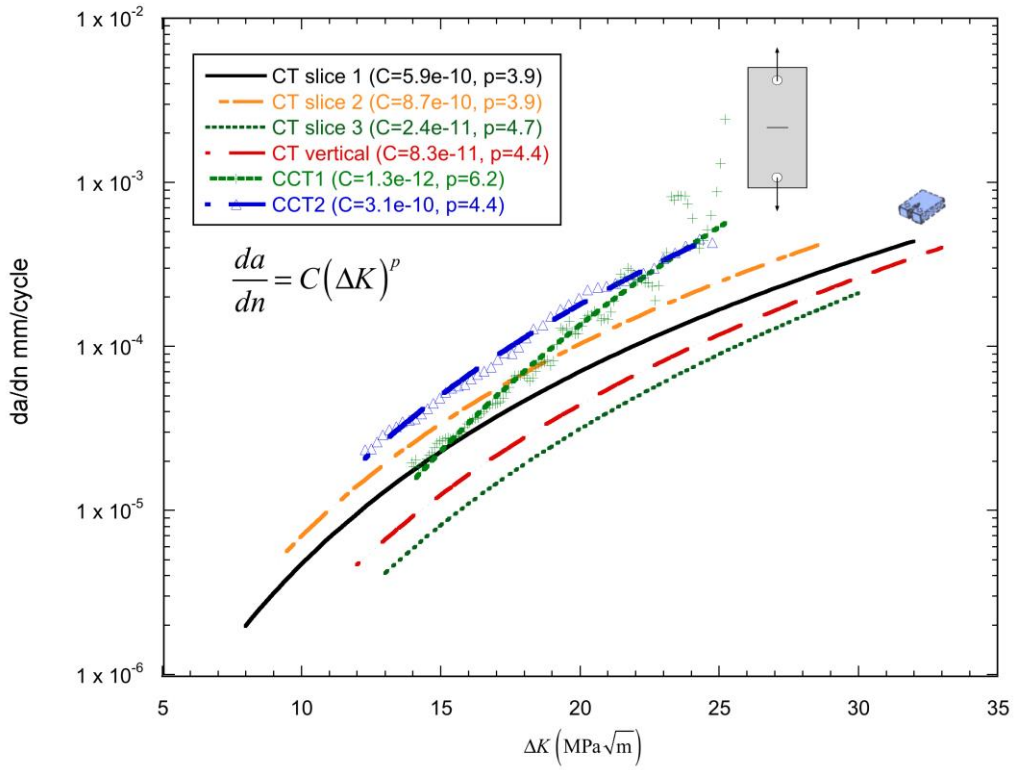

Figure 87 – Comparison of fatigue crack growth rates from CT and CCT specimens for HH rail. R=0.1.

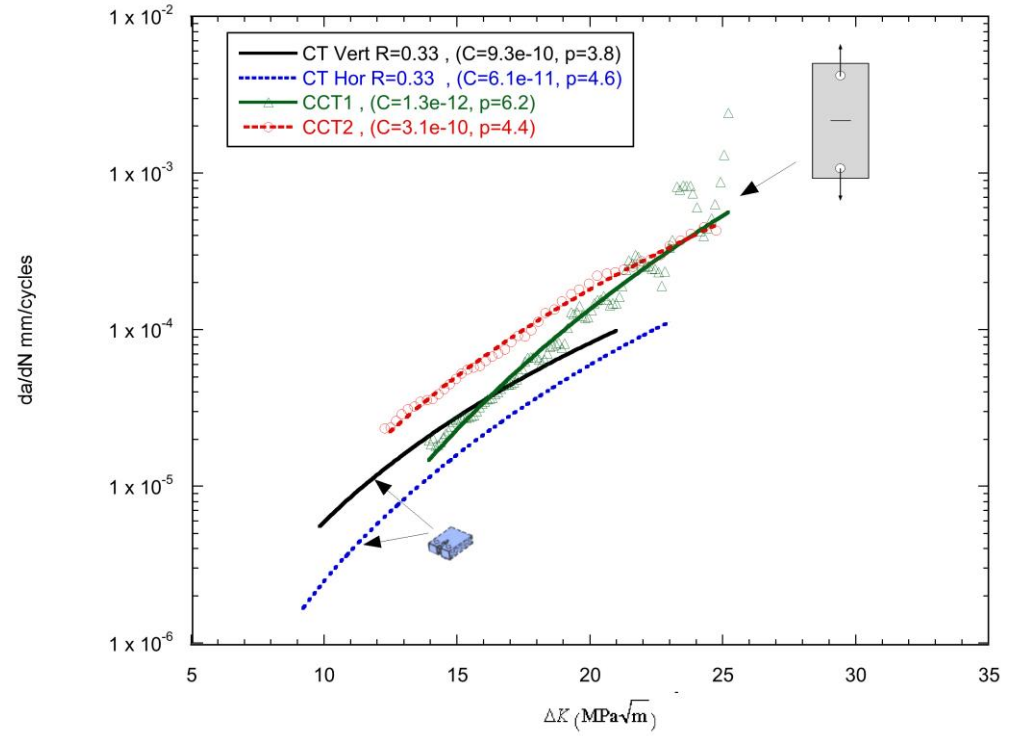

Figure 88 – Comparison of fatigue crack growth rates from horizontal and vertical CT specimens (R=0.33) with CCT specimens from the HH rail.

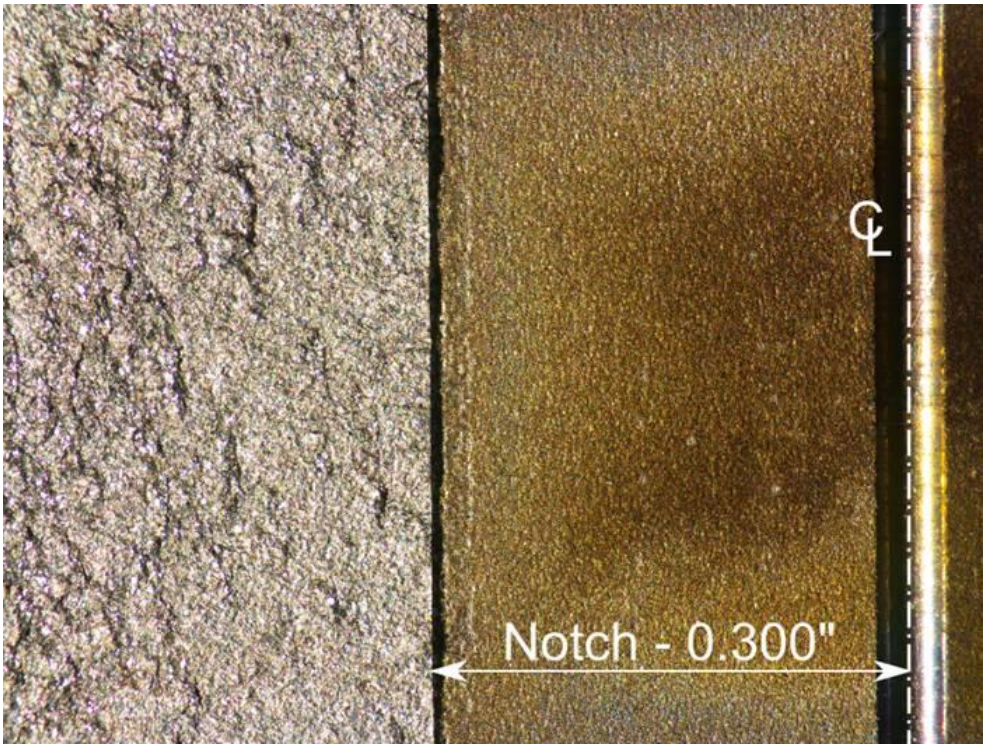

Figure 89 – Fatigue/fracture surface taken from HH rail CCT test specimen showing rough fatigue crack surface.

Figure 90 compares the crack growth rate from the AHH CCT specimen with the crack growth rates from the AHH CT specimens cut from different layers in the AHH rail. As can be seen, the crack growth rates in the CCT specimen is greater that the crack growth rates measured using CT specimens cut from any of the horizontal layers in the rail. It is again speculated that the higher crack growth rates for the AHH CCT specimen are due to higher residual stresses that may be present in the larger CCT test specimen. For example, Figure 91 compares the CCT crack growth rates for the AHH rail with crack growth rates obtained from CT specimens tested at R=0.33 (both vertical and horizontal specimens). The CCT test results seem to be consistent with crack growth rates from CT specimens measured at an elevated R-ratio, e.g. R>0.33.

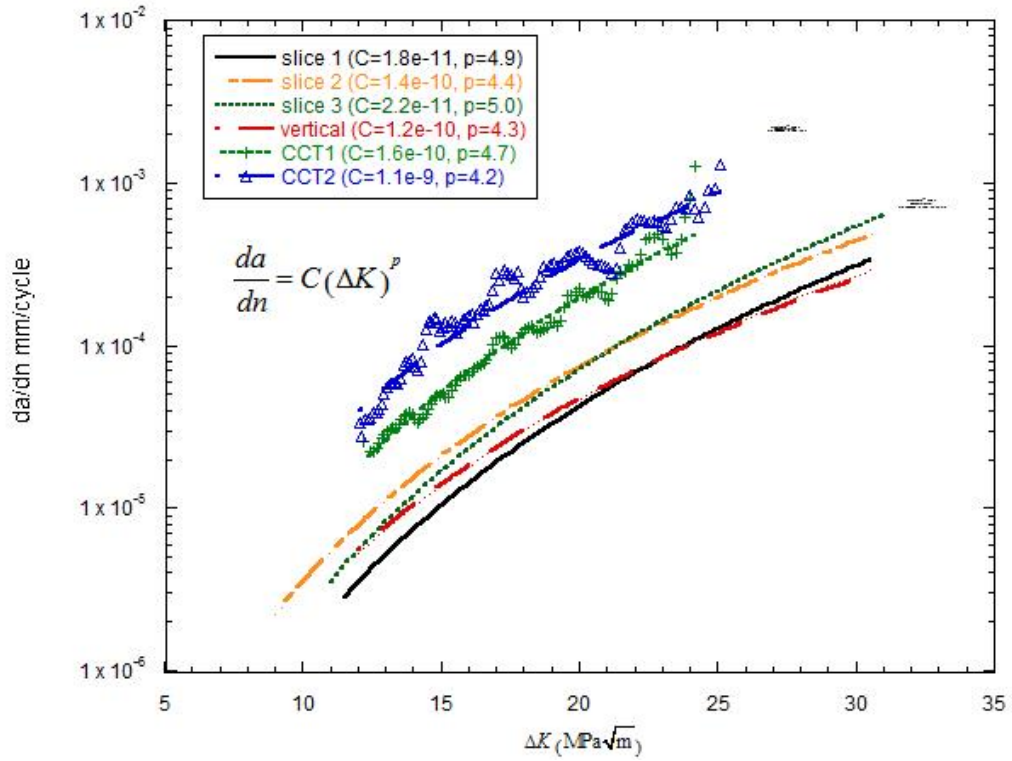

Figure 90 – Comparison of fatigue crack growth rates from CT and CCT specimens for AHH rail. *R*=0.1.

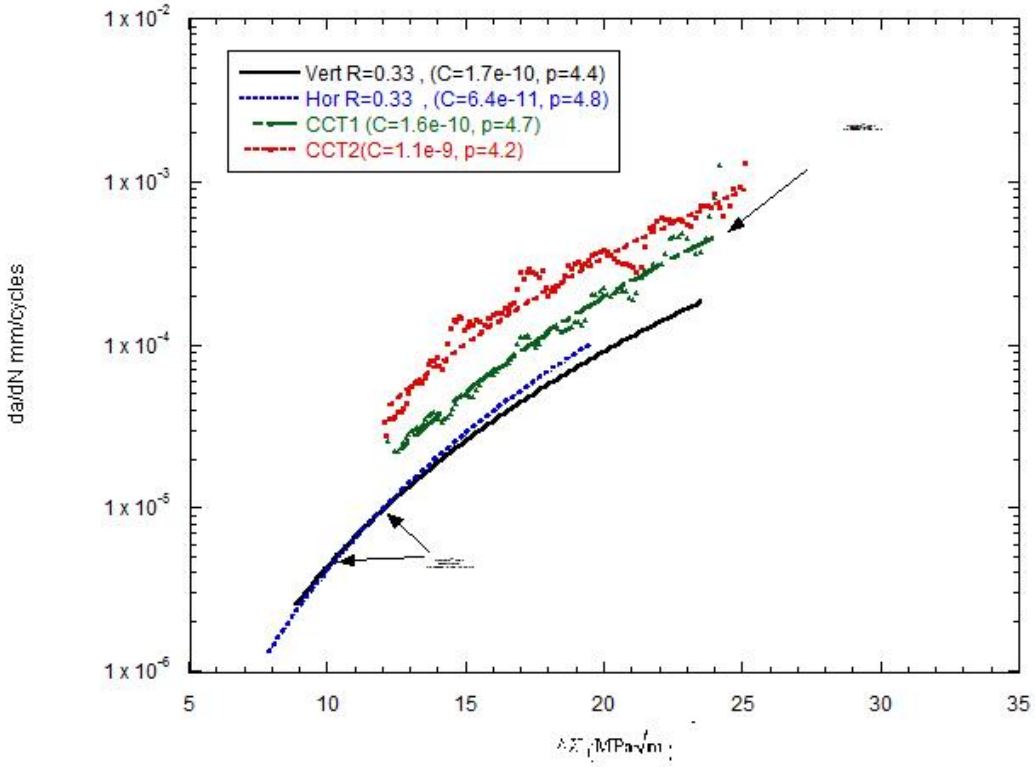

Figure 91 – Comparison of fatigue crack growth rates from horizontal and vertical CT specimens (*R*=0.33) with CCT specimens from the AHH rail.

3.8 Residual stresses

The importance of the residual stress effects on fatigue crack growth rates in legacy rails has been extensively investigated by Orringer et al. [29, 34]. The investigation was based on the simulated fatigue service tests conducted at the Facility for Accelerated Service Testing (FAST) of the US Transportation Test Center in Pueblo, CO. The data collected over the course of five months of simulated fatigue service tests showed existence of two groups with respect to detail fracture growth rate, as shown in Figure 92(a).

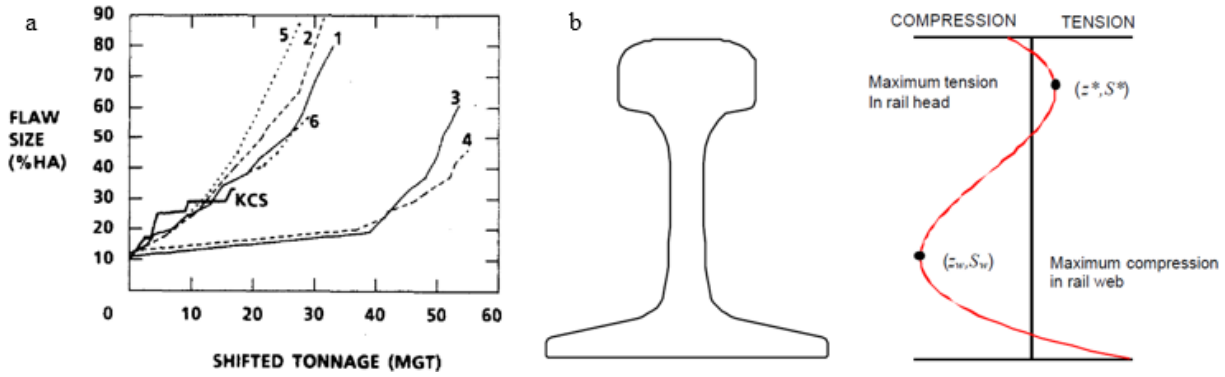

Figure 92 – Residual stresses effect on legacy rails: (a) Detail fracture growth curves with differences attributed to residual stresses [34], and (b) approximate distribution of the residual stresses through the rail height [23]

Since all the tested rails were nominally the same and subjected to the same loading conditions, significant differences in the observed crack growth rates between two rail groups in Figure 92(a) (1, 2, 5, 6 vs. 3, 4) were attributed to the differences in railhead residual stress.

There are several important sources of residual stresses in rails: roller-straightening, heat treatment of the railhead and wheel-rail contact. Modern rails produced for continuously welded track are roller straightened (i.e. cold worked) to meet strict tolerances on residual vertical camber and horizontal sweep. The residual stress field resulting from this process is approximately axially uniform except for ~18in at each rail end. Previous experimental stress analyses have characterized the axially uniform region, which includes a tensile axial stress in the railhead [6]. Another important source of residual stresses in rails is the wheel-rail contact stress that causes local yielding of the rail. Previous microhardness measurements showed that the railhead is work-hardened by the wheel-rail contact to a depth of about 0.25cm below the running surface and inward from the gage face. The axial residual stress is compressive in this region, and its magnitude approaches the work-hardened yield strength. An internal pocket of axial tension is also found in the heads of both roller straightened and manually straightened rails [34]. While we recognize the importance of the residual stresses caused by the local plastification due to wheel-rail contact, reliable quantification of these stresses would require extensive experimental measurements conducted on service-worn rails, which is beyond the scope of the current project.

Introduction of the head-hardening process of modern rails produces a slight hardness gradient (as discussed above) as well as the residual stress. The non-uniform cooling of the railhead results in a non-uniform, self-equilibrating stress distribution through the height of the rail, which effectively contributes to the stress range as well as the R value. An example of the residual stress distribution through the height of the rail section is shown in Figure 92(b) [23]. We note the compressive residual stress near the running surface of the rail turns into tension for most of the head. As a result, a propagating detail fracture can encounter changing residual stresses. Thus, accurate

assessment of residual stresses in modern head hardened rails is necessary for determining its influence on the fatigue crack growth rate and for establishing optimum inspection intervals.

A series of neutron diffraction measurements was performed at the Center for Neutron Research of the National Institute of Standards and Technology (NIST), Gaithersburg, MD and at Fraunhofer Institute to determine three-dimensional stress state in modern rails investigated here. Since all rails investigated here were unused, the residual stresses in these rails are due to the head hardening process and roller-straightening (i.e. no wheel-rail contact effects). 8mm thick plane stress cross-sectional rail slices cut from all investigated rails (i.e. AHH, HH, SS, CF&I77, HAY84) were used to measure in-plane residual stress distribution. Additionally, a longitudinal residual stress measurement in the AHH rail was conducted using a 3-D half-rail specimen, cut along its axis of symmetry (Figure 97).

A basic principle of neutron diffraction measurement method as well as its limitations that affect the number and type of specimens used are discussed in the next section of the report. Detailed finite element analyses conducted to optimize the specimens and aid in interpretation of the results are also described in the following sections, followed by the discussion of the measurement results obtained by NIST and Fraunhofer.

3.8.1 Neutron diffraction measurements

Neutron diffraction measurement technique relies on behavior of the diffracted beam of neutrons, which follow Bragg's law:

$$2d\,sin\theta = n\lambda \tag{1}$$

where d is the atomic lattice spacing, θ is the diffraction angle and λ is the wavelength. Internal stress in the crystallographic material, such as steel, causes changes in the lattice spacing, i.e. $\Delta d = d - d_0$. This change leads to change in the diffraction angle $\Delta\theta$, which can be accurately measured using a beam with constant wavelength λ. This is schematically illustrated in Figure 93.

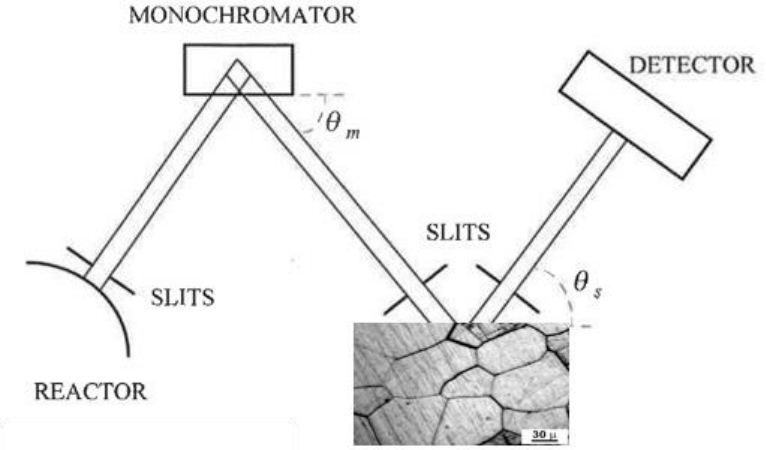

Figure 93 – Neutron diffraction measurement schematic [12]

By differentiating Bragg's law and using the reference configuration in the stress-free condition (d_0, θ_0), strains and stresses in the material can be determined, as follows:

$$\Delta\theta = -\frac{\Delta d}{d_0} tan\theta_0 = -\varepsilon\, tan\theta_0 \;\rightarrow\; \varepsilon = -\Delta\theta\, cot\theta_0 \;\; ; \;\; \sigma = E\varepsilon \tag{2}$$

One of the main advantages of using neutron diffraction, as opposed to x-ray diffraction is deeper penetration of neutrons into engineering materials (i.e. centimeters rather than millimeters for synchrotron x-rays or μm for laboratory x-rays). However, significant beam time is necessary to achieve sufficient penetration depths for accurate measurements inside the material, which constrains the size of the specimens that can be efficiently characterized. On the other hand, cutting the rail specimens for neutron diffraction measurements relives residual stresses. Thus, careful planning of different cuts is necessary along with quantification of the stress relief mechanisms introduced by these cuts. This was performed using detailed finite element analyses, as discussed in the following section of the report.

3.8.2 Specimen optimization and residual stress analyses

Residual stresses are three-dimensional and self-equilibrating, which indicates a complicated distribution through the height and width of the railhead. Specimen optimization is therefore a compromise between minimizing the beam time (i.e. measurement time) by minimizing the specimen size, and preserving the residual stress state that exists in a full rail. Cutting the rail introduces free boundaries and relieves stresses in the direction normal to the cut surface. Thus, the specimen geometry needs to be considered in the context of the direction of stresses being investigated. Lateral and transverse residual stresses can be effectively determined using thin rail slices. Longitudinal stresses, on the other hand, require a long rail specimen that preserves the stress distribution along the rail. Figure 94 gives an example of the residual stresses measured by Luzin et al. [16] using full rail sample of 530mm length (top row), and corresponding thin slice measurements (bottom row).

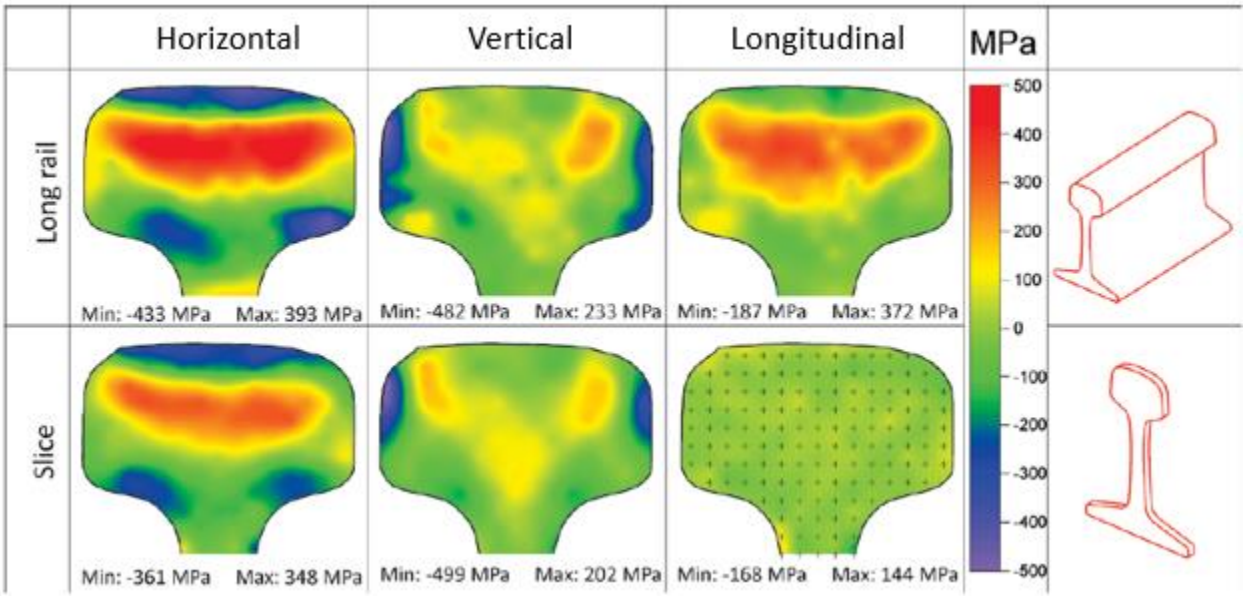

Figure 94 – Example of residual stress measurements using full rail sample (top) and thin rail slices (bottom) [16]

As indicated in Figure 94, thin rail slices, which require relatively small amounts of beam time, provide reliable information about lateral and transverse stress distribution. However,

determination of the longitudinal stresses requires a long rail sample, which at 530mm used by Luzin et al., required approximately 3 months of beam time. This amount of beam time is practically not achievable, considering limited number of nuclear facilities that perform neutron diffraction measurements. In the same time, while lateral and transverse stresses are certainly important, the most consequential stress component for detail fracture growth is the longitudinal one. Thus, it is very important to determine the minimum size and shape of the rail specimen that preserves the longitudinal stress distribution. This will be performed by investigating the effects of different types of rail specimen cuts and resulting change in the stress distribution. We first investigate two transverse cuts to determine the minimum rail specimen length. Subsequently, we investigate the effect of the longitudinal cut along the mid-section of the rail that splits the long rail specimen in half (longitudinally). The effects of these cuts on the residual stress state in the rail are analyzed using detailed finite element simulations.

TRANSVERSE CUTS

The main objective of the analysis conducted here is to determine the minimum length of the rail specimen that preserves the longitudinal residual stress. A detailed finite element representation of the full rail (136RE) geometry is used to reach this objective. Since residual stresses are elastic, the material model used in the analyses is also elastic.

There are many approaches to introduce self-equilibrating residual stresses into the rail finite element model. The approach followed here involves introducing two virtual cuts to the infinite rail model, and applying longitudinal stress that is equal and opposite to the one measured in the legacy rail (as shown in Figure 92(b)), modified to ensure that it is self-equilibrating (i.e. both the total force and moment are zero). This is equivalent to cutting the physical rail and relieving the locked-in residual stresses, and then reapplying equal and opposite self-equilibrating stress to one of the free rail surfaces. This exercise was repeated for different effective lengths of the models (ranging from 10–30cm) to examine the distance over which the applied stresses decay. The analysis results obtained with a 12cm rail model (half-length due to symmetry) are shown in Figure 95.

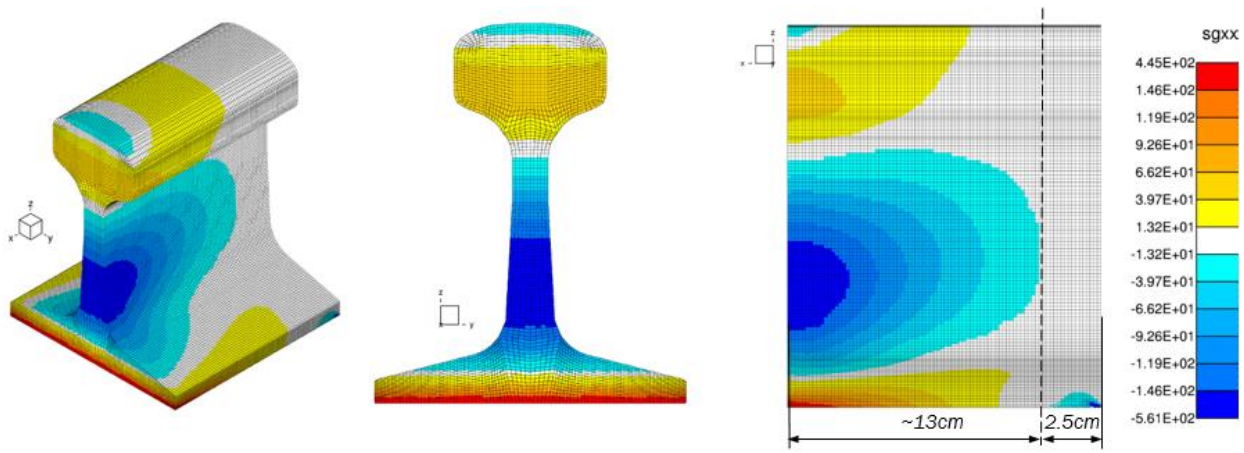

Figure 95 – Longitudinal residual stress distribution; 15cm rail model (units MPa).

The analysis results show the expected pattern of longitudinal stresses that match the applied stress near the application surface (left side of the model in Figure 95) and relatively fast decay as the free end is approached. The distance over which the stresses decay is approximately 13cm, which is less than the height of the rail (18.5cm – 136RE). The analysis was repeated using longer models,

until the length over which the stresses decay did not increase significantly. Since there was no significant increase in the decay length calculated using 20cm and 25cm rail models, compared to the 15cm rail model, the minimum length of the rail specimen was determined to be 30cm (i.e. 2x15cm).

It is also worthwhile to examine the lateral stress in the rail resulting from application of the longitudinal stress. These results are presented in Figure 96.

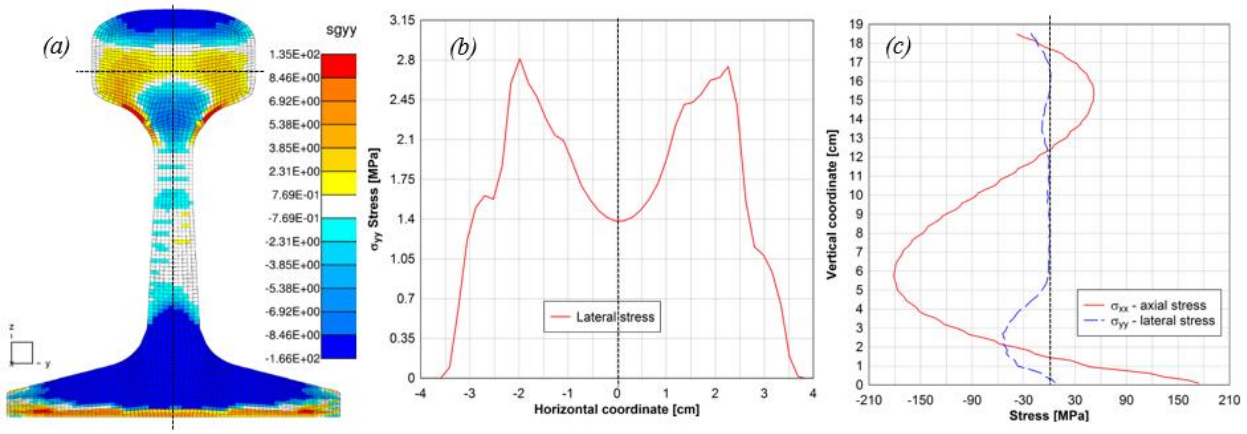

Figure 96 – Lateral stress induced by the application of the longitudinal stress: (a) lateral stress maps on the rail surface where longitudinal stress was applied; (b) lateral stress across the width of the railhead; (c) longitudinal and lateral stresses along the height of the rail (units MPa, length in cm)

The analysis results indicate that the lateral stress caused by the application of the longitudinal stress is practically negligible. This suggests that the effect of longitudinal stress on the lateral stress is not significant for this rail geometry. It would be important to understand if reverse is also true, i.e. investigate the longitudinal stress caused by the application of the lateral stress. This is consequential for investigation of the effects of the longitudinal cut along the middle section of the rail, which will be considered next.

LONGITUDINAL CUT

Considering the available beam time for the residual stress measurements at any neutron diffraction beam facility, further specimen size reduction is necessary. A longitudinal cut through the middle section of the rail was proposed, as shown in Figure 97.

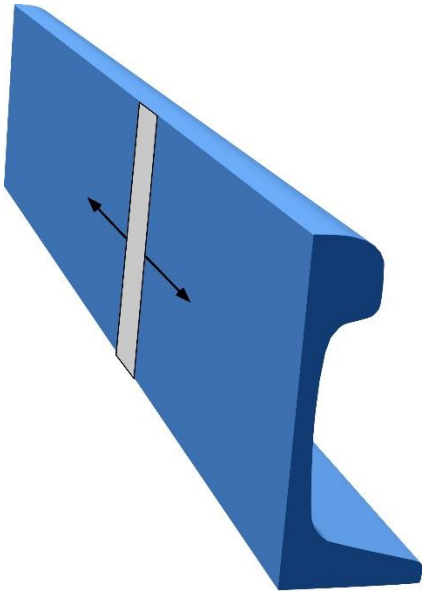

Figure 97 – Proposed rail specimen for longitudinal stress measurements – longitudinal cut along the mid-section of the rail

Interpretation of the residual stress measured with the rail specimen shown above requires careful consideration of the effect of the longitudinal cut on the stress distribution inside the rail. It is clear that a longitudinal cut is going to significantly change the lateral (i.e. horizontal) stress distribution in the rail. It is not clear, however, what effect it will have on the longitudinal stress state.

The transverse cuts analyses discussed above indicated that application of the longitudinal stress has limited influence on the lateral stress. If the reverse is also true, i.e. the influence of lateral stress on the longitudinal stress state is limited, then the longitudinal cut would affect primarily the lateral stress in the rail, while the longitudinal stress would remain approximately the same as before the cut was introduced. This scenario is analyzed using the same methodology as in the case of the transverse cut investigation. A detailed finite element model of the rail is used with a longitudinal cut shown in Figure 98. Lateral stress σ_{yy} is applied onto the free surface created by the cut, where the stress distribution is obtained from the literature data (Kelleher et al. [29]). The applied stress was modified to ensure that it is self-equilibrating. Additionally, the maximum stress levels were reduced by a factor of 10 to ensure elastic behavior of the new half-rail section. This is equivalent to longitudinally cutting the physical rail and relieving the locked-in stresses, and then reapplying equal and opposite self-equilibrating transverse stress to the surface created by the cut. The finite element model along with the applied transverse stress is shown in Figure 98.

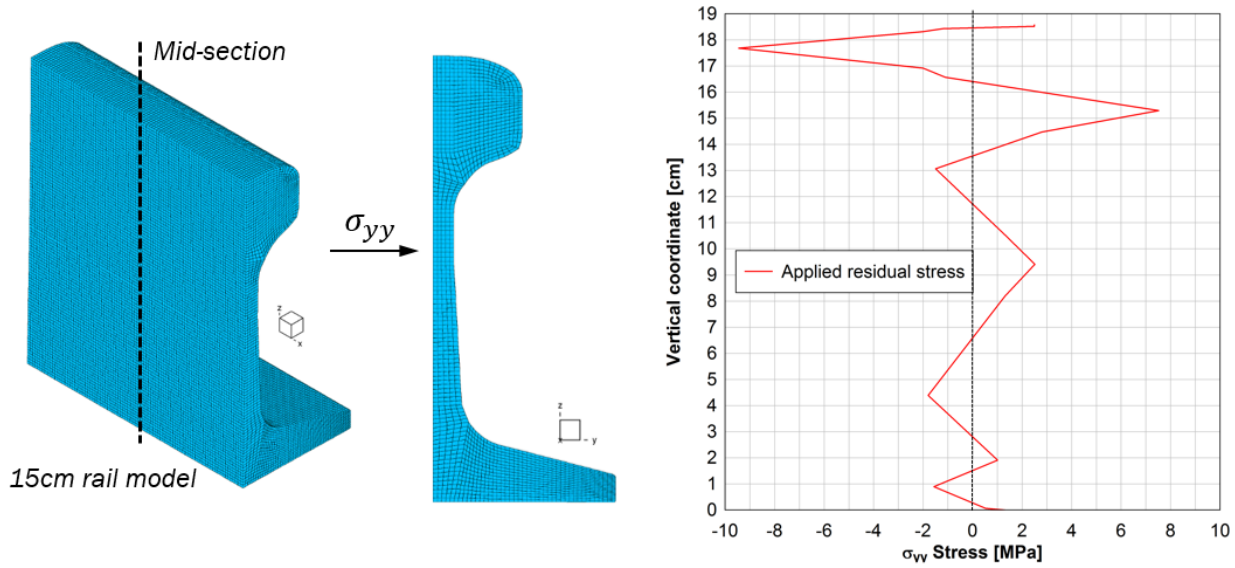

Figure 98 – Investigation of the effect of longitudinal cut: 15cm half-rail model with lateral stress applied on the surface of the cut (applied lateral stress profile from ref [29]).

The results of the half-rail finite element analysis are given in Figure 99.

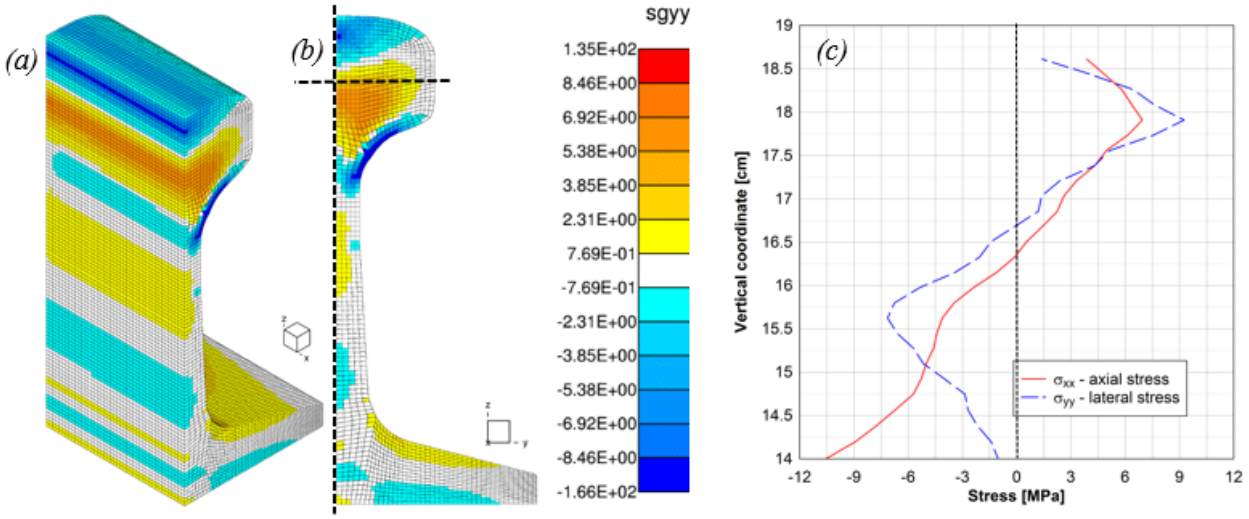

Figure 99 – Longitudinal stress induced by the application of lateral stress: (a) applied lateral stress maps on the longitudinal middle surface – isometric view; (b) applied lateral stress on the middle surface of the rail; (c) longitudinal and lateral stresses along the height of the railhead (units MPa, length in cm)

The analysis results indicate that the longitudinal stress induced by the application of the lateral stress is on the same order as applied lateral stress. This means that significant changes of the lateral stress result in similar changes in longitudinal stress. Since the magnitude of the lateral residual stresses in the rails is typically similar to the longitudinal stress (Figure 94 [16]), relieving the lateral stress by introducing the investigated cut has a significant effect on the longitudinal stress state. In other words, the longitudinal cut does change the state of both lateral and longitudinal stresses in considered rail geometry (136RE).

The residual stress analyses discussed above indicate a complex interaction between different stress components in the rail. Thus, cutting the rail for neutron diffraction measurements requires careful investigation of the effects of various cuts on the residual stress state. We note that the analyses discussed here were performed based on data from published literature, as opposed to stress measurements conducted in support of the project. This is because the analyses were conducted to optimize the specimen and were completed before measurements were taken. Additionally, and more importantly, half-rail specimens (Figure 97) were used to measure the longitudinal residual stress, which are affected by the longitudinal cut, as the analysis above shows. Thus, the residual stress measurements taken here, while very important and valuable, provide only a partial representation of longitudinal residual stresses. Obtaining a complete representation would require solution of an inverse problem, i.e. determining the stress state that existed in the rail before the cut, based on stresses measured using cut specimen (i.e. half-rail – Figure 97). This will be pursued as part of the follow on effort.

3.8.3 Neutron diffraction residual stress measurements

Residual stress measurements using neutron diffraction techniques were conducted by Dr. T. Gnaupel-Herold, at NIST's Center for Neutron Research, in Gaithersburg, MD. Three separate sets of residual stress measurements were conducted at NIST: 1) Plane stress residual stress measurements on 8-mm thick cross-section slices taken from AHH, HH, and SS rails (Figure 100), 2) Plane stress residual stress measurements on 8-mm thick cross-section slices taken from the HAY84 and CF&I77 rails, and 3) 3-D residual stress measurements using ½ of an AHH rail cut along its axis of symmetry (Figure 97 and Figure 100b). The residual stress measurements for the planar slices where conducted using a wavelength of 1.637 Å over a gauge volume of 42.875 mm^3 (3.5 x 3.5 x 3.5 mm cubes). The reported residual stress values are based on a grid spacing interval of 3 mm x 3 mm, with the grid plane located at the half-thickness of the rail slice, as shown in Figure 101.

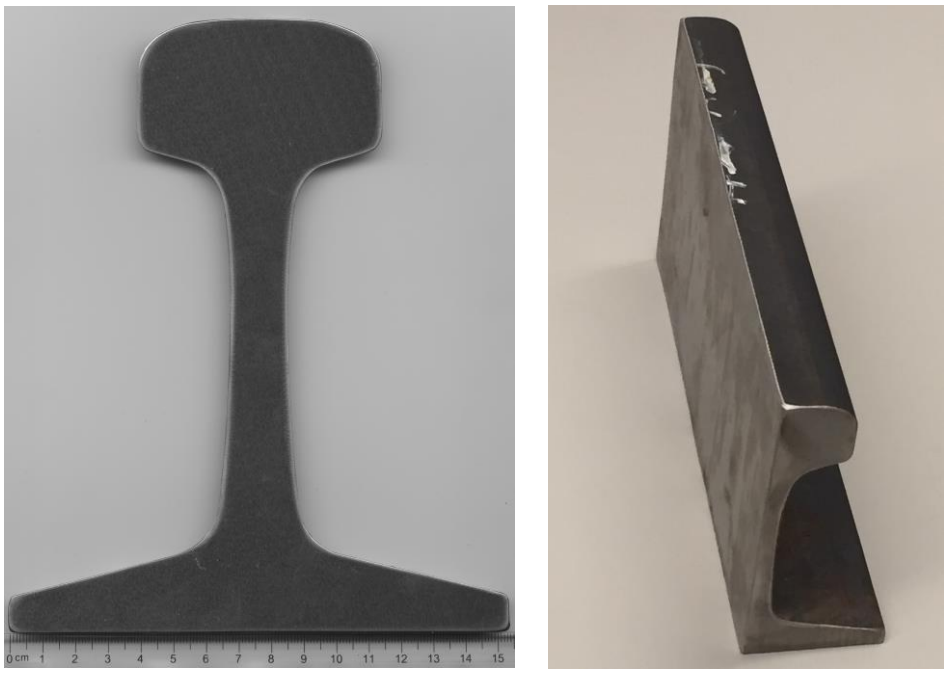

(a) (b)

Figure 100 – Specimens for the residual stress measurements: (a) 8-mm thick cross-sectional slice used for plane stress measurements (i.e. no longitudinal component), and, (b) 300mm half-rail specimen used for longitudinal residual stress measurement.

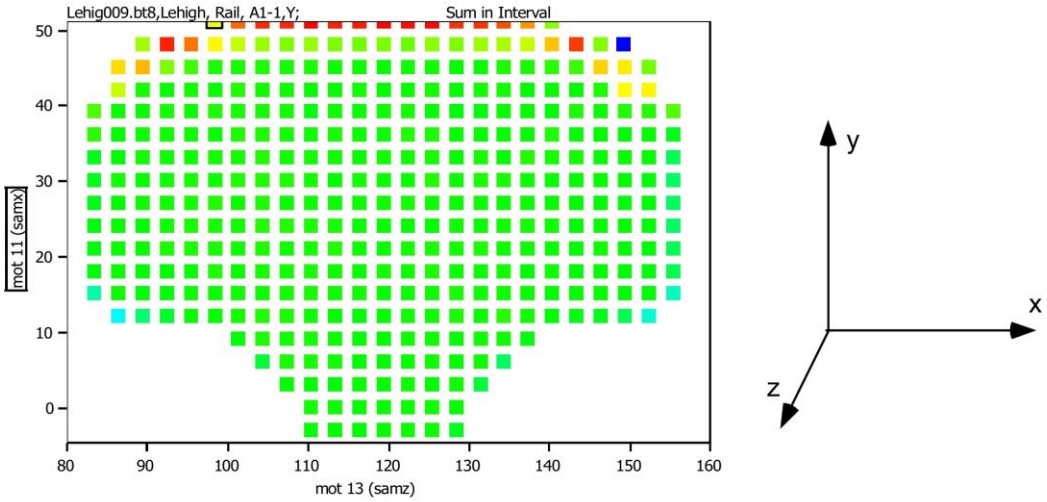

Figure 101 – Grid of 384, 3-mm x 3-mm, residual stress measurement areas in slice mid-plane (a different coordinate system was used than the one in Section 3.8.2)

As expected, the neutron diffraction residual stress measurements showed that the longitudinal stress component σ_{zz} (note different coordinate system than in used in the analyses in Section 3.8.2) is zero for all planar slices. The σ_{xx} (lateral) and σ_{yy} (transverse) stress contours for the HH, AHH, and SS rails are shown side by side in Figures 102 – 103. A minimum lateral compressive residual stress, $\sigma_{xx} = -262$ MPa, was measured close to the running surface of the

HH rail (Fig. 102a) and a maximum tensile residual stress, $\sigma_{xx} = 102$ MPa, was measured close to the center of the head in the AHH rail (Fig. 102b). Referring to Figure 103, it's interesting to note that the maximum and minimum σ_{yy} stress components both occur in the SS rail (Fig. 103c): $\sigma_{yy}^{\min} = -192$ MPa, $\sigma_{yy}^{\max} = +162$ MPa. The details of these maximum measured residual stress values from contour plots Figs. 102a, 102b, and 103c are shown enlarged in Figs. 104 - 106.

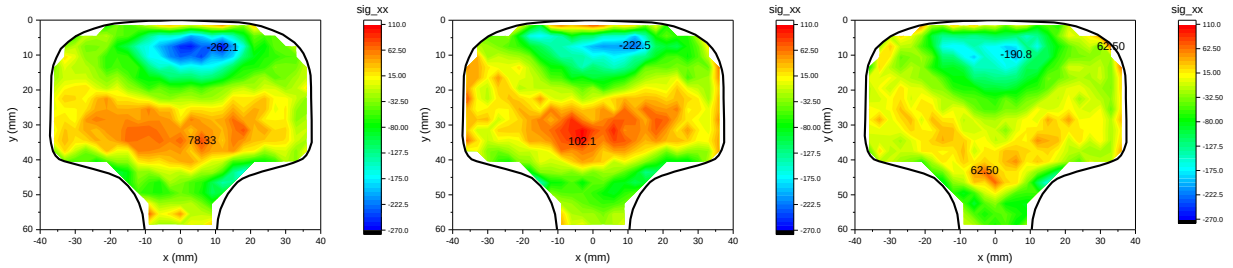

(a) (b) (c)

Figure 102 – Contour plots comparing the lateral residual stress component σ_{xx} in rails: (a) HH, (b) AHH, and (c) SS respectively. Scale -270 MPa (blue) – 110 MPa (red).

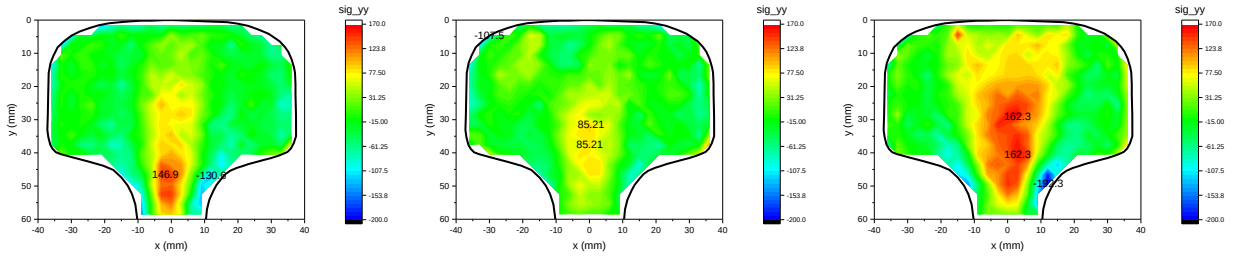

(a) (b) (c)

Figure 103 – Contour plots comparing the transverse residual stress component σ_{yy} in rails: (a) HH, (b) AHH, and (c) SS respectively. Scale -200 MPa (blue) – 170 MPa (red).

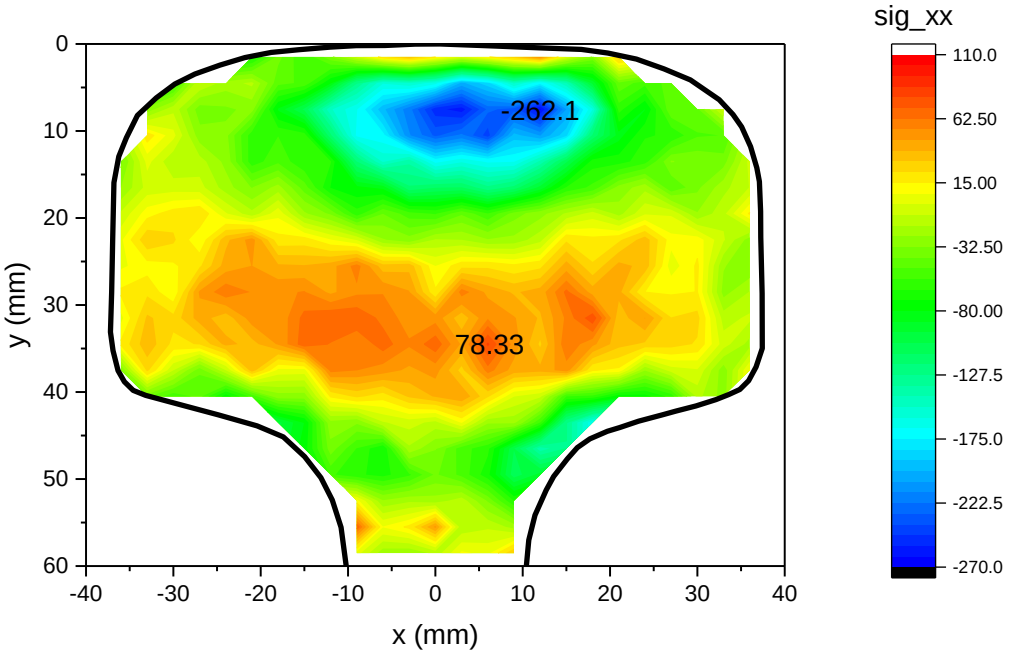

Figure 104 – Enlargement showing lateral residual stress contours for HH rail (S_{xx}).

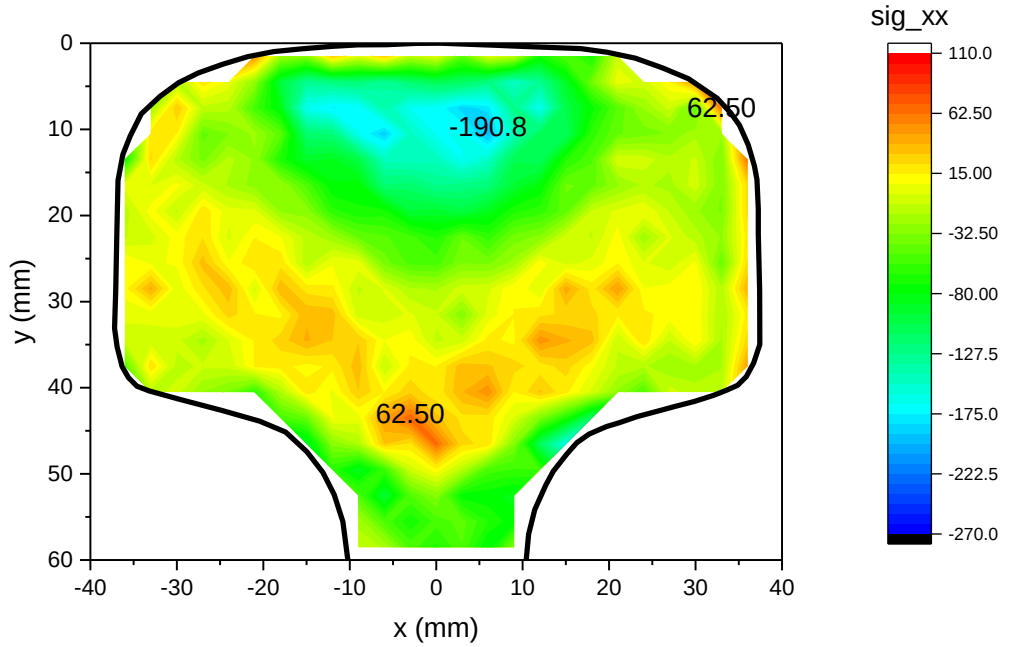

Figure 105 – Enlargement showing lateral residual stress contours for AHH rail (S_{xx}).

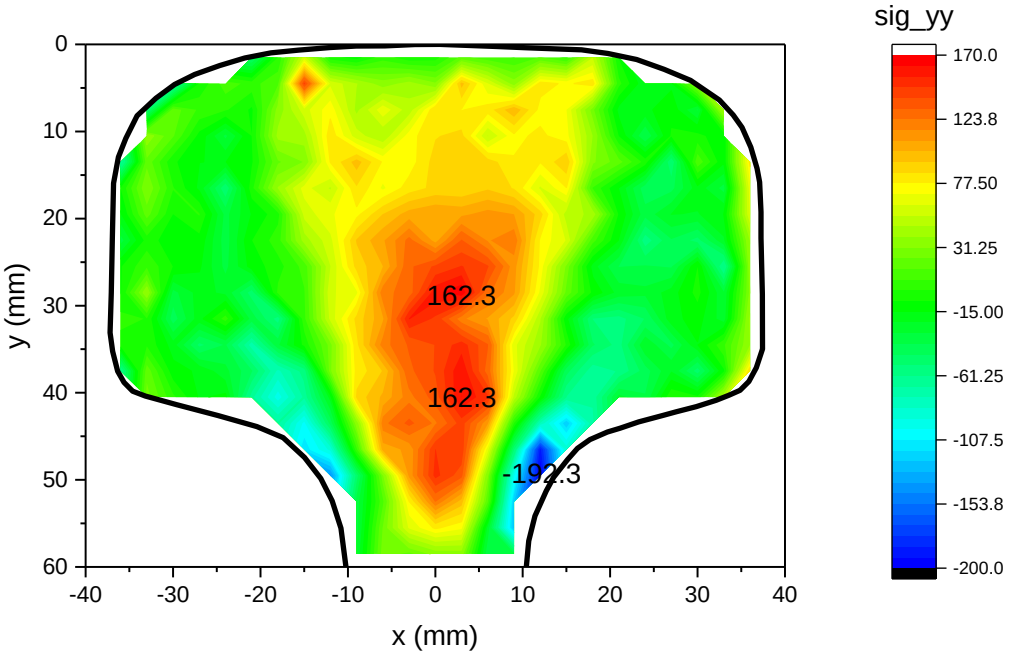

Figure 106 – Enlargement showing transverse residual stress contours for SS rail (σ_{yy}).

As shown in Figure 106, in the SS rail, the maximum σ_{yy} in tension is located in the central portion of the rail head, while the maximum compressive σ_{yy} occurs on the rail surface at the transition from the flange to the rail head.

NIST also measured the planar residual stresses, σ_{xx} (lateral) and σ_{yy} (transverse), in the legacy rails, HAY84 and CF&I77. The stress components for the HAY84 rail are shown in Figure 107 and for the CF&I77 rail in Figure 108. The residual stresses in the legacy rails are considerably lower than the stresses measured in the modern rails. As can be seen by comparing these figures, the minimum and maximum residual stresses are slightly higher in the HAY84 rail. For example, in the HAY84 rail (Fig. 107) the minimum and maximum σ_{xx} residual stress components are: $\sigma_{xx}^{\min} = -144\text{MPa}$, $\sigma_{xx}^{\max} = +57\,\text{MPa}$, and the minimum and maximum σ_{yy} residual stress components are: $\sigma_{yy}^{\min} = -89\,\text{MPa}$, $\sigma_{yy}^{\max} = +77\,\text{MPa}$. This can be contrasted with the residual stresses in the CF&I77 rail (Fig. 108), where the equivalent minimum and maximum σ_{xx} residual stresses are: $\sigma_{xx}^{\min} = -55\text{MPa}$, $\sigma_{xx}^{\max} = +56\text{MPa}$, and the minimum and maximum σ_{yy} residual stresses are: $\sigma_{yy}^{\min} = -39\,\text{MPa}$, $\sigma_{yy}^{\max} = +52\text{MPa}$.

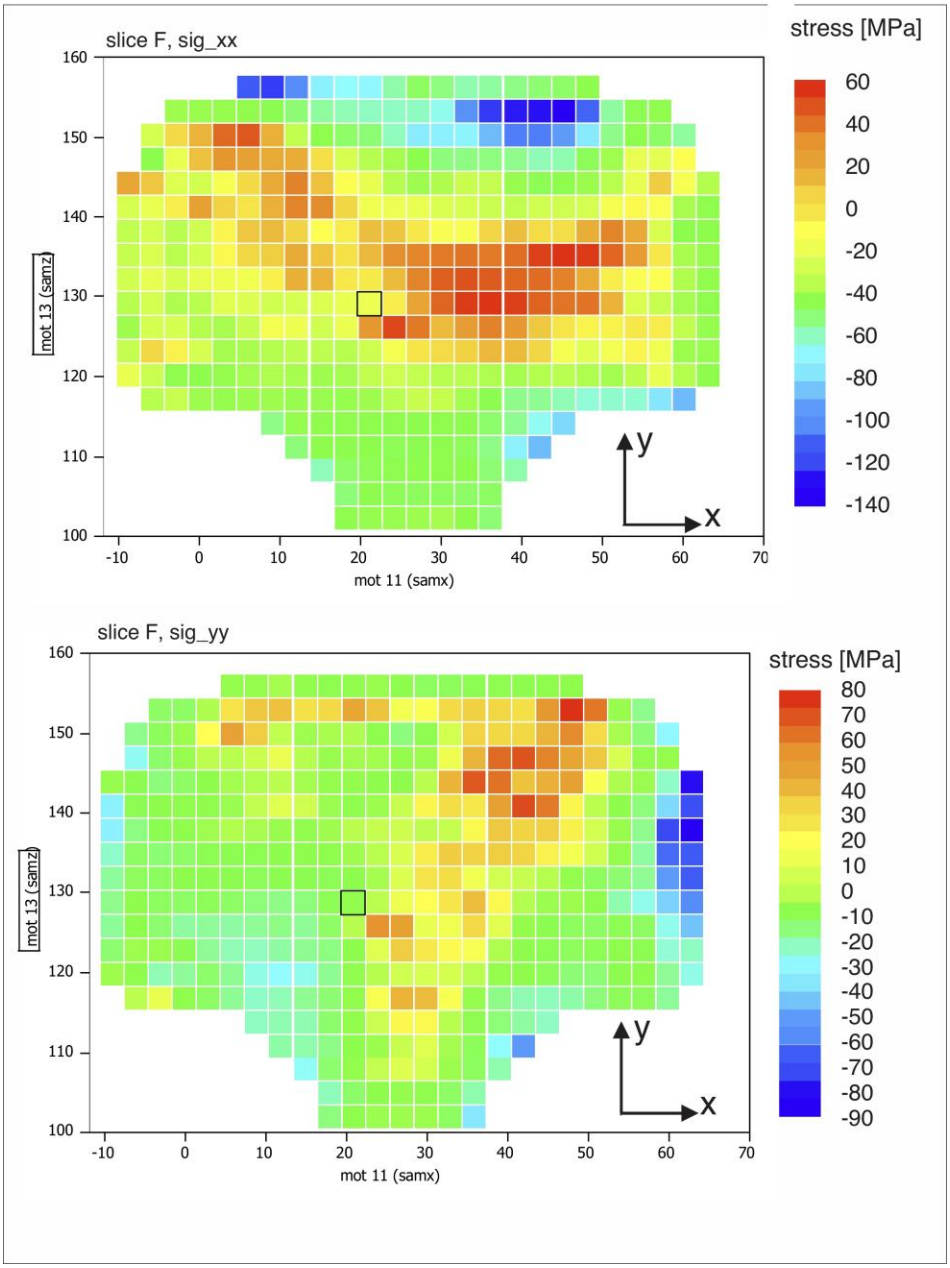

Figure 107 – Residual stresses S_{xx} and S_{yy} in the legacy HAY84 rail.

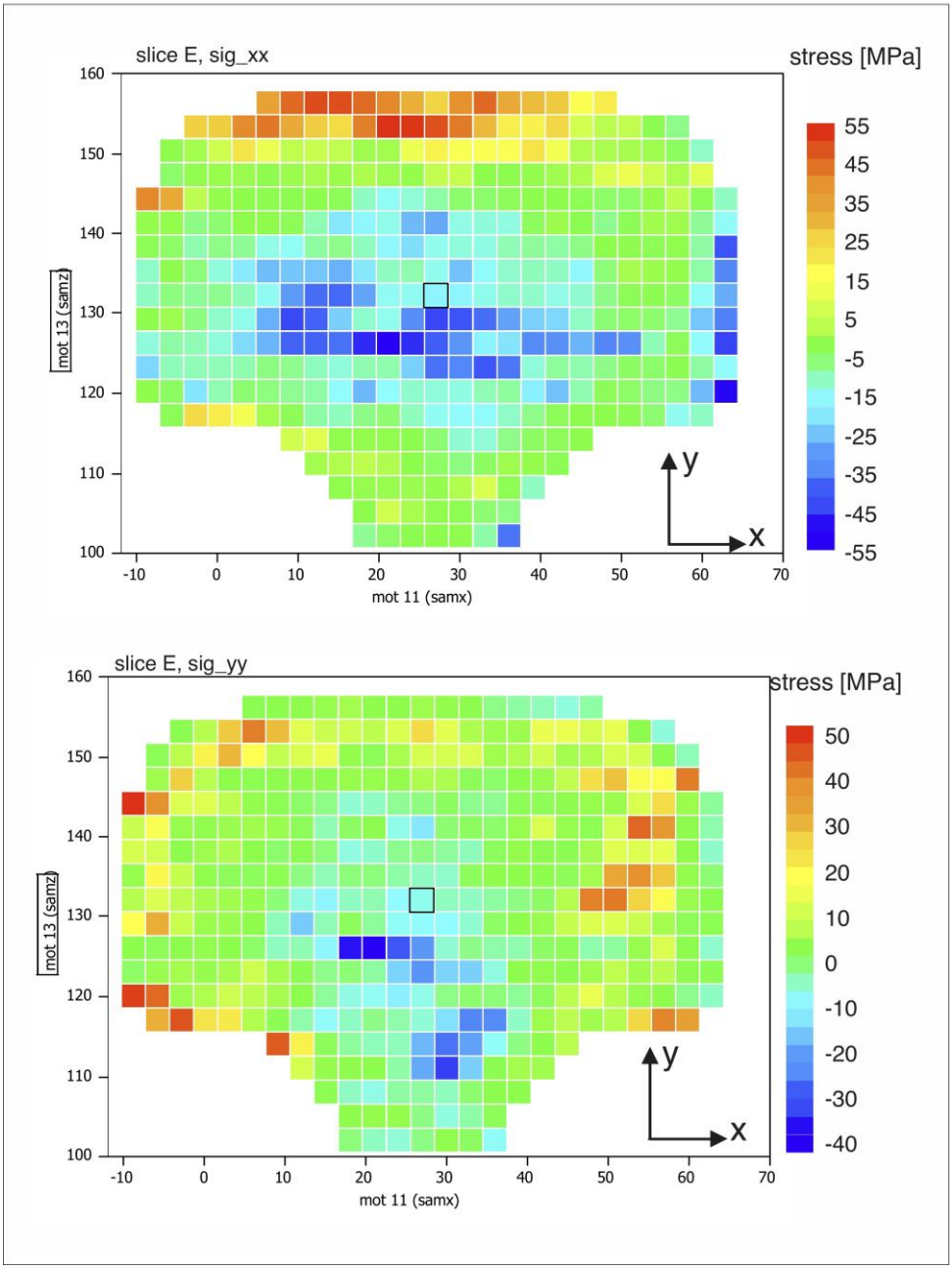

Figure 108 – Residual stresses σ_{xx} and σ_{yy} in the legacy CF&I77 rail.

Measurement of the longitudinal residual stresses using neutron diffraction cannot be conducted using rail slices discussed above, since cutting these slices relieves the longitudinal stresses. A full 3-D section of rail is needed to measure longitudinal residual stresses (Section 3.8.2), which is very challenging, as it requires an excessive amount of beam time, e.g., weeks of continuous measurement. An attempt was made by Dr. M. Farajian of Fraunhofer Institut für Werkstoffmechanik (IWM), Freiburg, Germany to make a limited number of longitudinal residual stress measurements, at selected points in the upper corner of the AHH rail. For these measurements, a 300 mm long section of the AHH rail was placed in the neutron beam source at the Helmholz-Zentrum Berlin (HZB). Figure 109 shows the AHH rail test specimen in the HZB

neutron diffraction residual stress measurement facility. Unfortunately, because of difficulties in making these measurements within a very limited time period, only preliminary residual stress measurements were obtained at the desired points (Figure 110). Dr. Farajian, who performed these measurements at no cost to the project, is very interested in completing these measurements when he can obtain beam time at HZB in the future, so this is a recommend item for future work.

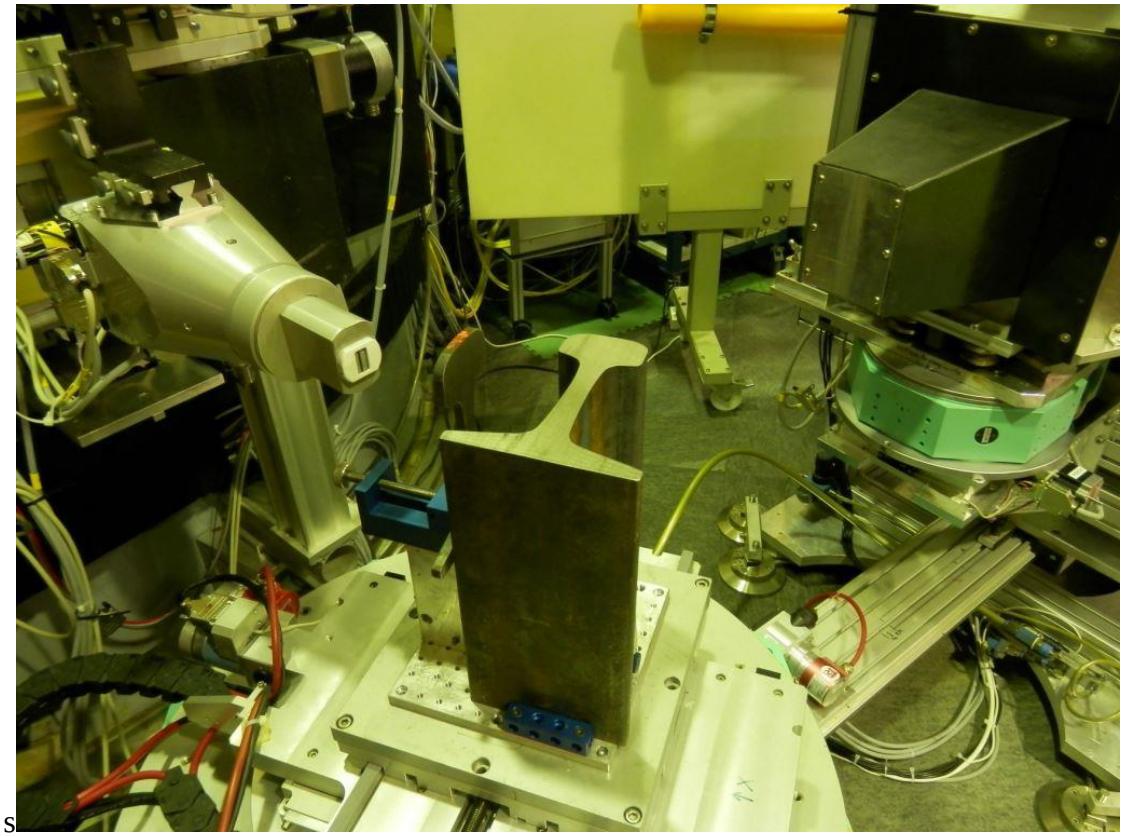

Figure 109 – Residual stress measurements on a 300 mm section of the AHH rail using the neutron source at Helmholz-Zentrum Berlin (HZB).

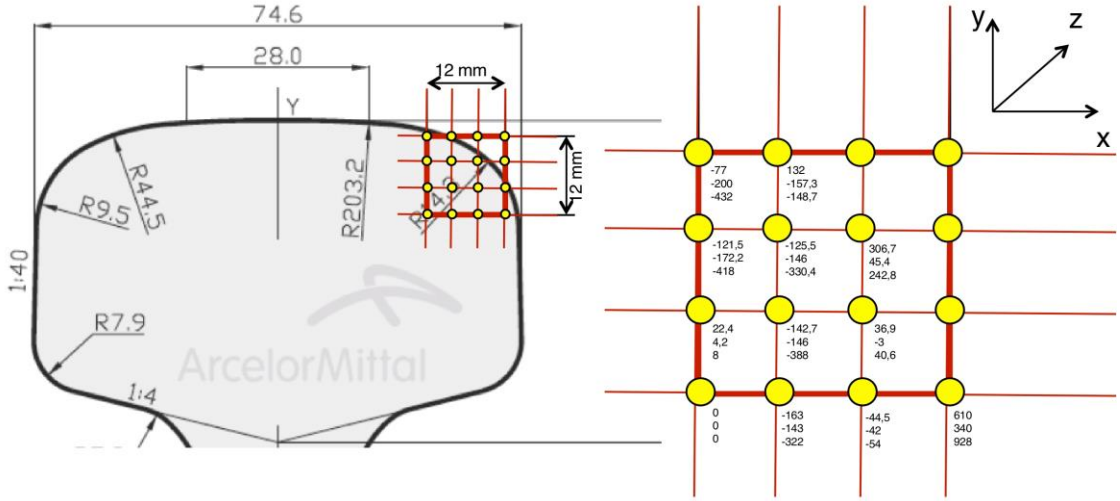

Figure 110 – Preliminary longitudinal residual stress measurements from corner of AHH rail.

After consultation with Dr. Gnaupel-Herold at NIST, a decision was made to attempt neutron diffraction residual stress measurements on a 300-mm long section of the AHH rail cut down the rail's axis symmetry as shown in Figure 100(b). This reduction in the mass substantially reduces the necessary beam time, but at the expense of altering the internal residual stresses, as discussed in Section 3.8.2. One of the conclusions of the analyses conducted to optimize the specimens for neutron diffraction measurements is that it is possible to combine finite element simulation with the residual stress measurements on ½ of the rail to approximate the longitudinal residual stresses. This will be investigated in detail in the next phase of the project.

Before examining the longitudinal residual stresses measured with a half-rail specimen shown in Figure 100(b), it is useful to investigate the lateral and transverse stresses and compare the results with the corresponding measurements made with the rail slices. Figure 111 shows a comparison of the lateral stress component (σ_{xx}) measured on the mid-plane of the long half-rail section, with the same stress component measured on the symmetric 8-mm thick (plane stress) slice (Fig. 105). The difference between these two residual stress measurements is striking. As expected, on the vertical plane of symmetry, σ_{xx} becomes smaller on the free surface of the split rail (Fig. 111a). However, it is not clear why large compressive stresses are reported at the top and bottom of the specimen (Fig. 111a), which appears to violate the traction-free boundary condition on the cut vertical plane of symmetry. Additionally, the tensile lateral stress measured on the vertical mid-plane of the half-rail section is significantly higher than the corresponding level obtained for the same rail with the plane stress slices. In the Fig. 111(a) image, $\sigma_{xx}^{\min} = -209$ MPa, $\sigma_{xx}^{\max} = +236$ MPa. In the symmetric, plane stress, cross-section, Fig. 111(b), $\sigma_{xx}^{\min} = -227$ MPa, $\sigma_{xx}^{\max} = +105$ MPa.

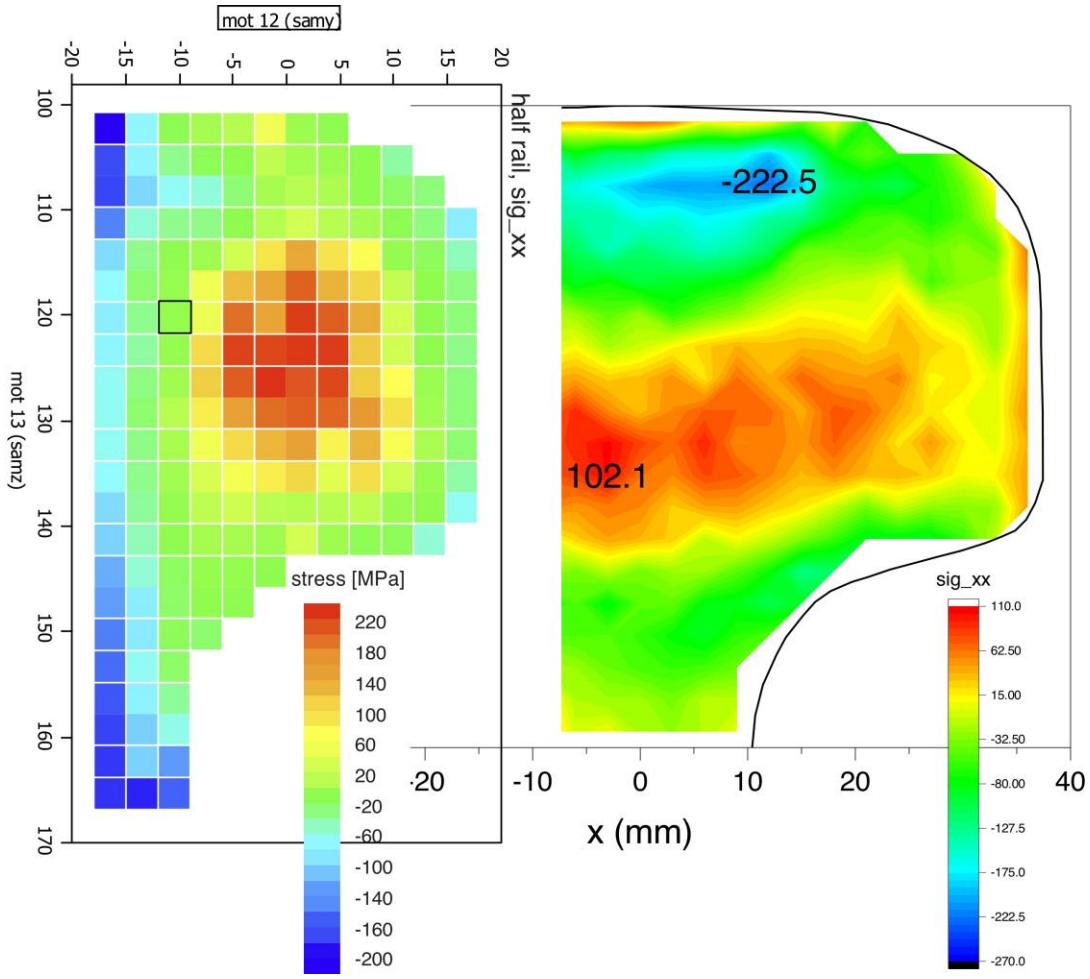

(a) (b)

Figure 111 – Comparison of the lateral residual stresses (σ_{xx}) measured in AHH rails: (a) σ_{xx} measured in 300-mm long half-rail section, (b) σ_{xx} measured in 8-mm thick planar section (Fig. 105).

Figure 112 shows a similar comparison for the transverse stress component (σ_{yy}). In Fig. 112(a) $\sigma_{yy}^{\min} = -188\,\text{MPa}$, $\sigma_{yy}^{\max} = +221\,\text{MPa}$. In the symmetric, plane stress cross-section shown in Fig. 112(b), $\sigma_{yy}^{\min} = -172\,\text{MPa}$, $\sigma_{yy}^{\max} = +152\,\text{MPa}$. While the peak compressive and tensile values appear similar, the distribution is not. Based on the available results, it is difficult to attribute these differences to any particular effect. However, it can be concluded that cutting the rail specimens for neutron diffraction measurements of residual stresses is very consequential for the actual stress distribution. This also indicates that the interaction between different stress components is even more consequential than suggested by the results of the finite element analyses discussed in Section 3.8.2.

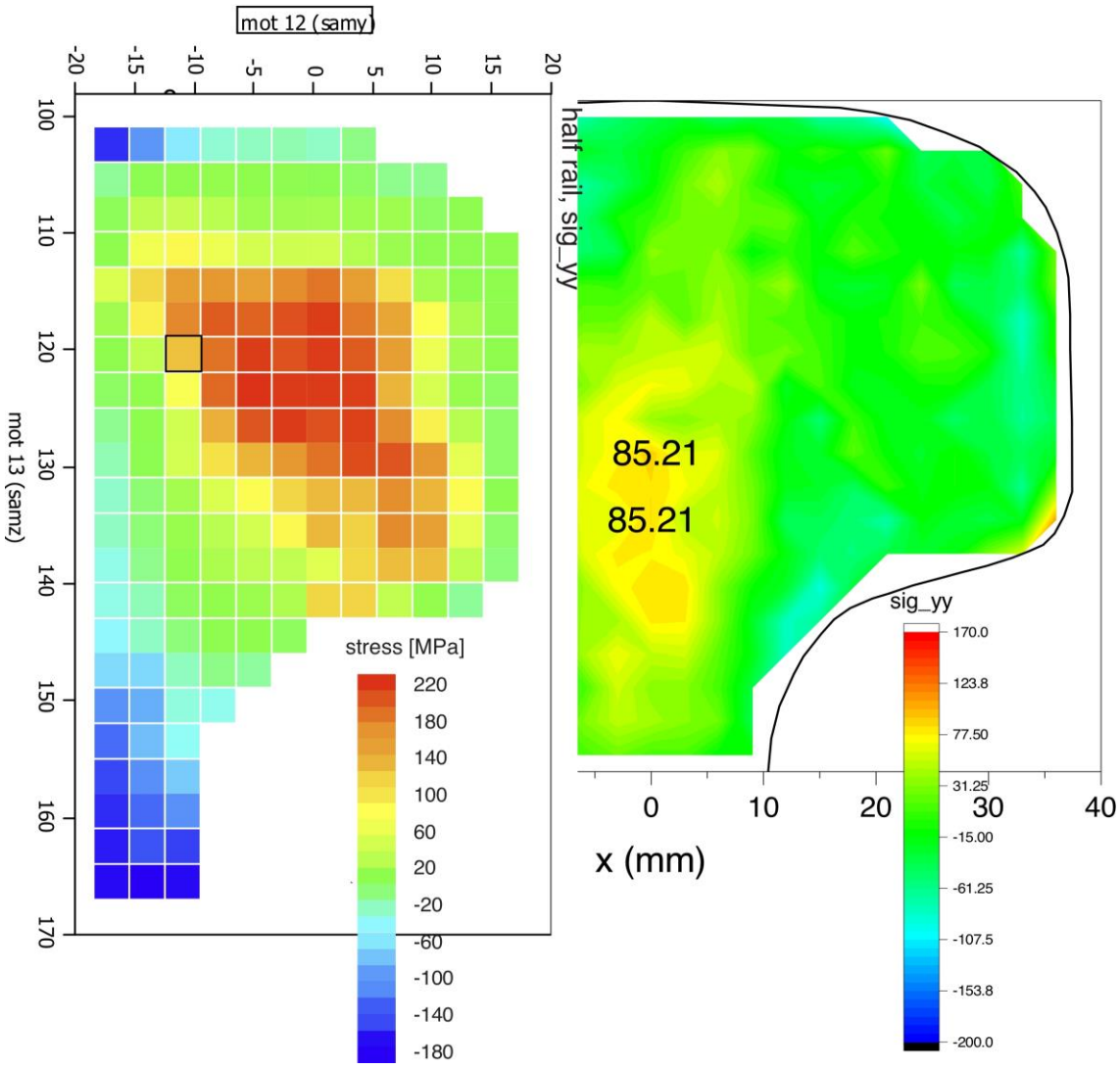

(a) (b)

Figure 112 – Comparison of the transverse residual stresses (σ_{yy}) measured in AHH rails: (a) σ_{yy} measured in 300mm long half-rail section, (b) σ_{yy} measured in 8-mm thick planar section (Fig. 103b).

Figure 113 shows the longitudinal stress component (σ_{zz}) measured in the center (i.e. mid-length) of the half-rail sample. The peak compressive stress is $\sigma_{zz}^{\min} = -222$MPa and the peak tensile stress is $\sigma_{zz}^{\max} = +356$MPa. High tensile stress in the rail head is especially important for transverse fracture growth. We note however, that the stress distribution shown in Figure 113, as well as the comparative analysis of the lateral and transverse stresses obtained with a 3-D half-rail and plane stress slices, point to complicated interaction between the stress components and significant effects of cutting the rail specimen. This makes a clear interpretation of the measured values and distribution of longitudinal residual stresses very challenging.

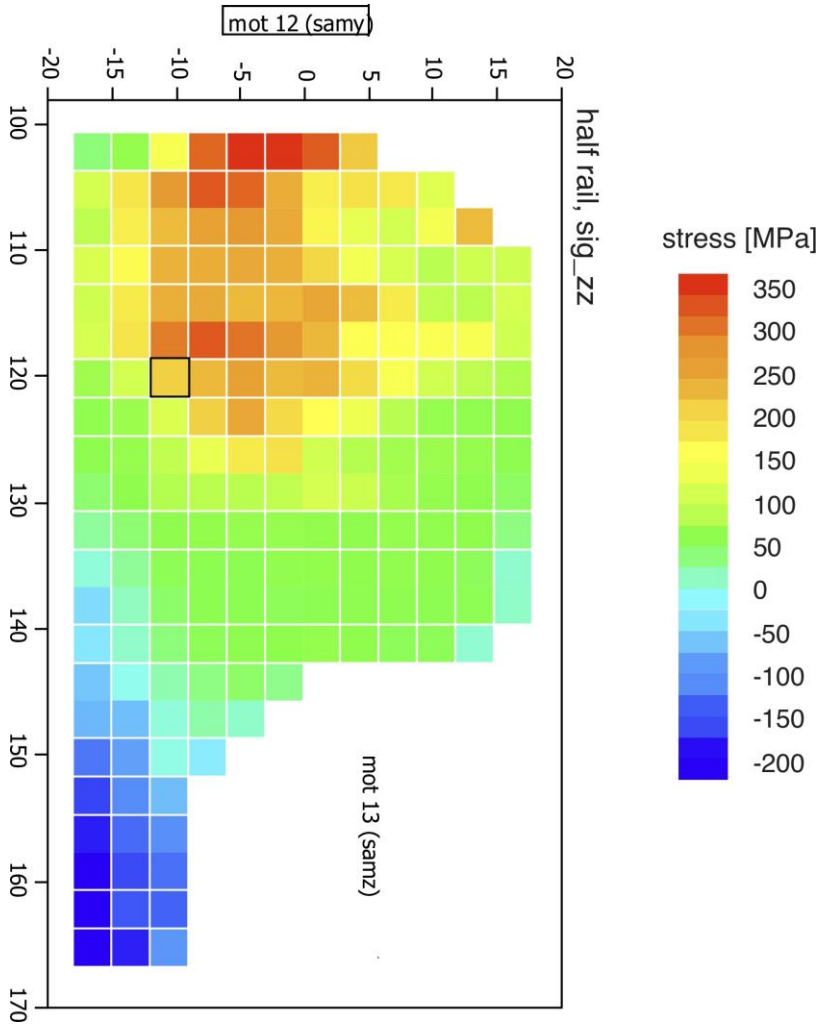

Figure 113 – Longitudinal (S_{zz}) stress component measured in the split 300-mm long AHH rail.

The analysis of the residual stress measurements conducted with the 3-D half-rail specimen points to complexities of the residual stress distribution in rails as well as significant challenges related to their measurement. Ideally, the residual stress measurements in all directions should be conducted with a full 3-D rail section (as opposed to half-rail) and repeated multiple times to verify the accuracy. Given the beam time required to perform such measurements, this is simply prohibitive. In the same time, clear interpretation of the residual stress state based on partial measurements conducted with half-rail specimens or plane stress slices, proved nearly impossible. These challenges can be alleviated, to a certain degree, through detailed finite element simulations aimed at recreating the stress state in the rail before it was cut. This however requires solution of the inverse problem, which is challenging in its own right. A residual stress analysis effort is envisioned for the next phase of this project, with a goal of approximating a full 3D residual stress distribution. However, we recognize that a separate, dedicated multi-year effort is required to fully understand the residual stress distribution in rails. Such an effort should involve both extensive new measurements supplemented by detailed finite element analysis.

4 DATA SUMMARY AND REDUCED TESTING PROTOCOL

The key objective of the project discussed in this report was to perform a thorough investigation of the effects of the microstructural gradient and residual stresses on detail fracture propagation in head-hardened rails, in reference to legacy rails. Since these effects were not previously characterized for modern rails, a comprehensive experimental program, supplemented by advanced numerical analysis was developed and executed. This resulted in multiple fundamental insights into the key effects that can be attributed to the head hardening process, including a distinction between the first and second order effects. This is especially useful as it allows development of a reduced testing protocol for a general characterization of rails.

Based on the experimental data collected for five representative rails (i.e. two modern head hardened, one modern control rail and two legacy rails), trends of behavior have been identified, as briefly summarized in Table 12. These trends can be considered representative of the majority of rails that exist today, which provides a basis for reduced testing protocol outlined in Table 12 and

Table 12 – Summary of the trends in collected data and recommendation for inclusion in the reduced testing protocol

Experimental Tests Performed	Test Standard	Conclusion and Trends	Inclusion in Reduced Testing Protocol
1. Chemical analysis of legacy rail steel	AREMA	Chemical composition for all rails within (or exceeding) AREMA guidelines	Yes
2. Tensile test data	AREMA	Tensile data consistent with previous measurements [35] and AREMA standards	Yes, select rail head location
3. Hardness data	AREMA	Hardness consistent (or exceeding) with AREMA guidelines.	Yes; rail head
4. Light optical microscopy (LOM) – interpretation of the hardness map	-	Uniform perlitic microstructure for all rails; thickness of decarb layer observed	No
5. Hitachi 4300 High Resolution Field Emission SEM – samples removed based on LOM results	-	Cementite / ferrite spacing observations responsible for hardness and strength variations	No
6. Compact tension (CT) specimens – K_{Ic} plane strain toughness	ASTM E399	Fracture toughness fairly uniform across all rails and within each rail head.	Yes, select locations
7. Compact tension specimens – fatigue tests (da/dN tests); additional verification tests with center cracked tension specimen (CCT)	ASTM E647	The fatigue crack growth rate behavior as a function of ΔK is similar for all investigated rails.	Yes, selected locations
8. Neutron diffraction residual stress measurements		Prohibitive beam time needed for full 3D characterization;	Yes, measure residual stress in

		Significant interaction between stress components; Large longitudinal residual stress – critical for detail cracks; Need for a dedicated residual stress effort	CCT specimens before testing *Need for a separate residual stress research program*

5 CONCLUSION

A comprehensive fatigue and fracture characterization effort for modern head hardened rails has been performed, in reference to legacy rails. The main objective of the program was to determine if the head hardening process, designed to improve the wear resistance of rails, resulted in reduction of fatigue life. This was achieved by detailed investigation of the fatigue crack growth rates and fracture properties of the rail material as well as spatial variability of these properties caused by the microstructural gradient inside the rail head. Additionally, residual stress measurements were conducted to determine their magnitude and distribution. The key findings are as follows:

1. The head hardened rails are significantly harder and stronger than legacy rails. Maximum hardness and strength occurs near the running surface of the rail head, which significantly improves wear resistance.
2. All investigated rails, i.e. modern (head hardened), and legacy (non-head hardened) have a uniform pearlitic microstructure except near the surface of the rail head, where a mixed ferrite/pearlite microstructure is observed. This is caused by decarburization that leads to local carbon depletion during high temperature processing. The depth of the decarburized layer is approximately 1mm for all rails (i.e. modern and legacy) with varying density of ferrite, i.e. highest in the HAY84 rail and lowest in the AHH rail.
3. Despite significant hardness and strength variation between different rails, fracture toughness is fairly uniform across all rails (Mean $K_{Ic} = 36.4\ MPa\sqrt{m}$ with a standard deviation of $\sigma = 2.3$). Variation of toughness within each rail head at different depths from the running surface, caused by microstructural gradient, is similar to toughness variation across all rails (e.g. mean toughness in the AHH rail head: $K_{Ic} = 37.8\ MPa\sqrt{m}$ with a standard deviation of $\sigma = 2.8$; SS and HAY84 rail heads: $K_{Ic} = 35.0\ MPa\sqrt{m}$ with a standard deviation of $\sigma = 1.9$; CF&I77 rail head: $K_{Ic} = 41.3\ MPa\sqrt{m}$ with a standard deviation of $\sigma = 3.8$).
4. Fatigue crack growth rate is also similar across all rails, with the biggest difference occurring at low ΔK. However, at low crack growth rates, the relative error associated with determination of Δa is also greater, which could lead to overestimation of the differences between the crack growth rates across all rails. Overall, the fatigue crack growth rate behavior as a function of ΔK is very similar for all investigated rails.
5. Residual stresses due to head hardening and roller straightening are significant, with longitudinal stresses reaching the highest level of approximately ~350MPa. Accurate neutron diffraction measurement of full 3D distribution of residual stresses is challenging due to prohibitively long beam time required to penetrate the rail material. Cutting smaller rail samples, such as plane stress slices and half-rail samples reduces the necessary beam time, making direct measurements possible. Unfortunately, this also leads to complicated, three-dimensional stress redistribution, which makes interpretation of the residual stress state very challenging. Further investigation of the residual stress distribution as well as the wheel-rail contact influence is needed for a complete assessment of the residual stress effect on transverse crack growth in modern rails.
6. Detailed characterization of the microstructure as well as fatigue and fracture properties across all investigated rails, including spatial variability within each rail, provided fundamental

insights into the key effects that can be attributed to the head hardening process. This allows distinguishing the first and second order effects and developing a reduced testing protocol for a general characterization of rails. This testing protocol can be used to characterize other types of rails that have not been investigated as part of this project.

Increasing hardness and strength of the material to improve its wear resistance can be expected to reduce toughness and increase fatigue crack growth rate. In the case of modern, head hardened rails, this is not the case. The results of this study show that the head hardening process of modern rails does not significantly reduce their toughness or fatigue crack growth resistance. This indicates that fatigue-rather than abrasive wear-can become the limiting factor for the overall life of the rail, which places higher emphasis on rail inspection and fatigue life assessment.

While this conclusion has been reached based on the investigation of five specific rails (i.e. two head hardened, one modern control rail and two legacy rails), these rails can be considered representative of the majority of rails that exist today.

6 REFERENCES

1. ASTM E1820–13e1 - Standard Test Method for Measurement of Fracture Toughness
2. ASTM E647–15 - Standard Test Method for Measurement of Fatigue Crack Growth Rates
3. Barsom J.M. and Imhoff, E.J., (1978). Fatigue and Fracture of Carbon-Steel Rails; in: D.H. Stone and G.G. Knupp (eds.). *Rail Steels - Developments, Processing, and Use, ASTM STP 644*, 387-413.
4. Besuner, P.M. (1978). Fracture mechanics analysis of rails with shell-initiated transverse cracks; in: D.H. Stone and G.G. Knupp, eds.: *Rail Steels-Developments, Processing and Use, ASTM STP 644*, 303-329.
5. Bramfitt, B., Fletcher, F., (2013). A Perspective on the Manufacture of Modern-Day High-Strength Steel Rail. AREMA 2013 Annual Conference and Exposition.
6. Budianksy, B., Hutchinson, J.W., (1978). Analysis of Closure in Fatigue Crack Growth. *Journal of Applied Mechanics*, 45, 267-276.
7. Carolan, M.E., Jeong, D.Y., Perlman, A.B., (2014). Engineering Studies on Joint Bar Integrity, Part II: Finite Element Analysis. Proceedings of the 2014 Joint Rail Conference, JRC2014-3708, April 2014. https://ntlsearch.bts.gov/tris/record/ntl/51593.html
8. Deng, X., Hutchinson, J.W., (1996). Approximate methods for analyzing the growth of large cracks in fatigue damaged aircraft sheet material and lap joints. *Finite Elements in Analysis and Design*, 23, 101-114.
9. Deroche et al., (1982). Stress releasing and straightening of rail by stretching, 82-HH-17, *Proc. Second International Heavy Haul Railway Conference*, Colorado Springs.
10. Forman, R.G., Kearney, V.E., and Engle, R.M., (1967). Numerical Analysis of Crack Propagation in Cyclic-Loaded Structures. *Journal of Basic Engineering*, 89,459-464.
11. Fowler G.J. and Tetelman, A.S. (1978). The Effect of Grain Boundary Ferrite on Fatigue Crack Propagation in Pearlitic Rail Steels," in: D.H. Stone and G.G. Knupp (eds.), *Rail Steels - Developments, Processing, and Use, ASTM STP 644*, 363-386.
12. Gnaupel-Herold, T., Brand, P.C., and Prask, H.J. (1999). Neutron Diffraction Investigation of Residual Stresses in Transverse/Oblique Rail Slices Subjected to Different Grinding Strategies. NIST Report NISTIR 6305.
13. Groom, J.J. (1983). Determination of Residual Stresses in Rails. Battelle Columbus Laboratories. Final Report, DOT/FRA/ORD-83/05.
14. Kusko, C.S., DuPont, J.N. and Marder, A.R., (2004a). The Influence of Stress Ratio on Fatigue Crack Propagation Behavior of Stainless Steel Welds, W*elding Journal*, Vol. 83, 59s-64s.
15. Kusko, C.S., DuPont, J.N. and Marder, A.R., (2004b). The Influence of Microstructure on Fatigue Crack Propagation Behavior of Stainless Steel Welds, *Welding Journal*, Vol. 83, pp. 6s-14s.
16. Luzin, V., Prask, H.-J., Gnaupel-Herold, T., Gordon, J., Wexler, D., Rathod, Ch., Pal, S., Daniel, W., and Atrens, A. (2013). Neutron Residual Stress Measurements in Rails; Scientific Reviews; Vol. 24; No. 3.
17. Lyons, M.L., Jeong, D.Y., Gordon, J.E. (2009). Fracture Mechanics Approach to Estimate Rail Wear Limits. Proceedings of the 2009 ASME Rail Transportation Division Fall Technical Conference. RTDF2009-18035
18. Jeong, D. (2016). RSAC Rail Integrity Working Group. US Department of Transportation; Federal Railroad Administration; Volpe National Transportation Systems Center.

19. Jeong, D.Y., Tang, Y.H., Orringer, O., (1997). Damage tolerance analysis of detail fractures in rail. *Theoretical and Applied Fracture Mechanics*; 28, 109-115
20. Jeong, D.Y., Tang, Y.H., Orringer, O., (1998). Estimation of Rail Wear Limits Based on Rail Strength Investigations; US DoT: DOT/FRA/ORD-98/07
21. Jeong, D.Y., Tang, Y.H., Orringer, O., Perlman, A.B., (1998). Propagation Analysis of Transverse Defects Originating at the Lower Gage Corner of Rail. FRA Technical Report. DOT/FRA/ORD-98/06; DOT-VNTSC-FRA-98-14
22. Jeong, D.Y. (2001). Progress in Rail Integrity Research. AREMA 2001 Annual Conference and Exposition.
23. Jeong, D.Y. (2003). Correlations Between Rail Defect Growth Data and Engineering Analyses, Part I: Laboratory Tests. UIC/WEC Joint Research Project on Rail Defect Management Report. USDOT, Volpe National Transportation Systems Center.
24. Jeong, D.Y. (2003). Correlations Between Rail Defect Growth Data and Engineering Analyses, Part II: Field Tests. UIC/WEC Joint Research Project on Rail Defect Management Report. USDOT, Volpe National Transportation Systems Center.
25. Jeong, D.Y., Carolan, M.E., Yu, H., Perlman, A.B., (2012). Fracture Mechanics and Beam Theory Analyses of Semi-Elliptical Cracks Originating in the Base of Rail. Proceedings of the 2012 ASME / ASCE / IEEE Joint Rail Conference: https://ntlsearch.bts.gov/tris/record/ntl/44615.html
26. Journet B. and Pelloux, R.M. (1985). Spectrum loading fatigue crack propagation in rail steel. Massachusetts Institute of Technology, Cambridge, interim report.
27. Journet, B.G., and Pelloux, R.M. (1987a). A Direct Method for Laboratory Spectrum Crack Growth Testing. *Theoretical and Applied Fracture Mechanics*, 7(1), 19-22.
28. Journet, B.G., and Pelloux, R.M. (1987b). A Methodology for Studying Fatigue Crack Propagation under Spectrum Loading: Application to Rail Steels. *Theoretical and Applied Fracture Mechanics*, 8(2), 117-123.
29. Kelleher, J., Prime, M.B., Buttle, D., Mummery, P.M., Webster, P.J., Shackleton, J., and Withers, P.J. (2003). The Measurement of Residual Stress in Railway Rails by Diffraction and Other Methods. *Journal of Neutron Research*, 11(4), 187-193.
30. Landis, C., Pardoen, T., Hutchinson, J. W., (2000). Crack velocity dependent toughness in rate dependent materials. *Mechanics of Materials*, 32, 663-678.
31. Magiera, J., Orkisz, J. Karmowski, W. (1996). Reconstruction of residual stresses in railroad rails from measurements made on vertical and oblique slices. *Wear*, 191, 78-89.
32. Orkisz, J., Orringer, O., Hołowiński, M., Pazdanowski, M., Cecot, W., (1990). Discrete Analysis of Actual Residual Stresses Resulting from Cyclic Loadings; Computers and Structures, 35, 397-412.
33. Orringer, O., Morris, J.M. and Steele, R.K. (1984) Applied research on rail fatigue and fracture in the United States; *Theoretical and Applied Fracture Mechanics;* 1, 23-49.
34. Orringer, O., Morris, J.M., Jeong, D.Y. (1986). Detail Fracture Growth in Rails: Test Results; *Theoretical and Applied Fracture Mechanics*, 5, 63-95.
35. Orringer, O., Tang, Y.H., Gordon, J.E., Jeong, D.Y., Morris, J.M., Perlman, A.B. (1988). Crack Propagation Life of Detail Fractures in Rails. Final Report, DOT/FRA/ORD-88/13
36. Orringer, O., (1990). Control of Rail Integrity by Self-Adaptive Scheduling of Rail Tests. DOT/FRA/ORD-90/05
37. Orringer, O., Orkisz, J., Swiderski, Z., (1992), Residual Stress in Rails: Effects on Rail Integrity and Railroad Economics; Kluwer Academic Publishers.

38. Pazdanowski, M., (2014) Residual stresses as a factor of railroad rail fatigue. Technical transactions Civil Engineering; 4-b/2014
39. Prime, M. B., Gnaupel-Herold, T., Baumann, J.A., Lederich, R.J., Bowden, D.M., Sebring, R.J., (2006). Residual stress measurements in a thick, dissimilar aluminum alloy friction stir weld. *Acta Materialia,* 54, 4013–4021.
40. Prime, M. B., DeWald, A.T., (2013). The Contour Method. Chapter 5 in *Practical Residual Stress Measurement Methods,* G. S. Schajer, (ed.), Wiley-Blackwell, pp. 109-138.
41. Reed, H.M., (2017).
42. Rungta, R., (1985), Battelle Columbus Laboratories
43. Schleinzer, G., Fischer, F.D. (2001). Residual stress formation during the roller straightening of railway rails. *International Journal of Mechanical Sciences.* 43, 2281–2295.
44. Sih, G.C. and Tzou, D-Y., (1984). Three-dimensional transverse fatigue crack growth in rail head. *Theoretical and Applied Fracture Mechanics*, 1, 103-115.
45. Sprucegroveexaminer.com – Gainford TX Derailment
46. Timoshenko, S. and Langer, B.F. (1932). Stresses in railroad track; *ASME Transactions, 54*, 277-293.
47. Voyiadjis, G.Z., Woelke, P.B. (2008). Elasto-plastic and damage analysis of plates and shells. Springer Science & Business Media.
48. Walker, E.K. (1970). The Effect of Stress Ratio During Crack Propagation and Fatigue for 2024-T3 and 7075-T6 Aluminum. In *Effects of Environment and Complex Load History on Fatigue Life*. ASTM STP 462:1-14. American Society for Testing and Materials.
49. Wang, C.H., Hutchinson, J.W., (2001). Interactions of fatigue cracks with elastic obstacles. *Int. J. Fracture*, 109, 263-283.
50. Wang, B., Zheng, T., Wu, S., Chiang, F. (1999). Experimental 3-D Residual Stress Measurements in Rails with Thermal Annealing. Report DOT/FRA/ORD-99/04. USDOT, Volpe Center, Cambridge, MA.
51. Wineman, S.J., (1991). Residual Stresses and Web Fracture in Roller-Straightened Rail. Ph.D., thesis; MIT, Dept. of Mechanical Engineering; http://hdl.handle.net/1721.1/26829
52. Zhan, X., Wang, S., (2005). Research on the Improvement of Rail Head Hardening Technology on Railway. Proceedings of the Eastern Asia Society for Transportation Studies, 5, 263 – 271.
53. Sellew, W. H., "Steel Rails – Their History, Properties, Strength and Manufacture", D. Van Nostrand Co., 1913.
54. "Manual of Recommended Practice for American Railway Engineering and Maintenance of Way Association", Edition of 1907, Committee No. IV, Rail pp. 55-58.
55. D.F. Cannon, K.O. Edel, S.L. Grassie and K.Sawley, "Rail defects: an overview", (2003).
56. Farris, T.N., Keer, L.M, and Steele, R.K. (1991) "Life prediction for unstable shell growth in rails"
57. *"Proposed Standard Specifications for Steel Rails",* Proceedings American Society for Testing and Materials, Vol. 7, 1907, p. 57.
58. Bramfitt, B. L.,Wirick, D. P. and Cross, R. L "Advanced In-Line Head Hardening of Rail", Iron and Steel Society, Proc. International Symposium on Rail Steel 1994, p. 23-29.
59. d Bramfitt, B. L., "Accelerated Cooling of Rail", Iron and Steel Society, Proc.Mechanical Working and Steel Processing Conf., Vol. XXVII, 1990, p. 485-496.

APPENDIX A. HARDNESS VALUES AS A FUNCTION OF POSITION

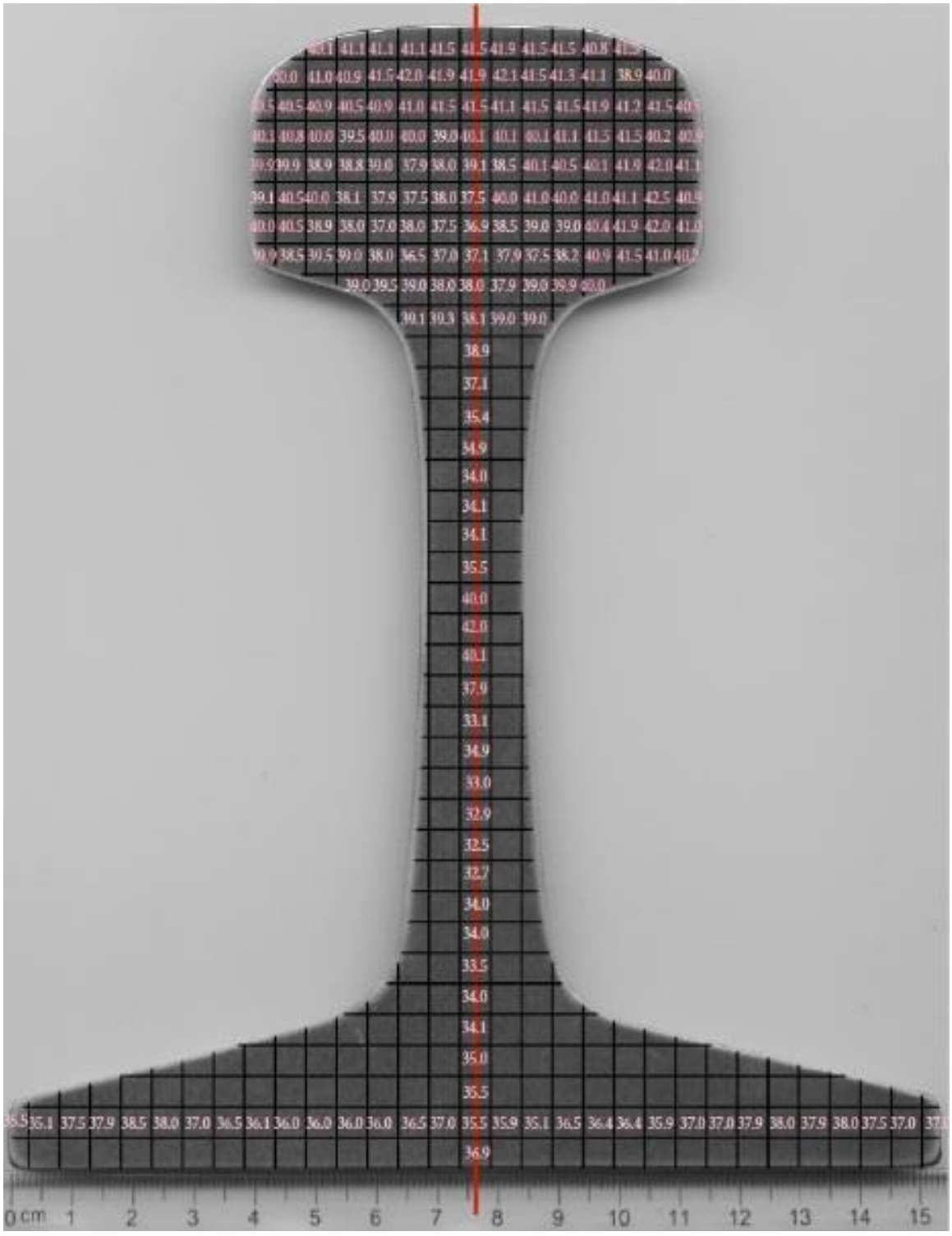

Figure 114 – AHH Rail showing measured HRC hardness values

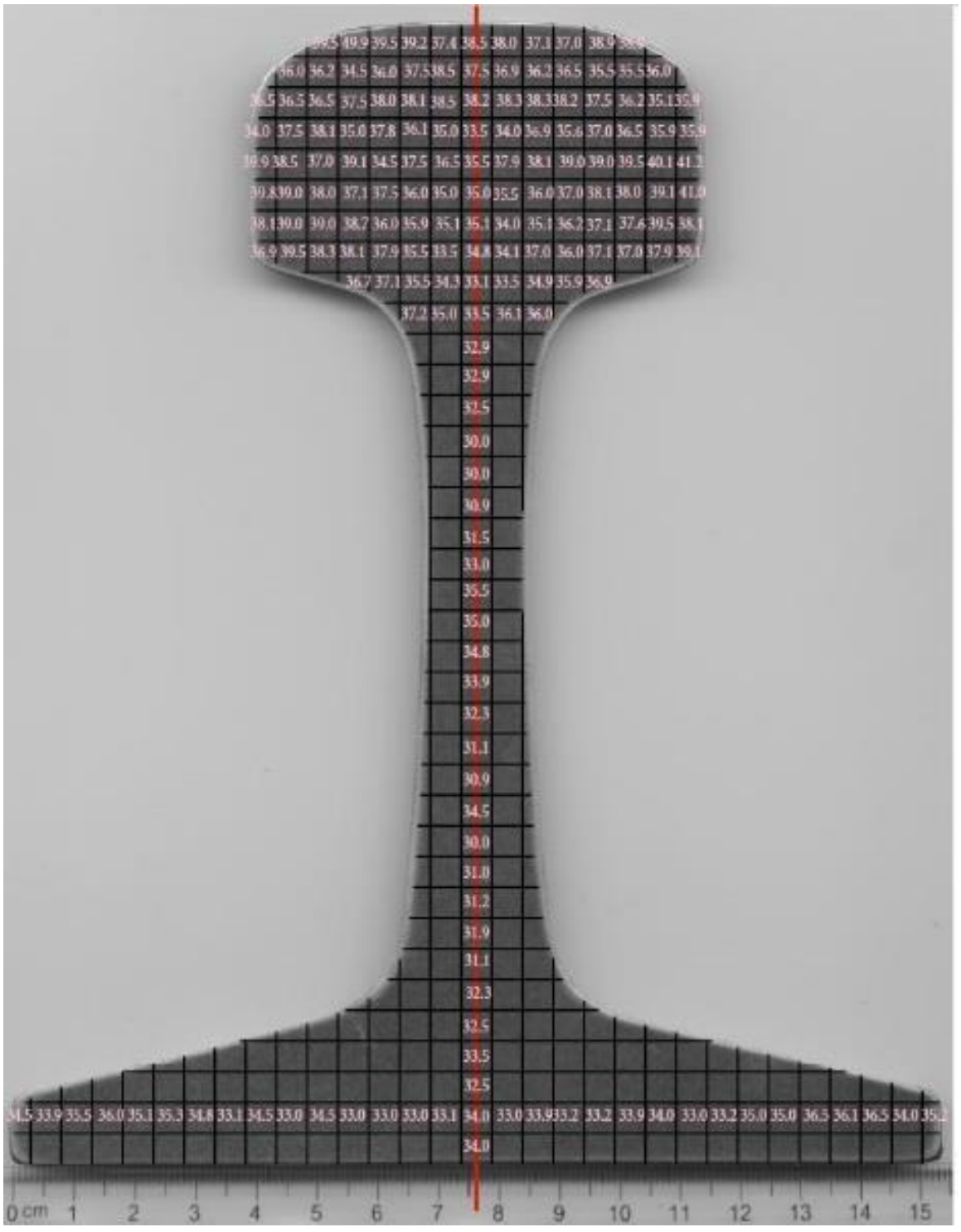

Figure 115 – HH Rail showing measured HRC hardness values

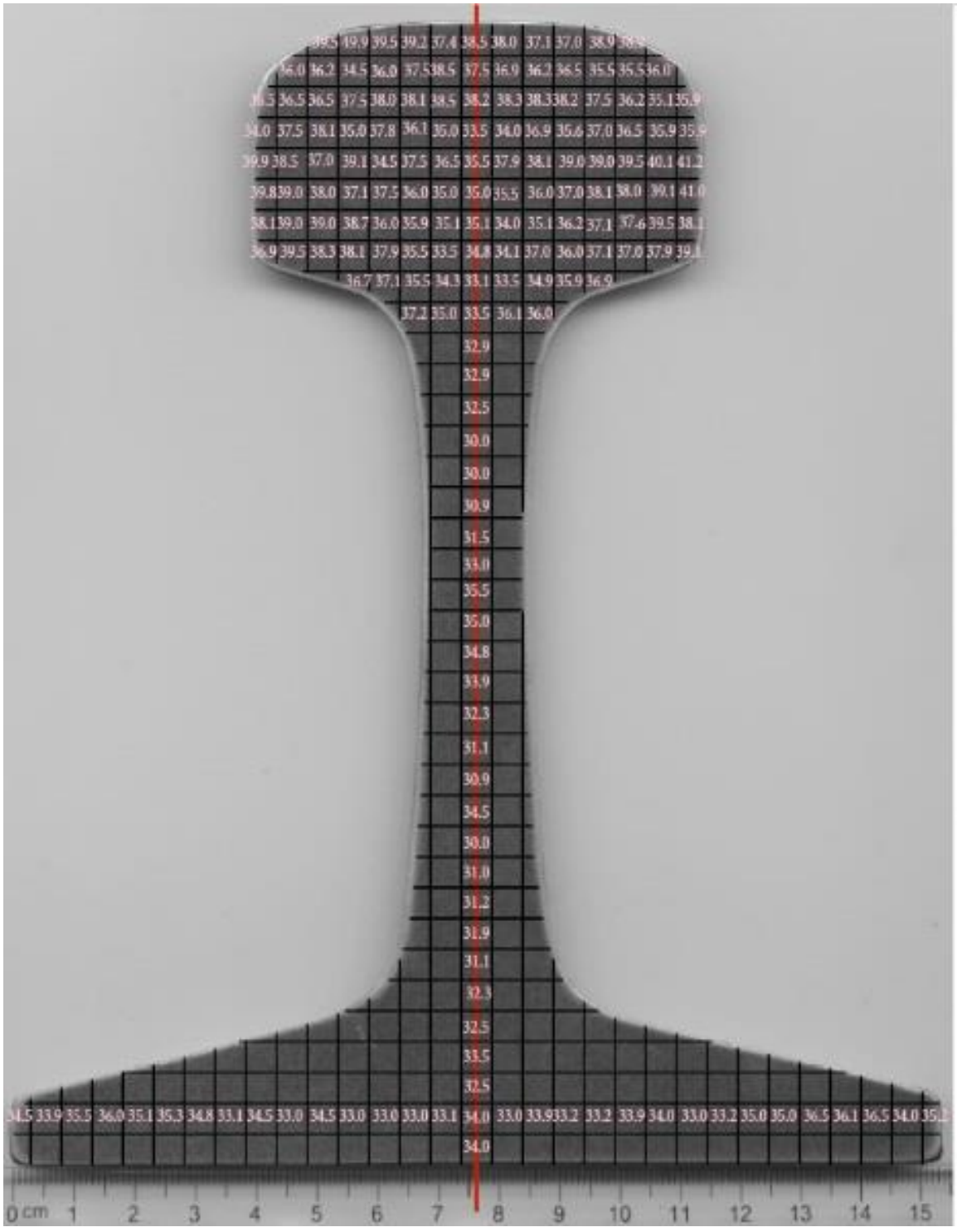

Figure 116 – SS Rail showing measured HRC hardness values

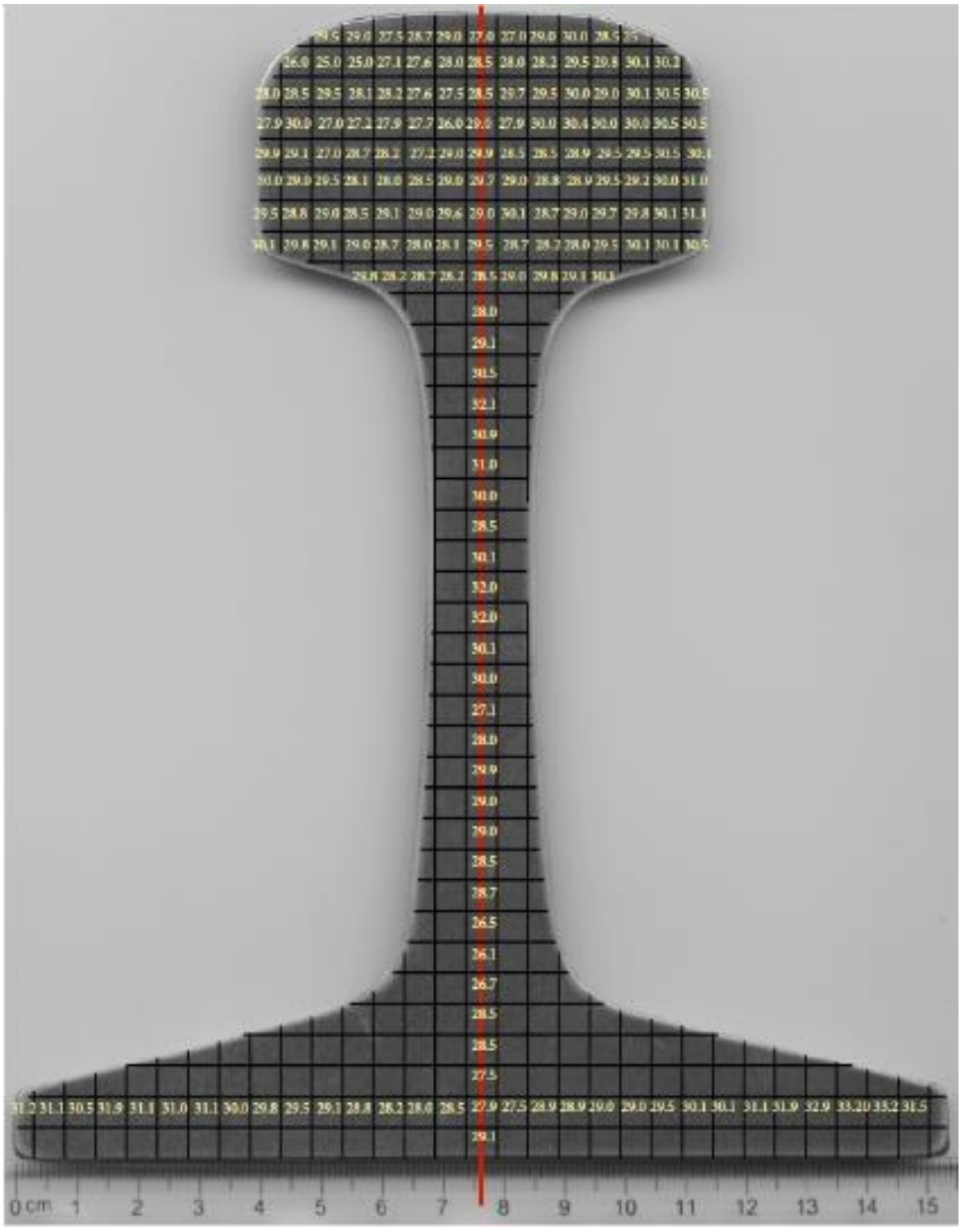

Figure 117 – HAY84 Rail showing measured HRC hardness values

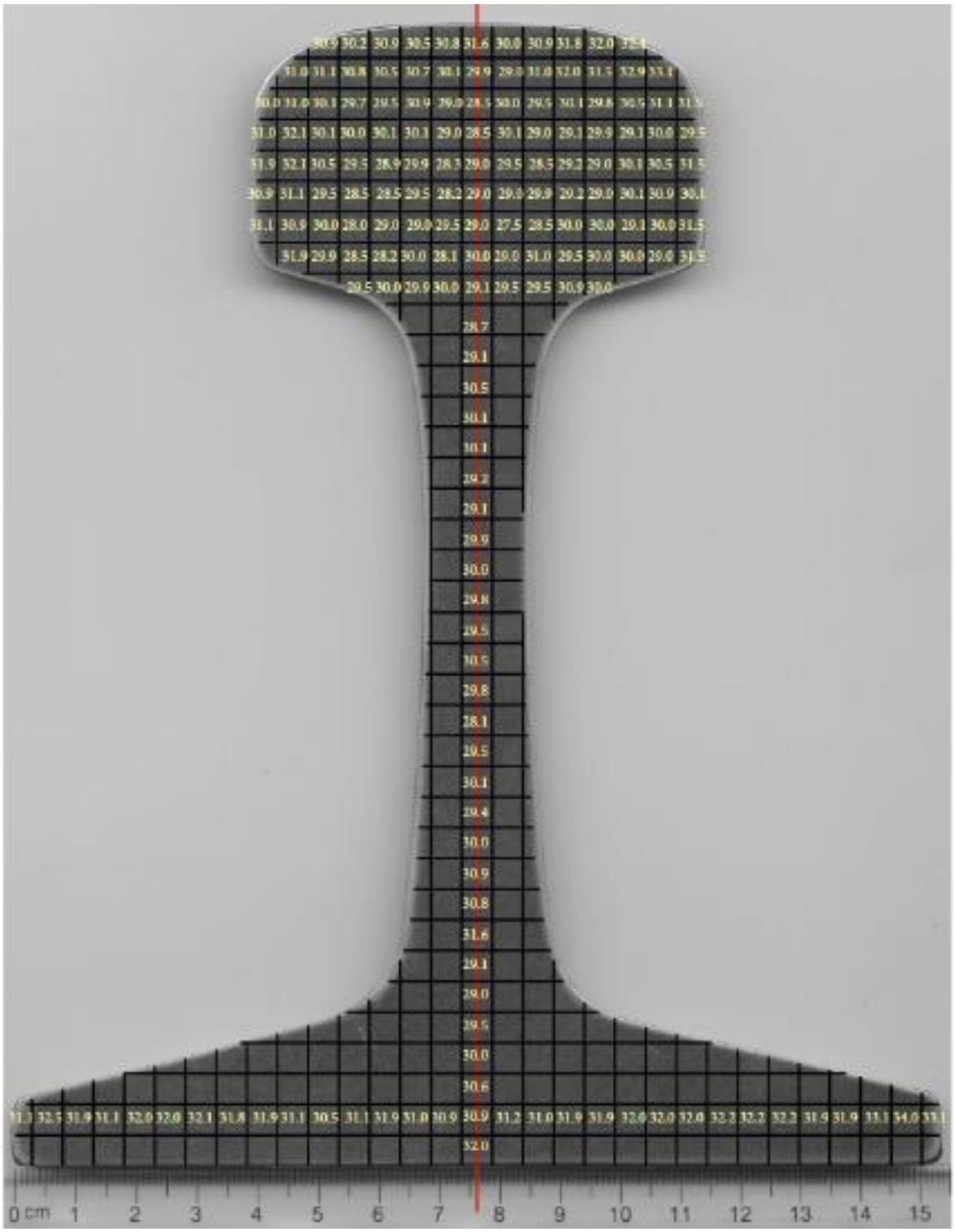

Figure 118 – CF&I77 Rail showing measured HRC hardness values

APPENDIX B. TENSILE STRESS STRAIN CURVE

As depicted in Figure 119, the standard "offset method" was used to determine the tensile yield strength in accordance with ASTM E8 standards. Referring to Fig. 119, *om* is the specified value of the offset, *mn* is drawn parallel to *OA*, determining *r*, i.e., the intersection of *mn* with the stress-strain curve. In reporting values of yield strength obtained by this method the specified value of the offset was 0.2%. Typical stress/strain curves for each of the rails, taken from layer #2 in the rail heads (see Fig. 45), are given in Figs. 120 - 124.

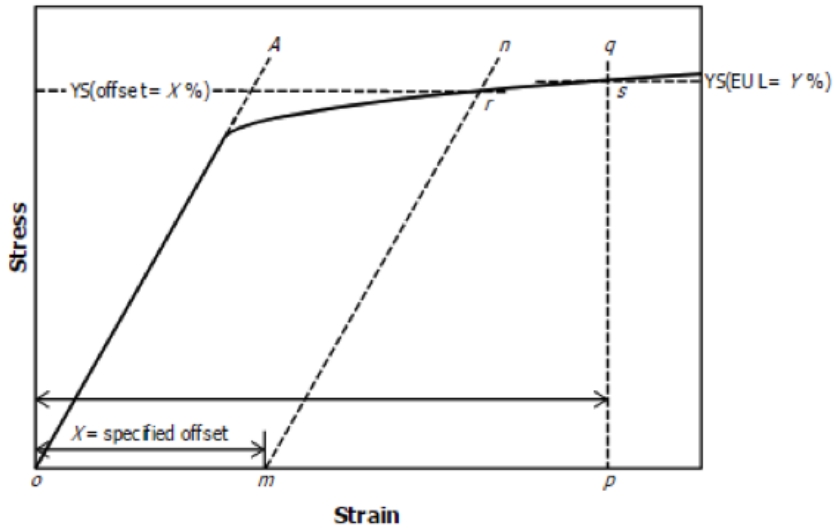

Figure 119 – Determination of yield stress based on 0.2% offset.

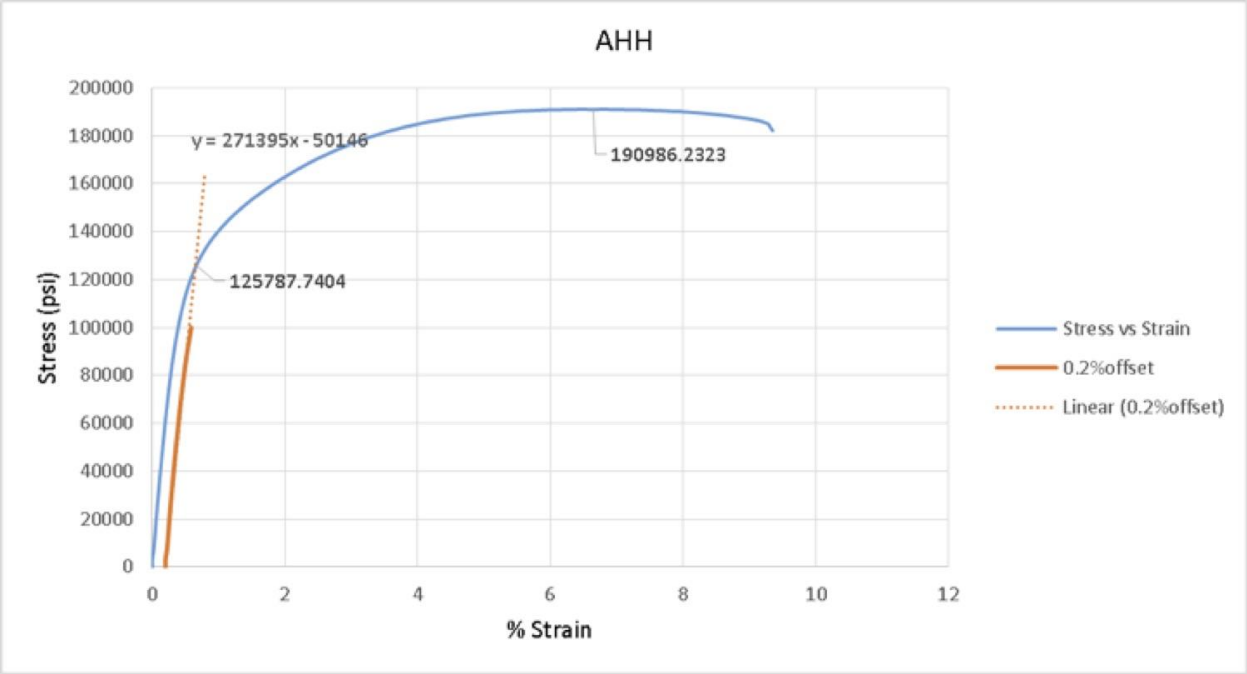

Figure 120 – Stress vs Strain for AHH rail, layer #2.

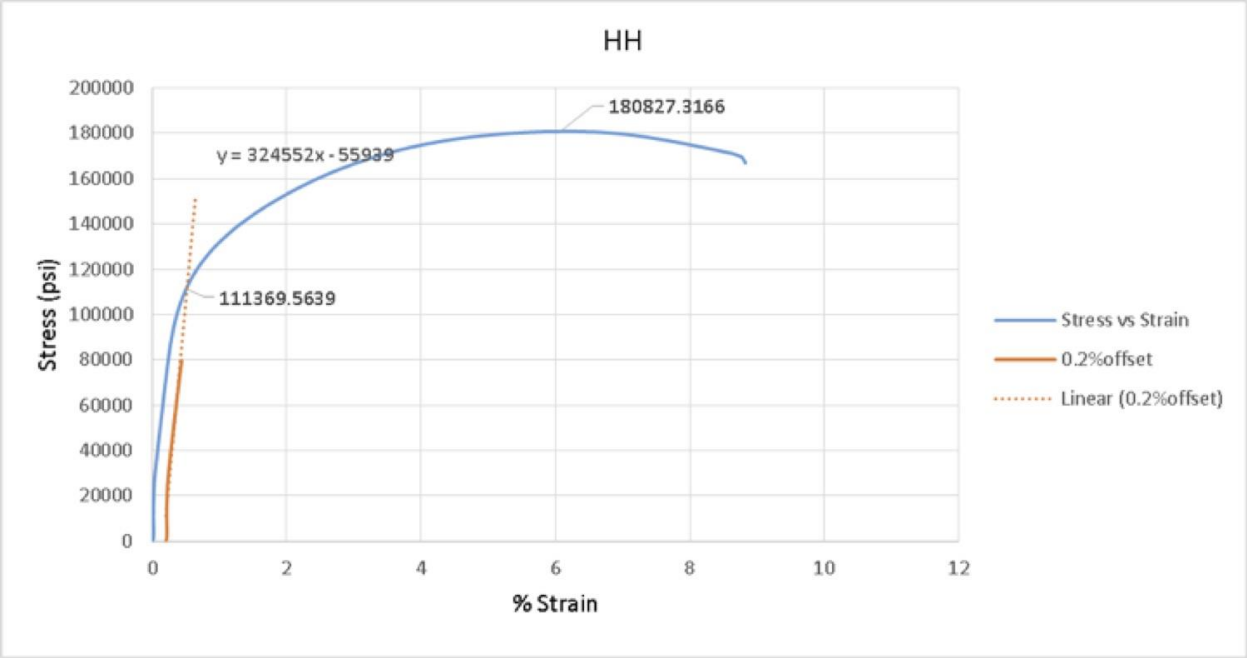

Figure 121 – Stress vs Strain for HH rail, layer #2.

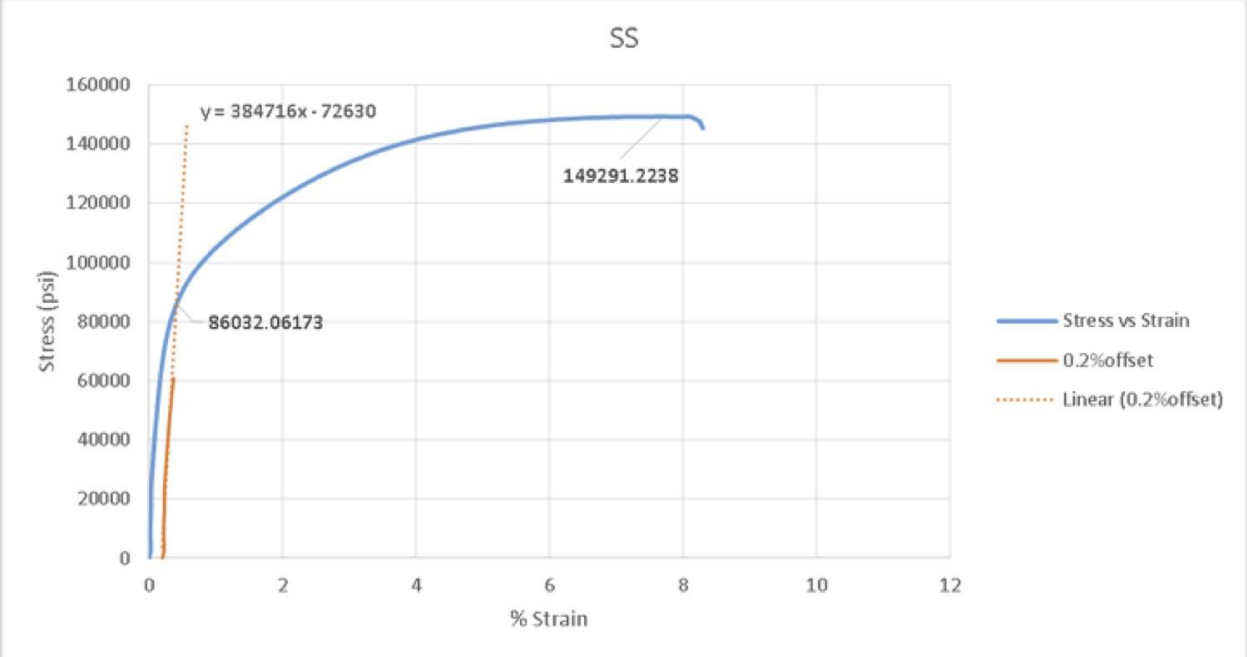

Figure 122 – Stress vs Strain for SS rail, layer #2.

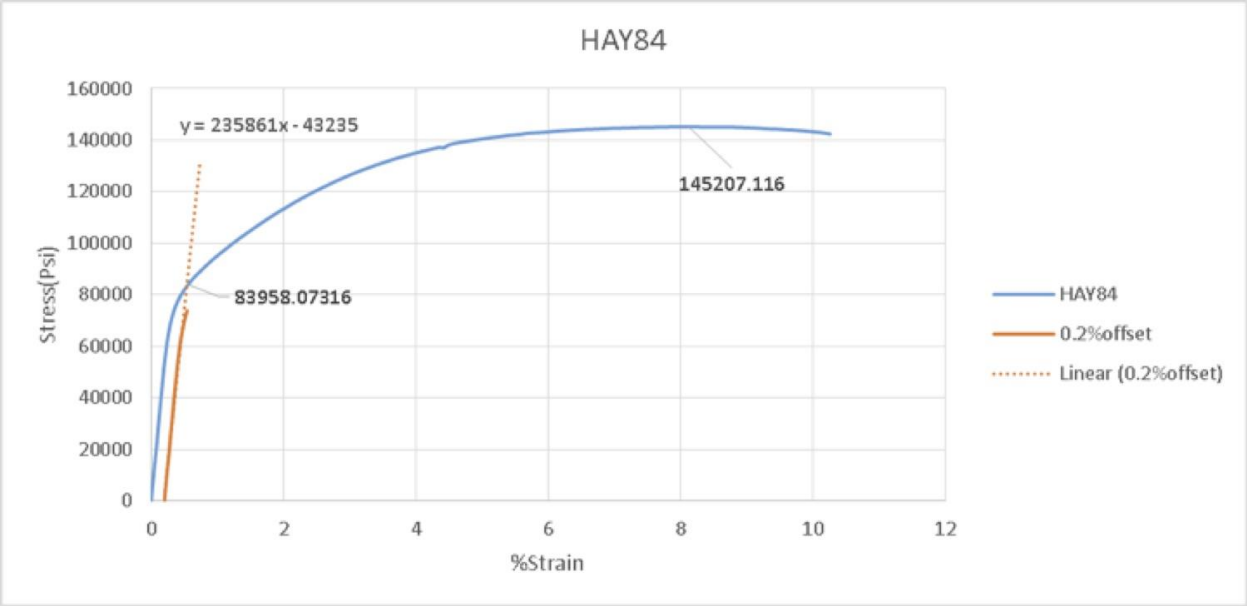

Figure 123 – Stress vs Strain for HAY84 rail, layer #2.

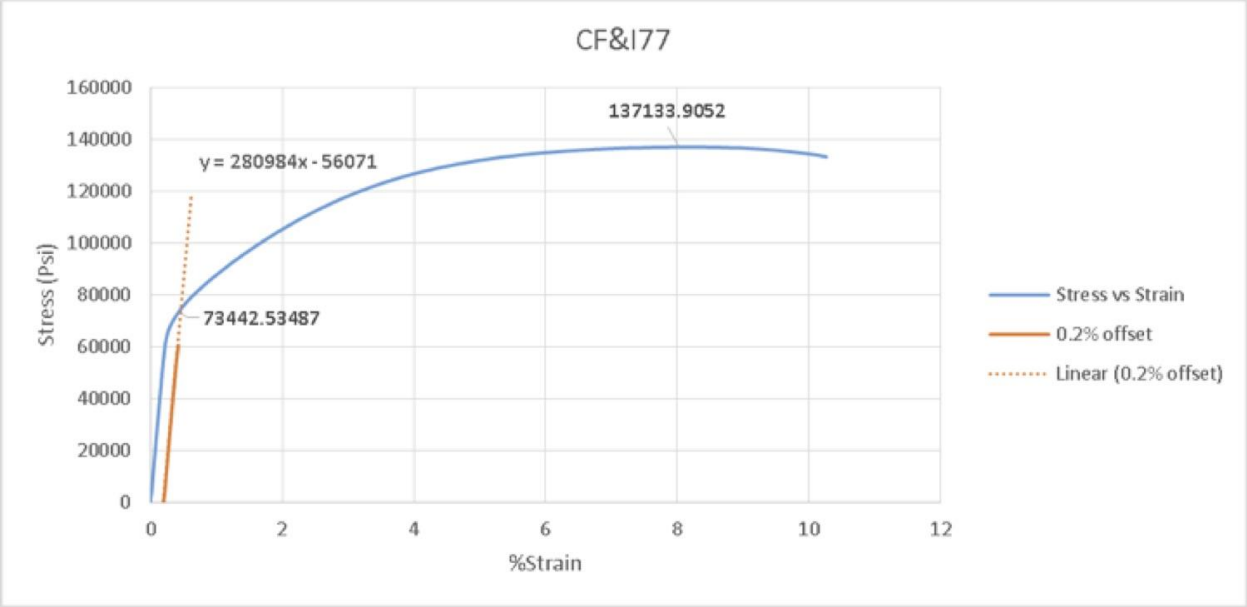

Figure 124 – Stress vs Strain for CF&I77 rail, layer #2.

APPENDIX C. LOAD VS COD CURVES FOR FRACTURE TOUGHNESS

EQUATION SECTION 3

A valid K_{Ic} test requires the determination of a preliminary conditional result, K_Q, which is determined from a graphical construction based on the load-displacement test record, where the displacement is the crack opening displacement (COD) measured at the mouth of the crack. Measurement of the crack opening displacement in the fracture testing is done using a clip gauge extensometer as shown in the photograph in Figure 55. The clip gauge is attached to the CT specimen using machined knife-edges at the mouth of the crack as shown in the photograph in Figure 53. If, after testing, the calculated value of K_Q satisfies the necessary small scale yielding requirements specified in the ASTM E399 Standards, K_Q can be reported as a valid K_{Ic} value.

When a precracked CT test specimen is loaded to failure, one of three types of valid load vs displacement (COD) curves are possible (see Figure 125). Depending on the actual load-displacement curve that occurs during a test, a value for the critical load, P_Q, is selected, which is then used to calculate K_Q based on the tabulated stress intensity factor solution.

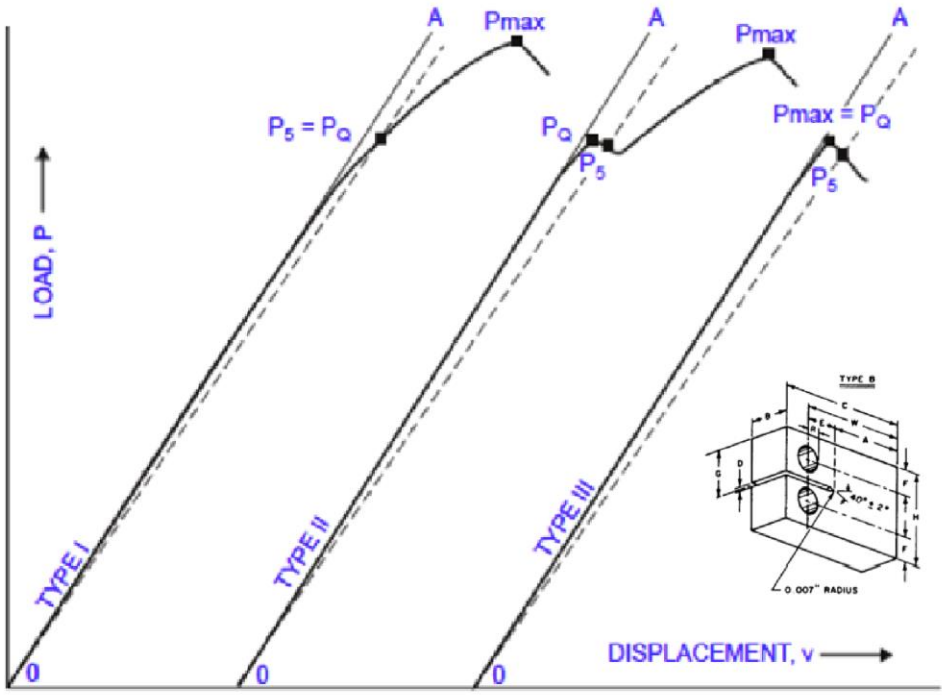

Figure 125 – Typical load displacement curves encountered during fracture toughness testing

To obtain P_Q, a line OA is drawn tangent to the initial linear portion of the load-displacement curve. A second line, designated as O_{P5}, and called the 5% Secant line, is constructed with a slope

equal to 95% of the initial load line. The point at which the load-displacement curve and the 5% Secant line intersect, determines the point P_5 as shown in Fig. 125.

P_Q is determined by the specific load-displacement behavior for a particular test specimen. If the curve is smooth and deviates only slightly from linearity before reaching the ultimate failure load at $P_{\max}$, then it is referred to as a Type I curve as shown in Fig. 125 and $P_Q = P_5$. Alternatively, a Type II curve, will exhibit a small amount of unstable crack growth, often referred to as pop-in, which occurs before the curve deviates from linearity by 5%. For a Type II curve, P_Q is defined at the pop-in load (Fig. 125). A specimen that fails before achieving 5% nonlinearity, is described as a Type III curve. In this case, $P_Q = P_{\max}$, as shown in Fig. 125. With P_Q determined from the load-displacement curve, K_Q is calculated using the following formula valid for CT specimens

$$K_Q = f\left(\frac{a}{W}\right)\sigma_Q\sqrt{\pi a}\ , \tag{C1}$$

where

$$f(a/W) = 16.7 - 104.7(a/W) + 369.9(a/W)^2 - 573.80(a/W)^3 + 360.5(a/W)^4 \tag{C2}$$

and

$$\sigma_Q = \frac{P_Q}{BW}\ . \tag{C3}$$

The average crack length a at fracture is determined by directly measuring the crack length on the fractured crack surface at five equally spaced points (0, 0.25, 0.5, 0.75, 1) along the crack front (see Figure 56). The calculations for determining K_{Ic} for an AHH rail CT specimen, based on the load-displacement measurements depicted in Figure 126, will be given as an example. In this particular case the relevant geometric parameters are: 1) crack length $a = 0.0125\,\text{m}$, 2) width $W = 26\,\text{mm}$, and 3) thickness $B = 12.5\,\text{mm}$. Thus, $a/W = 0.48$ and from (C2) $f\left(a/W\right) = 7.34$. From the load-displacement curve (Fig. 126), the value of $P_Q = 7684\,\text{N}$, and from (C3), $\sigma_Q = 7684/\left(26 \times 12.5\right) = 23.64\,\text{MPa}$. Using eqns. (C1) and (C2) K_Q is determined to be: $K_Q = 34.4\,\text{MPa}\sqrt{\text{m}}$. The value of σ_Y was measured as $\sigma_Y = 792\,\text{MPa}$. Thus, it can quickly be established that the value of K_Q satisfies the plane strain requirements (2.6.1)-(2.6.3) for reporting a valid plane strain fracture toughness (K_{Ic}) value. The additional ASTM requirements that 0.45<(a/W)<0.55 and $P_{\max} \le 1.1P_Q$ are also satisfied in this test, thus for this specific test, $K_{Ic} = 34.4\,\text{MPa}\sqrt{\text{m}}$. Not all fracture toughness tests conducted in this study resulted in valid K_{Ic} values. In most of the invalid cases, there were minor deviations from the strict ASTM specifications, e.g., the initial fatigue crack front was insufficiently straight, or $P_{\max}$ was slightly greater than P_Q, etc. Though the values of K_Q from these tests were still within the range of valid K_{Ic} values, they are not reported as K_{Ic} values. Representative load-displacement plots that were

used for determining K_{Ic} values for all five rails used in this study are shown in Figs. 126 - 130. In each of these figures the P_Q, P_{max}, and K_Q values are given on the plots.

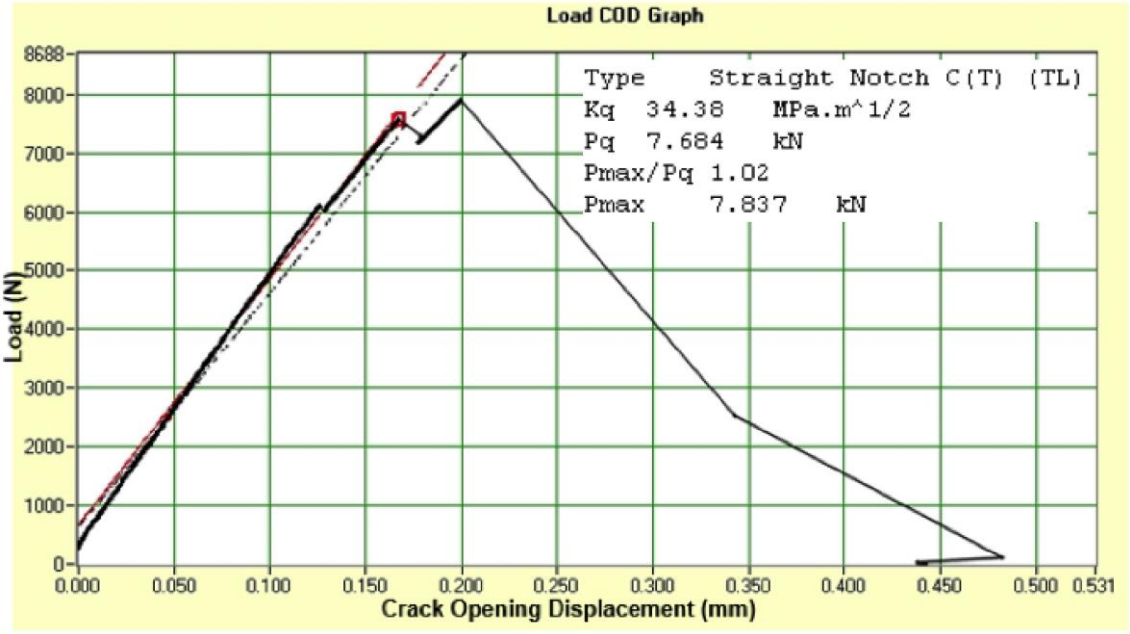

Figure 126 – Load vs COD for AHH Rail Fracture Toughness Test.

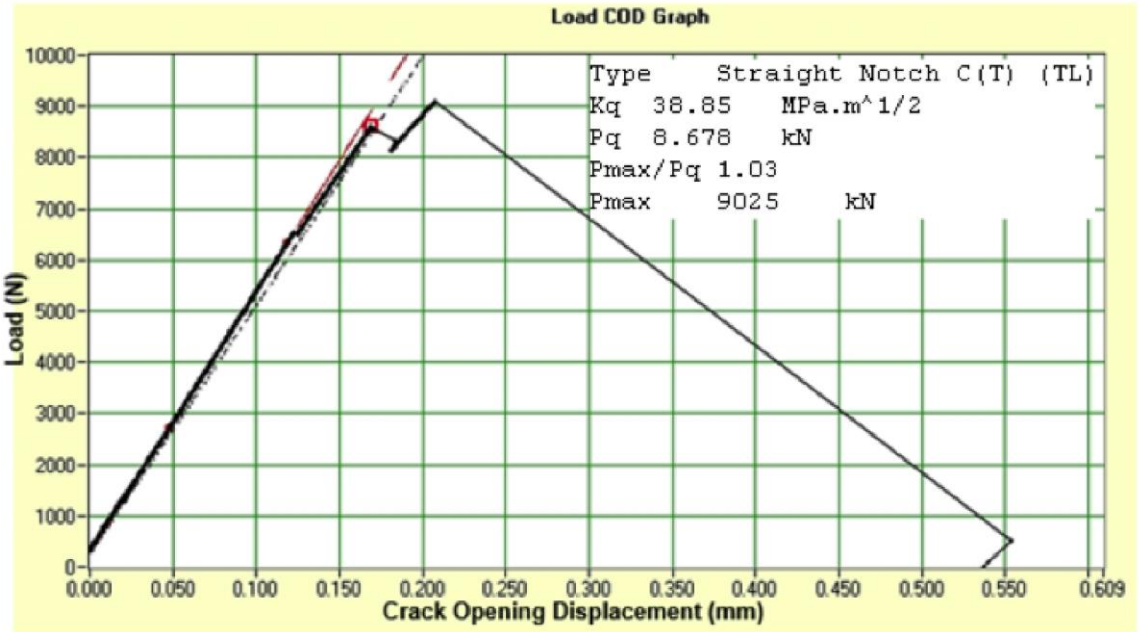

Figure 127 – Load vs COD for HH Rail Fracture Toughness Test.

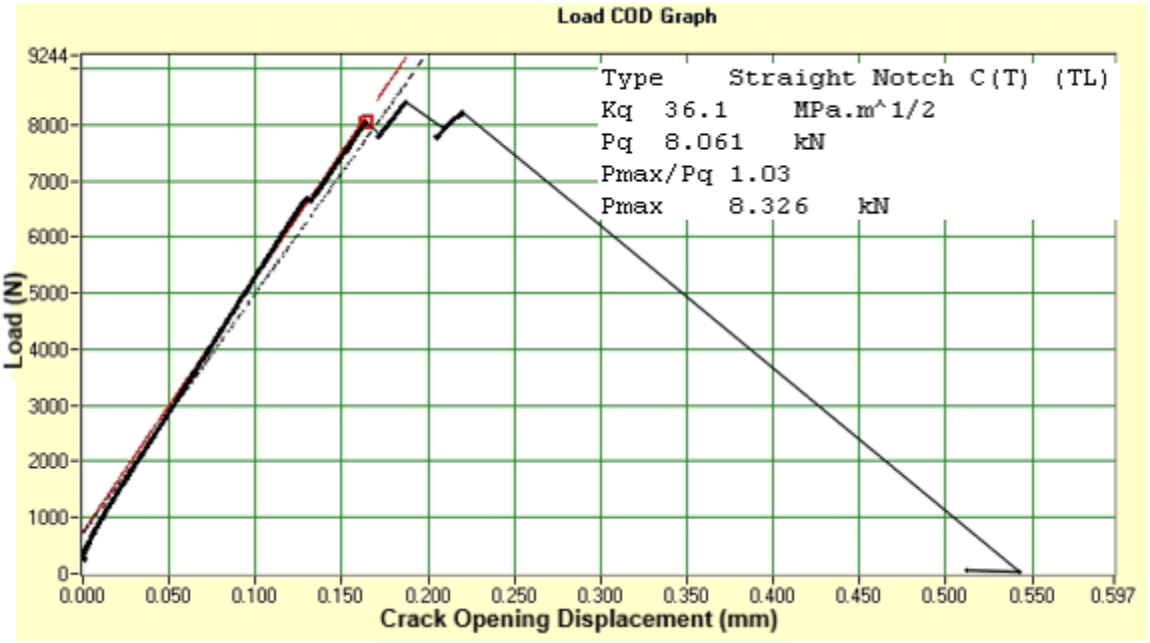

Figure 128 – Load vs COD for SS Rail Fracture Toughness Test.

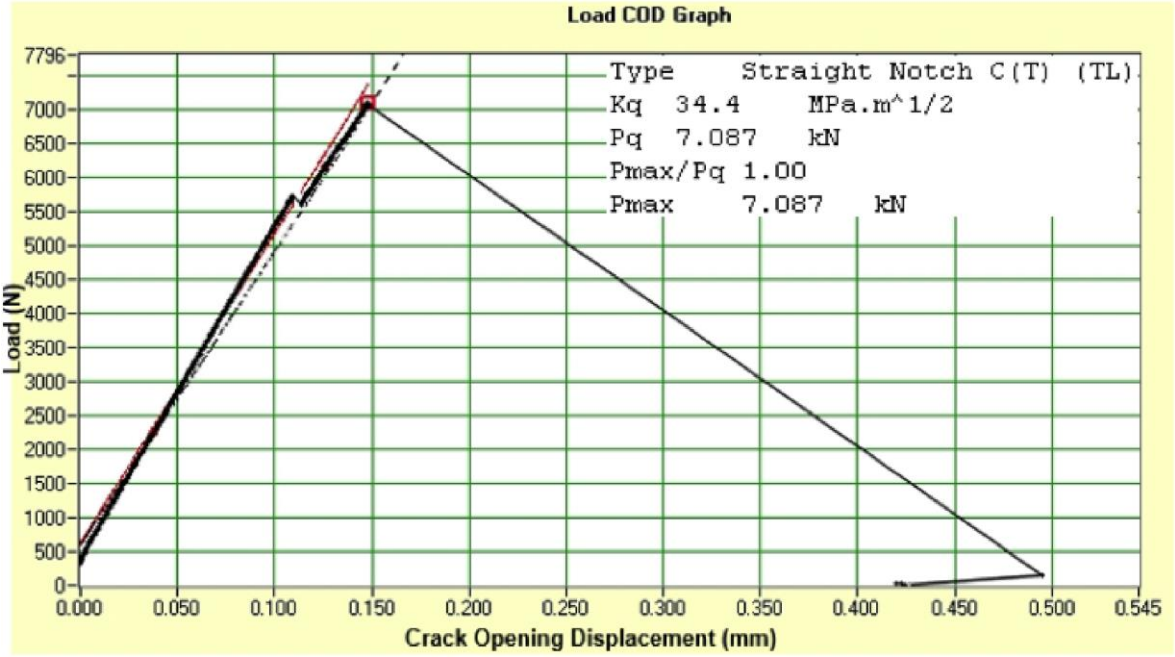

Figure 129 – Load vs COD for HAY84 Rail Fracture Toughness Test.

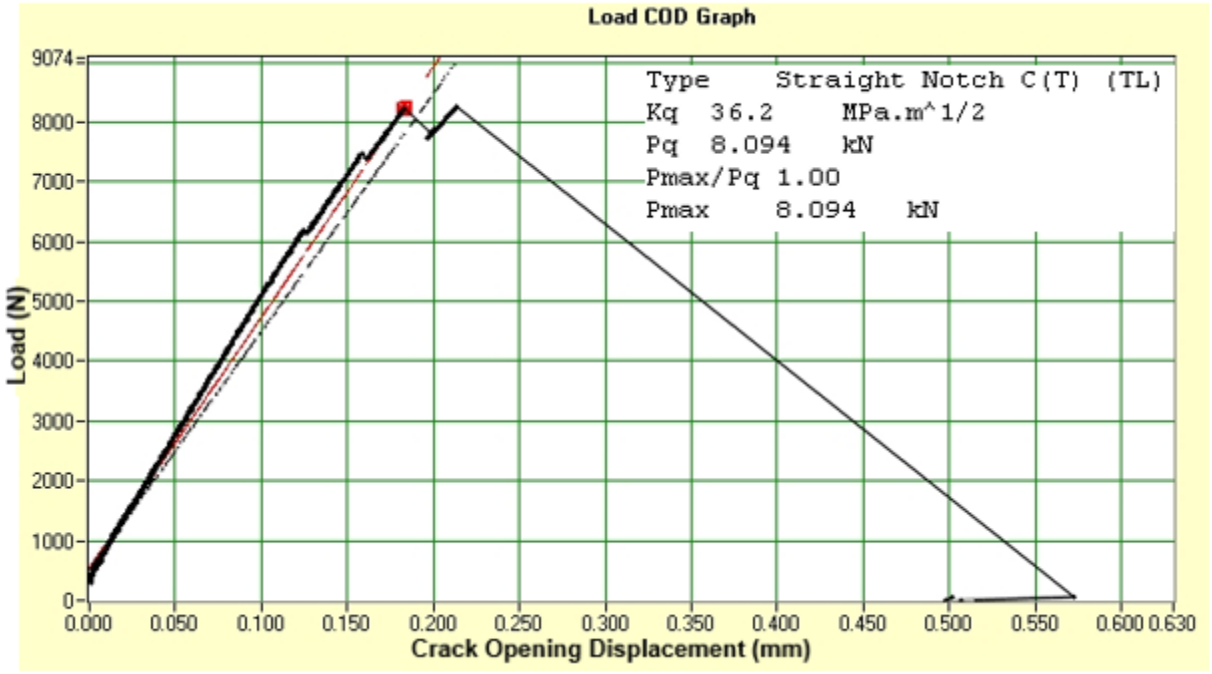

Figure 130 – Load vs COD for CF&I77 Rail Fracture Toughness Test.

COMPLIANCE CRACK LENGTH CALCULATION

During fatigue crack growth rate testing, the crack length a is inferred from changes in the measured compliance. The relationship between compliance and crack length has been analytically derived for the compact tension C(T) specimen. The normalized crack length, a/W, is given by the following polynomial expression

$$\frac{a}{W} = 1.0010 - 4.6695(U) + 18.460(U)^2 - 236.82(U)^3 + 1214.9(U)^4 - 2143.6(U)^5 , \qquad \text{(C4)}$$

where

$$U = \frac{1}{1+\sqrt{\frac{E d_1 B}{P}}} . \qquad \text{(C5)}$$

In (C5) E is the elastic modulus, d_1 is the measured crack opening displacement (COD), P the measured load, and B the specimen thickness. Figure 131 shows a screen capture from the software used to compute the CT crack length, a, during fatigue testing on the Instron mechanical test machine shown in Fig. 55.

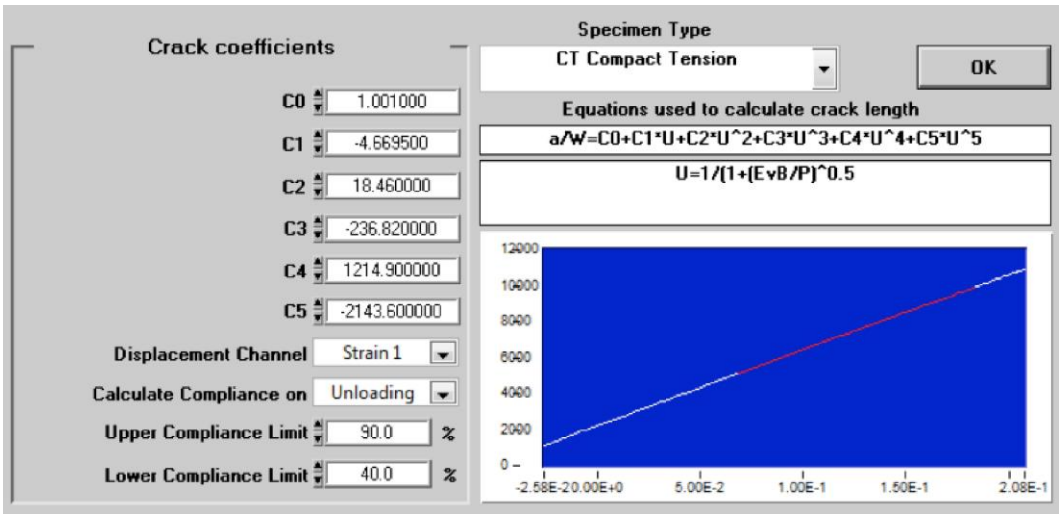

Figure 131 – Crack length calculations based on compliance measurements during testing.

VITA

Sena Kizildemir was born on March 28, 1994 in Istanbul, Turkey. Sena earned a Bachelor of Science degree in Civil Engineering at Istanbul Isik University in January, 2016.

After graduating with valedictorian honors, she was accepted to pursue her Master of Science degree in Civil and Environmental Engineering in Lehigh University where she also was awarded research assistantship in Mechanical Engineering and Material Science.

Following the completion of her Master's degree in May,2018 , she will be continuing to pursue her Ph.D. program in Lehigh University.